Nanostructural Effects on Uncompensated Spin Ensemble in Oxide Thin Films Fabricated by RF Magnetron Sputtering

アグストリスノ マルリス ヌラツ

Nanostructural Effects on Uncompensated Spin Ensemble in Oxide Thin Films Fabricated by RF Magnetron Sputtering

By

Agusutrisno Marlis Nurut

Department of Electronics

Graduate School of Information Science and Electrical Engineering

Kyushu University

2024

Table of Contents

List of Figures

Abstract

Uncompensated spin ensembles have been successfully obtained by manipulating nanostructures in oxide thin films, paving an avenue for the exploration and development of spintronic devices, beyond the conventional metal-based ferromagnets. The nanostructures in magnetic nonmetallic ferromagnet have captivated researchers, because of their inherent advantages and distinctive properties. Diluted magnetic semiconductors (DMSs), which exploit both the charge and spin of electrons in semiconductors, offer valuable functionalities in spintronic devices, as their magnetic properties such as the Curie temperature and coercivity can be electrically controlled. The main challenge associated with this material is to increase the critical temperature without producing secondary phases. Ferrimagnetic insulators, which employ spin-orbit torque to manipulate magnetic moments, have the potential to become energy-efficient magnetic memory and logic devices. Controlling magnetic anisotropy to achieve perpendicular magnetic anisotropy (PMA) is the main challenge for this material.

In this study, the effects of nanoscale inhomogeneity in DMS materials and nanoscale lattice strain in ferrimagnetic insulators are investigated. Co-doped ZnO (ZnO:Co) is selected as the DMS material owing to the large moment of Co and its high solubility in Zn. Thulium iron garnet (TmIG) is chosen as the ferrimagnetic insulator because of its large negative magnetostriction constant, which potentially induces PMA. These materials were fabricated by radio-frequency magnetron sputtering.

The formation and control of inhomogeneities in the ZnO:Co film, which exert a significant influence on their structures and magnetic properties, are successfully achieved through nitrogen-mediated crystallization. The superparamagnetic–ferromagnetic properties of ZnO:CoN films with the highest inhomogeneous structures are obtained at annealed of 400 °C only, which is the optimum value before the desorption of N. To focus on the effects of nanoscale inhomogeneity on magnetic properties, other structural and compositional differences among the samples are eliminated by preparing a set of samples by varying only the postannealing time. An enhancement of the coercivity and blocking temperature is observed upon increasing the postannealing time, suggesting that this treatment changes the distribution of Co atoms in the film. A novel approach for the analysis of nanoscale

inhomogeneity, derived using energy-dispersive X-ray spectroscopy (EDX) is demonstrated, offering a direct measure of the inhomogeneity based on statistical analysis. The Gaussian distribution function provides an accurate representation of the ratio distribution of Co and Zn, thus facilitating a comprehensive investigation into the origin of the magnetic moment.

The fabrication of TmIG films with PMA and larger areas is successfully achieved by on-axis sputtering, in contrast to the previous studies that used unusual off-axis geometries. The PMA, which is crucial for efficient manipulation of magnetization by spin-orbit torque injection from an adjacent conductive layer, is attained by controlling the thermal annealing, thickness, and Tm/Fe ratio, according to the relative positions of the substrate and target.

Two significant findings have emerged from this study. First, a pioneering method for creating and analyzing nanoscale inhomogeneities in DMS materials is introduced, providing a promising avenue for advancing the understanding of DMS. Second, on-axis sputtering has been successfully employed to fabricate TmIG films with PMA, which is a potential approach for the large-scale fabrication of ferrimagnetic insulators with PMA, which can significantly improve the production efficiency in industrial applications.

Chapter I

Introduction

1. Introduction

Harnessing the spin degree-of-freedom as the second fundamental property of electrons has increased the data storage density, accelerated the data processing, and reduced the power consumption, paving the way for revolutionary advancements in information technology[1]. One of the most prominent achievements in this field is the configuration of the spin ensemble to encode digital information using binary states (1 and 0), based on the giant magnetoresistance phenomena[2–4]. This breakthrough has transformed conventional memory-device operations, profoundly impacting the mass-data-storage industry[5]. However, despite their advanced development, metal-based ferromagnetic materials face challenges related to Joule heating and energy dissipation[6]. Ferromagnetic semiconductors and ferrimagnetic insulators have garnered considerable attention to address these issues and offer potential solutions to improve the performance and power efficiency. By maintaining a particular spin state, ferromagnetic semiconductors eliminate the need for an external power source, a characteristic of nonvolatile devices. This property allows these materials to retain information without continuous power, enhancing the energy efficiency and reliability in data-storage applications[6]. In a ferrimagnetic insulator, information is carried by spin waves rather than electrons. Spin currents are highly efficient because they eliminate electrical resistance and Joule heating within the magnetic layer[7–9].

One method for realizing a ferromagnetic semiconductor is by doping a transition metal into the host semiconductor lattice, producing a diluted magnetic semiconductor (DMS)[10]. The dopants, including Mn, Co, and Fe, exhibit uncompensated electron spins in partially occupied 3*d* orbitals, which can induce long-range ferromagnetism in the host materials. These materials provide valuable functionalities in spintronic devices as their magnetic properties, particularly the Curie temperature and coercivity, can be controlled by electric currents[11]. The main challenge associated with DMS materials is the room-temperature ferromagnetism without segregation, metallic clusters, or changes in structure. Furthermore, DMS-based oxides have the potential for super-exchange interactions that result in compensated spin states between the doped and host elements, resulting in net magnetization[12]. For two decades, a perfectly uniform and homogenous film has been believed to be the route to the goal, whilst tuning the material composition has produced controversial results. However, the origin of the magnetization is still under debate[13,14].

Therefore, an alternative method for producing robust ferromagnetic DMS materials is needed. A notable study by Chakraborty et al. revealed a promising avenue: introducing low concentrations of nanoscale inhomogeneities into DMS materials resulted in a significant enhancement of the critical temperature[15]. Nevertheless, the implementation, particularly, the formation, control, and quantification of nanoscale inhomogeneities within these films, was challenging. Therefore, the primary goal of this study is to tackle these challenges. Co-doped ZnO (ZnO:Co) was selected for its high solubility[16] and predicted ferromagnetic behavior at room-temperature (300 K)[10]. Nanoscale inhomogeneity formation was achieved by introducing nitrogen during deposition, followed by thermal annealing. This technique, known as the nitrogen-mediated crystallization (NMC) method[17–19]**,** facilitates the control of the size and density of crystal grains.

Rare-earth iron garnets (REIG) have attracted considerable attention in the field of spintronics owing to their distinctive ferrimagnetic insulating properties, which allow spin waves to propagate over long distances[20–22]. These materials, which exploit the spin-orbit torque to modulate the magnetic moment[22], are being investigated as potential candidates for energy-efficient magnetic memory and logic devices[23]. The perpendicular magnetic anisotropy (PMA), coupled with the weakened magnetic moment resulting from compensated ferrimagnetism, offers advantages conducive to integrated system applications[22,24–26]. Thulium iron garnet ($Tm_3Fe_5O_{12}$, TmIG), a member of the REIG family, has garnered significant attention for its PMA properties[24,27–29]. Its large magnetostriction constant creates a nanoscale lattice expansion when grown on a gadolinium gallium garnet ($Gd_3Ga_5O_{12}$, GGG) (111) substrate, effectively counteracting the shape anisotropy effects. Remarkably, observations of spin-orbit torque (SOT) switching[22,30] and skyrmion transport[26,31] phenomena in TmIG multilayers, exemplified by Pt/TmIG/GGG configurations, suggest the potential for achieving highly efficient magnetization switching and exceedingly rapid chiral domain-wall motion.

The advancement of TmIG film research requires a concerted effort to bridge the gap between research and industrial application. Currently, TmIG film fabrication is predominantly accomplished by deposition techniques such as pulsed laser deposition (PLD)[32–34] and off-axis sputtering[27–29]. However, sputtering is more suitable than PLD for large-scale manufacturing, owing to several factors. These include the inherent limitations

of PLD, such as the limited film area, challenges associated with particle coalescence in the ablated film, and nonuniform deposition patterns leading to droplet formation, all of which hinder the fabrication of multilayer structures[35,36]. Conversely, on-axis sputtering, a widely used method for the industrial-scale growth of oxide thin films[37], holds great promise for fabricating TmIG films. However, the lack of research exploring the application of on-axis sputtering in TmIG films remains a notable gap in the current knowledge. This study addresses this gap by detailing the successful fabrication of TmIG films exhibiting PMA, using on-axis sputtering complemented by post-annealing treatment. The PMA of TmIG is attributed to the lattice-constant strain induced by the lattice mismatch between the substrate and the film[24,38].

This dissertation has two primary objectives. First, to investigate the effect of the nanoscale inhomogeneity in Co-doped ZnO films, induced by nitrogen (ZnO:CoN), on the structure and magnetic properties. Second, to obtain TmIG with PMA through the nanoscale straining of the lattice fabricated by on-axis sputtering. To achieve these stated goals, the following research steps were implemented:

1. Create nanoscale inhomogeneity in ZnO:Co films by NMC and compare it with that of the films created without NMC.
2. Control the nanoscale inhomogeneity in ZnO:CoN by varying the postannealing time and quantify it using EDX analyses.
3. Achieve PMA in TmIG films grown via on-axis sputtering by systematically tuning the Tm/Fe ratio by modifying the Ar/O_2 ratio, pressure, and angle between the target and substrate.

This dissertation comprises six chapters, each outlined briefly as follows:

Chapter 1 summarizes the background and objective and presents an outline of the study.

Chapter 2 reviews the fundamentals and theories of sputtering deposition, DMSs, magnetic insulators, and various characterization techniques.

Chapter 3 presents the formation of nanoscale inhomogeneity in ZnO:Co films through NMC and compares these results with that of films grown without NMC.

Chapter 4 explores the control and quantification of nanoscale inhomogeneity in ZnO:CoN films.

Chapter 5 demonstrates the large-scale fabrication of TmIG films exhibiting PMA, through on-axis sputtering.

Chapter 6 provides a comprehensive summary of the experimental findings and outlines the prospects for the future development of magnetic-oxide films, especially for DMS and REIG materials.

References

1. A. Hirohata, K. Takanashi, *J. Phys. D. Appl. Phys.* **47** (2014), doi:10.1088/0022-3727/47/19/193001.

2. M. N. Baibich, J. M. Broto, A. Fert, F. N. Van Dau, F. Petroff, P. Eitenne, G. Creuzet, A. Friederich, J. Chazelas, *Phys. Rev. Lett.* **61**, 2472–2475 (1988).

3. G. Binasch, P. Grünberg, F. Saurenbach, W. Zinn, *Phys. Rev. B.* **39**, 4828–4830 (1989).

4. J. Puebla, J. Kim, K. Kondou, Y. Otani, *Commun. Mater.* **1**, 1–9 (2020).

5. Y. Cao, G. Xing, H. Lin, N. Zhang, H. Zheng, K. Wang, *iScience*. **23**, 101614 (2020).

6. M. Tanaka, *Jpn. J. Appl. Phys.* **60** (2020), doi:10.35848/1347-4065/abcadc.

7. A. V. Chumak et al., *IEEE Trans. Magn.* **58** (2022), doi:10.1109/TMAG.2022.3149664.

8. A. Brataas, B. van Wees, O. Klein, G. de Loubens, M. Viret, *Phys. Rep.* **885**, 1–27 (2020).

9. V. E. Demidov, S. Urazhdin, G. de Loubens, O. Klein, V. Cros, A. Anane, S. O. Demokritov, *Phys. Rep.* **673**, 1–31 (2017).

10. T. Dietl, H. Ohno, F. Matsukura, J. Cibert, D. Ferrand, *Science (80-.).* **287**, 1019–1022 (2000).

11. D. D. Awschalom, M. E. Flatté, *Nat. Phys.* **3**, 153–159 (2007).

12. N. A. Spaldin, *Magnetic Materials ; Fundamentals and Application* (Cambridge University Press, Second., 2011).

13. C. Song, X. J. Liu, K. W. Geng, F. Zeng, F. Pan, B. He, S. Q. Wei, *J. Appl. Phys.* **101** (2007), doi:10.1063/1.2732432.

14. X. Luo, L. T. Tseng, Y. Wang, N. Bao, Z. Lu, X. Ding, R. Zheng, Y. Du, K. Huang, L. Shu, A. Suter, W. T. Lee, R. Liu, J. Ding, K. Suzuki, T. Prokscha, E. Morenzoni, J. B. Yi, *ACS Appl. Mater. Interfaces*. **10**, 22372–22380 (2018).

15. A. Chakraborty, R. Bouzerar, S. Kettemann, G. Bouzerar, *Phys. Rev. B - Condens. Matter Mater. Phys.* **85**, 1–7 (2012).

16. P. Kumari, K. P. Misra, S. Chattopadhyay, S. Samanta, *Mater. Today Proc.* **43**, 3297–3302 (2021).

17. K. Kuwahara, N. Itagaki, K. Nakahara, D. Yamashita, G. Uchida, K. Kamataki, K. Koga, M. Shiratani, *Thin Solid Films*. **520**, 4674–4677 (2012).

18. I. Suhariadi, N. Itagaki, M. Shiratani, *ACS Appl. Nano Mater.* **3**, 2480–2490 (2020).

19. N. Itagaki, K. Kuwahara, K. Matsushima, D. Yamashita, H. Seo, K. Koga, M. Shiratani, *Opt. Eng.* **53**, 087109 (2014).

20. Y. Kajiwara, K. Harii, S. Takahashi, J. Ohe, K. Uchida, M. Mizuguchi, H. Umezawa, H. Kawai, K. Ando, K. Takanashi, S. Maekawa, E. Saitoh, *Nature*. **464**, 262–266 (2010).

21. H. Nakayama, M. Althammer, Y. T. Chen, K. Uchida, Y. Kajiwara, D. Kikuchi, T. Ohtani, S. Geprägs, M. Opel, S. Takahashi, R. Gross, G. E. W. Bauer, S. T. B. Goennenwein, E. Saitoh, *Phys. Rev. Lett.* **110**, 1–5 (2013).

22. C. O. Avci, A. Quindeau, C. F. Pai, M. Mann, L. Caretta, A. S. Tang, M. C. Onbasli, C. A. Ross, G. S. D. Beach, *Nat. Mater.* **16**, 309–314 (2017).

23. H. Bai, Z. Z. Zhu, J. T. Ke, G. Li, J. Su, Y. Zhang, T. Zhu, J. W. Cai, *Phys. Rev. Appl.* **17**, 1–9 (2022).

24. M. Kubota, A. Tsukazaki, F. Kagawa, K. Shibuya, Y. Tokunaga, M. Kawasaki, Y. Tokura, *Appl. Phys. Express*. **5** (2012), doi:10.1143/APEX.5.103002.

25. J. J. Bauer, E. R. Rosenberg, S. Kundu, K. A. Mkhoyan, P. Quarterman, A. J. Grutter,

B. J. Kirby, J. A. Borchers, C. A. Ross, *Adv. Electron. Mater.* **6** (2020), doi:10.1002/aelm.201900820.

26. S. Vélez, S. Ruiz-Gómez, J. Schaab, E. Gradauskaite, M. S. Wörnle, P. Welter, B. J. Jacot, C. L. Degen, M. Trassin, M. Fiebig, P. Gambardella, *Nat. Nanotechnol.* **17**, 834–841 (2022).

27. C. N. Wu, C. C. Tseng, K. Y. Lin, C. K. Cheng, S. L. Yeh, Y. T. Fanchiang, M. Hong, J. Kwo, *AIP Adv.* **8**, 6–12 (2018).

28. C. N. Wu, C. C. Tseng, Y. T. Fanchiang, C. K. Cheng, K. Y. Lin, S. L. Yeh, S. R. Yang, C. T. Wu, T. Liu, M. Wu, M. Hong, J. Kwo, *Sci. Rep.* **8** (2018), doi:10.1038/s41598-018-29493-5.

29. G. Vilela, H. Chi, G. Stephen, C. Settens, P. Zhou, Y. Ou, D. Suri, D. Heiman, J. S. Moodera, *J. Appl. Phys.* **127** (2020), doi:10.1063/1.5135012.

30. C. O. Avci, E. Rosenberg, M. Baumgartner, L. Beran, A. Quindeau, P. Gambardella, C. A. Ross, G. S. D. Beach, *Appl. Phys. Lett.* **111** (2017), doi:10.1063/1.4994050.

31. S. Ding, A. Ross, R. Lebrun, S. Becker, K. Lee, I. Boventer, S. Das, Y. Kurokawa, S. Gupta, J. Yang, G. Jakob, M. Kläui, *Phys. Rev. B.* **100**, 100406 (2019).

32. O. Ciubotariu, A. Semisalova, K. Lenz, M. Albrecht, *Sci. Rep.* **9**, 1–8 (2019).

33. C. Tang, P. Sellappan, Y. Liu, Y. Xu, J. E. Garay, J. Shi, *Phys. Rev. B.* **94**, 1–5 (2016).

34. E. R. Rosenberg, K. Litzius, J. M. Shaw, G. A. Riley, G. S. D. Beach, H. T. Nembach, C. A. Ross, *Adv. Electron. Mater.* **7**, 1–11 (2021).

35. D. H. A. Blank, M. Dekkers, G. Rijnders, *J. Phys. D. Appl. Phys.* **47** (2014), doi:10.1088/0022-3727/47/3/034006.

36. D. Fischer, G. F. De La Fuente, M. Jansen, *Rev. Sci. Instrum.* **83** (2012), doi:10.1063/1.3697861.

37. U. Betz, M. Kharrazi Olsson, J. Marthy, M. F. Escolá, F. Atamny, *Surf. Coatings Technol.* **200**, 5751–5759 (2006).

38. C. N. Wu, C. C. Tseng, K. Y. Lin, C. K. Cheng, S. L. Yeh, Y. T. Fanchiang, M. Hong, J. Kwo, *AIP Adv.* **8** (2018), doi:10.1063/1.5006673.

Chapter 2

Principle and Fundamental Theory

2.1 Sputtering Deposition

Sputtering, pioneered by W. R. Groove in 1852, is a prominent physical vapor deposition technique for fabricating thin films across both research and industrial scales[1]. As shown in Fig. 2.1, the sputtering process involves the ejection of atoms from a solid target source through bombardment, driven by high-energy ions within a partially ionized plasma environment comprising both ions and electrons. These ions typically originate from an inert gas ambient, such as argon. Subsequently, the ejected particles are deposited or condensed onto a substrate, forming a thin film.

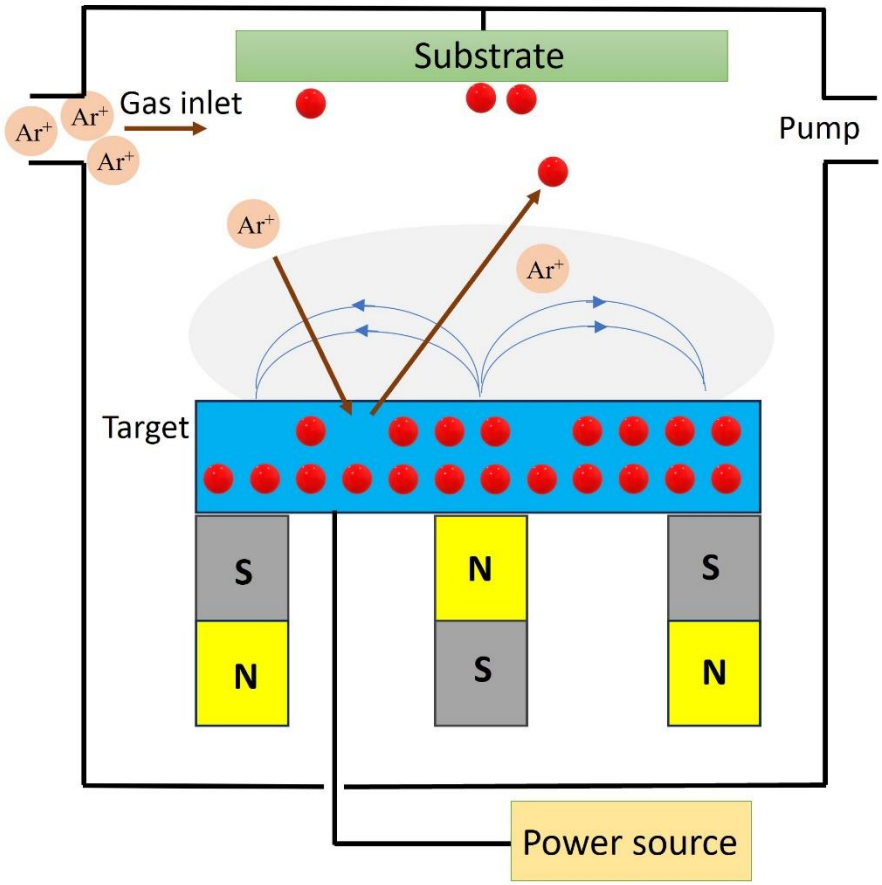

Figure 2.1 Illustration of RF magnetron sputtering process.

Sputtering deposition is categorized into two main types, based on the power applied to the target: direct current (DC) and radio frequency (RF) sputtering. In DC sputtering, a constant negative voltage (typically, in the kV range) is applied to the target material. This voltage serves to accelerate naturally occurring positive ions within the noble gas toward the target surface. Upon collision with the target material, these energized ions

prompt the ejection of atoms, which subsequently migrate toward the substrate, ultimately forming a thin film. However, the accumulation of the positive ions on the target surface over time reduces the efficiency of the sputtering mechanism. Although this issue is not usually observed in conductive targets, insulating materials such as REIG face these challenges during DC sputtering. An alternative approach is to employ RF power, wherein alternating potential cycles effectively clean the accumulated positive charges on the target during the positive cycle and attract ions for sputtering during the negative cycle. The industry-standard RF allocated by international communication authorities is typically set at 13.56 MHz to avoid interference with communication systems. To ensure optimal performance, the impedance of the RF plasma must be matched to the standard 50 Ω impedance of the RF generator.

An effective strategy to improve the sputter deposition, by increasing the deposition rates, reducing the voltage requirements, and extending the operating pressure range, is to apply a static magnetic field within the sputtering system, known as magnetron sputtering[2,3]. A set of magnets is positioned behind the target to capture additional electrons ejected from the target by ion bombardment. This configuration, known as a magnetron, generates a concentration of ion flux near the target. The effect of the magnetic field (B) in the sputtering system to trap the electron (e) close to the target surface (r) can be described using the Lorentz force, as follows :

$$r = \frac{vm_e}{Be} \tag{2.1}$$

Where v and m_e are velocity and mass of electron. By trapping additional electrons, the magnetron prevents them from reaching the substrate, increasing the probability of an ionizing electron–atom collision and forming a dense plasma in the target region. This leads to increased ion bombardment of the target, resulting in higher sputtering rates. The correlation between the sputtering rate (R) and ion number can be expressed as follows[1]:

$$R = \sum_j^N Y_j \frac{J_{i,j}}{e} \frac{1}{n_t} \tag{2.2}$$

where Y_j is the sputter yield, defined as the average number of atoms ejected from the target for each incident ion. J_i and n_t are the ion current density and atomic density of the target, respectively. The enhanced ionization efficiency achieved in the magnetron mode allows the

discharge to be maintained at lower operating pressures and voltages.

Figure 2.2 Photograph of RF magnetron sputtering systems. a). for ZnO:Co film and b). for TmIG films.

RF magnetron sputtering presents numerous advantages in the fabrication of magnetic oxide films, including precise control over deposition rate and composition, uniformity across large areas, tunability of magnetic properties, and ability to achieve high film quality. Its compatibility with various substrate materials further enhances its appeal, making it a versatile and efficient technique in magnetic-oxide film fabrication. The dependence of magnetic properties on the thickness demonstrates the pivotal role of deposition-rate control in magnetic oxide films. Among DMS materials, ZnO:Co exhibits the highest saturation moment when the strain reaches its highest value and lowest thickness[4]. Controlling the thickness has proven to be an effective strategy in inducing PMA in REIG materials such as yttrium iron garnet (YIG)[5] and TmIG[6,7]. The control of composition is a critical aspect of tuning magnetic properties in magnetic-oxide films. The saturation magnetization of the ZnO:Co film can be adjusted by varying the concentration of Co[8,9]. The introduction of bismuth as a substitution element in YIG and TmIG effectively induces lattice strain, producing PMA. The versatility of RF magnetron sputtering across a range of substrate materials holds significant importance, as it facilitates the exploitation of the lattice mismatch phenomena to attain PMA in REIG materials such as YIG on $Gd_3Sc_2Ga_3O_{12}$

(GSGG)[10–12], $Gd_{0.63}Y_{2.37}Sc_2Ga_3O_{12}$ (GYSGG)[10,11], and $Gd_{2.6}Ca_{0.4}Ga_{4.1}Mg_{0.25}Zr_{0.65}O_{12}$ (SGGG)[11,13] and TmIG on $Gd_3Ga_5O_{12}$ (GGG) substrates[7,14,15].

In this study, RF magnetron sputtering was employed to explore the nanostructure effect of uncompensated spin ensembles in oxide films; with specific emphasis on Co-doped ZnO, for controlling and quantifying nanoscale inhomogeneities, and TmIG films, for inducing lattice strain to achieve PMA using an on-axis deposition geometry.

2.2 Magnetic Semiconductors

2.2.1 *Introduction to Magnetic Semiconductors*

The fabrication of materials that combine both charge and spin functionalities of the carrier can transform technology by producing new devices that can exhibit improved performance and reduced power consumption. The utilization of both the spin and charge of the electron is commonly referred to as spintronics. The injection of spin-polarized electrons using ferromagnetic metals coated on metal–semiconductor junctions has been inefficient because of the formation of detrimental interfacial films and carrier scattering due to impedance mismatch. Therefore, the substitution of magnetic ions in the cations of the host semiconductor, referred to as DMS has been recognized as a new method to realize magnetic-semiconductor functionality. Transition metals such as Co and Mn are widely recognized as common dopants for DMSs, owing to their partially filled *d* orbitals, which possess the potential to couple with electrons within the semiconductor host. This coupling can produce various unique and intriguing structural, electrical, and magnetic properties.

The Curie temperature and origin of magnetism are the main factors for the realization of devices based on DMS materials. Dietl et al[16]. predicted that the Curie temperatures of transition-metal–doped ZnO and GaN could rise above room-temperature, a result that attracted much attention in the DMS research field. A perfectly uniform and homogenous film has been believed to be the route to the goal for two decades, whilst tuning the material composition such as adjusting Co concentration[9,17–19], oxygen vacancies[20–22], and zinc interstitial defects[23,24], has produced controversial results. Therefore, an alternative method for producing robust ferromagnetic DMS materials is needed. A notable study by Chakraborty et al. revealed a promising avenue: introducing low concentrations of nanoscale inhomogeneities into DMS materials resulted in a significant enhancement of the critical

temperature[25].

Recently, NMC using RF magnetron sputtering was developed to grow ZnO thin films, potentially inducing inhomogeneity in the film. In this protocol, ZnO is sputtered in an argon and nitrogen atmosphere, followed by thermal annealing. The N atoms adsorbed during deposition interfere with the crystallization of ZnO. The nitrogen is then replaced by oxygen in the post-annealing process, which induces solid-state crystallization. The size and density of crystal grains can be controlled by controlling the annealing temperature and time[26–28], prompting the author to realize nanoscale-inhomogeneity–based DMS. In this study, the effect of nanoscale inhomogeneities on Co-doped ZnO (ZnO:Co) films fabricated by the NMC method is investigated. A new analytical method is demonstrated to quantify the nanoscale inhomogeneity, which is believed to increase the critical temperature in DMS.

2.2.2 *Origin of Magnetism of DMS*

Although the fundamental understanding of the origin of ferromagnetism is still controversial, several theoretical models have attempted to explain the ferromagnetism observed in these systems. In the direct exchange interaction, the proximity of magnetic moments allows their wave functions to directly overlap, inducing magnetic coupling. This coupling is robust but limited in range and diminishes rapidly as the magnetic ions move apart. It is typically not predominant in most DMSs, because of the relatively large interatomic separation. The direct-interaction coupling (j) of spins ($\boldsymbol{s}_i$) is expressed using the Heisenberg Hamiltonian, as follows[29]:

$$H_{ex} = -\sum_{ij} \boldsymbol{j}_{ij} \boldsymbol{s}_i \cdot \boldsymbol{s}_j \tag{2.3}$$

Fig 2.3 illustrates the correlation between $\boldsymbol{j}$ and the interatomic distance (r). Positive and negative J values denote parallel and antiparallel spin configurations, respectively. Direct exchange interaction operates over short distances only[29]. With increasing interatomic distance, the wavefunction overlap decreases, leading to paramagnetic behavior[30].

Indirect exchange refers to the magnetic interaction between two magnetic ions, which is facilitated by a medium such as free carriers, and includes super-exchange, double-exchange, and Ruderman-Kittel-Kasuya-Yosida (RKKY) interactions[29]. Super-exchange, an indirect exchange interaction commonly observed in transition-metal oxides and related materials, involves magnetic interactions between neighboring magnetic ions, mediated by

nonmagnetic neighboring anions. This occurs when the magnetic ions are too distant for direct exchange. As a result of the *sp–d* exchange interactions, electrons originating from the negative anions transfer to the vacant *d*-orbitals of the magnetic ions. These electrons then interact with the localized spins of the magnetic ions, resulting in antiferromagnetic coupling between neighboring magnetic ions. A classic example is manganese oxide (MnO), where the interaction between two Mn atoms is mediated by oxygen through the overlap of oxygen *2p* and Mn *3d* orbitals.

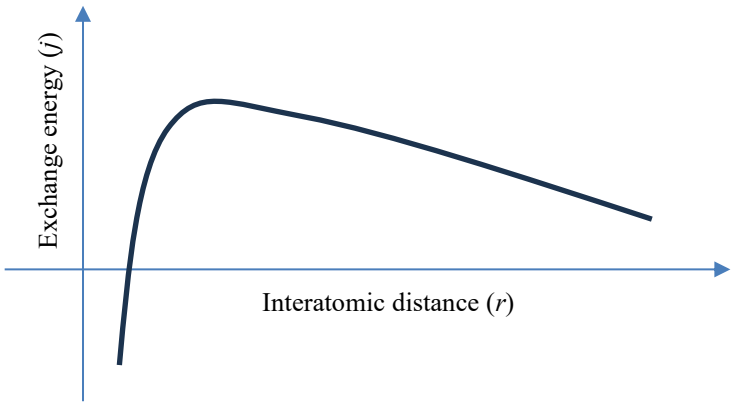

Figure. 2.3 Interatomic distance as a function of direct exchange energy

Double exchange is the interaction between two metal ions with differing valence states, through an anion. This interaction involves electron hopping and occurs when one of the atoms possesses an additional electron. The exchange of this electron can induce magnetism. For instance, in manganese perovskites like $LaMnO_3$, doping has been observed to enhance both the electron conduction and ferromagnetic coupling by altering the valence state of the Mn ion from 3+ to a mixed state of 3+ and 4+. The electron can traverse between the two metal ions via an intermediary such as oxygen. Following Hund's rule, the electron retains its spin direction during hopping, leading to ferromagnetic coupling. Unlike super-exchange, double exchange involves mediation by charge carriers.

The RKKY interaction, proposed by Ruderman, Kittel, Kasuya, and Yosida, is a form of indirect exchange that prevails when there is no direct overlap of wavefunctions among magnetic electrons. Consequently, it relies on an intermediary such as nonmagnetic conduction electrons. Operating over long distances, the RKKY interaction involves a

magnetic ion polarizing the surrounding conduction electrons and subsequently transferring this polarization to other magnetic ions. This process can result in either ferromagnetic or antiferromagnetic coupling, contingent upon the distance between the ions. This interaction is expressed as follows[31]:

$$J(r) = 9\pi \frac{J_0^2}{E_F} F(2K_F r) \tag{2.4}$$

$$F(x) = \frac{x\,cosx - sinx}{x^4} \tag{2.5}$$

where J, E_F, K_F, and r are the exchange interaction, Fermi energy, radius of the Fermi surface, and distance between two magnetic ions. As depicted in Fig. 2.4, the sign of the RKKY exchange interaction (J) oscillates from positive to negative as the distance (r) between two magnetic ions increases. At shorter distances, the magnetic interaction demonstrates the most robust ferromagnetic coupling[30].

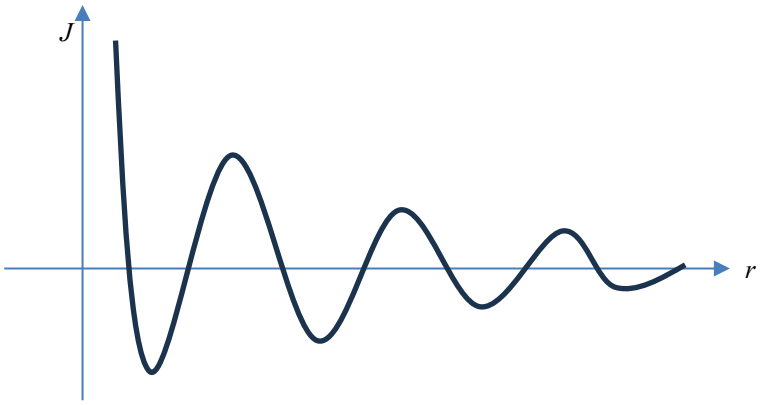

Figure 2.4 RKKY interaction as function of distance between magnetic ions

The bound magnetic polaron (BMP) model has gained attention following recent findings of high-temperature ferromagnetism in low-carrier-density systems. These reports suggest that free-carrier mediation alone cannot fully explain the mechanism behind long-range ferromagnetic ordering. Furthermore, the presence of such ordering at very low concentrations of magnetic ions cannot be explained solely by short-range exchange interactions such as double exchange or super-exchange. A defect-mediated approach, such as the BMP exchange model, provides an explanation for this phenomenon. BMP is generated through the interaction of vacancies with weakly bound carriers that adopt

extended orbits. The emergence of ferromagnetic behavior is contingent upon the pairing of shallow donor electrons with defects such as oxygen vacancies, which subsequently generates of BMPs, resulting in the generation of a spin-split band[32].

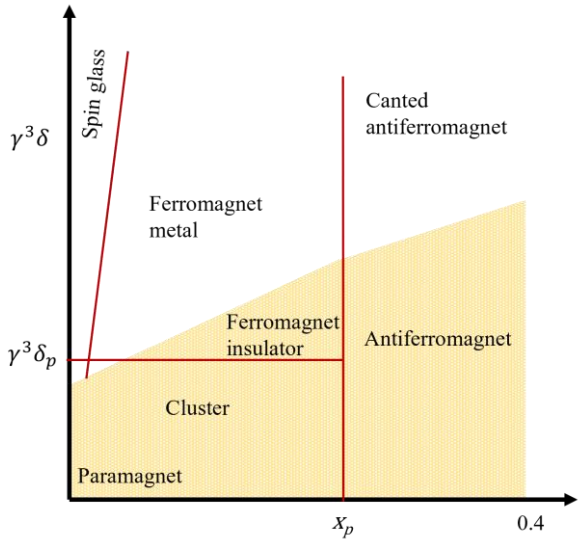

Figure 2.5 Magnetic state diagram for DMS[32]

The magnetic state diagram based on the BMP model was first introduced by Coey et al. (Fig. 2.5)[32]. This diagram elucidates how the magnetic state of a material is influenced by several key factors including the donor concentration (δ), concentration of the doped element (x), and ratio between hydrogenic radius (r_h) and Bohr radius (a_0) as coefficient γ. Two critical thresholds in this diagram are the doped-element concentration threshold (x_p) and donor concentration threshold (δ_p). Beyond x_p, antiferromagnetic or ferrimagnetic properties emerge because of the formation of a continuous path throughout the crystal that connects the nearest-neighbor magnetic cations. Conversely, ferromagnetic properties are observed when the donor concentration exceeds its threshold ($\delta > \delta_p$) and the doped-element concentration remains below its threshold ($x < x_p$). The BMP model can be used with both p and n-type host systems. A comparable model has been proposed, which postulates that the exchange of electrons via an F-center interaction between atoms trapped in an oxygen vacancy occupying an extended orbital results in ferromagnetic coupling between transition-metal ions positioned within that orbital[32].

2.3 Ferrimagnetic Insulator

2.3.1 *Introduction to Ferrimagnetic Insulator*

Recent advances in magnetic materials have facilitated the advancement of spintronic devices using insulating ferrimagnetic oxide films, which have advantageous properties over metallic magnets. The magnetic insulator demonstrates the ability to carry a spin current in which the spin information propagates as a wave through the material without electronic motion, owing to the nonconductivity of the material. Spin currents exhibit remarkable efficiency because the absence of electrical resistance or Joule heating in the magnetic film reduces the power consumption and cooling requirements. Energy dissipation occurs solely by dissipative magnetic damping mechanisms within the material. In addition, ferrimagnetic insulators exhibit significantly faster magnetization dynamics than the metallic bulk, extending into the terahertz frequency range[33,34]. One of the most common types of insulating magnetic oxides is the REIG.

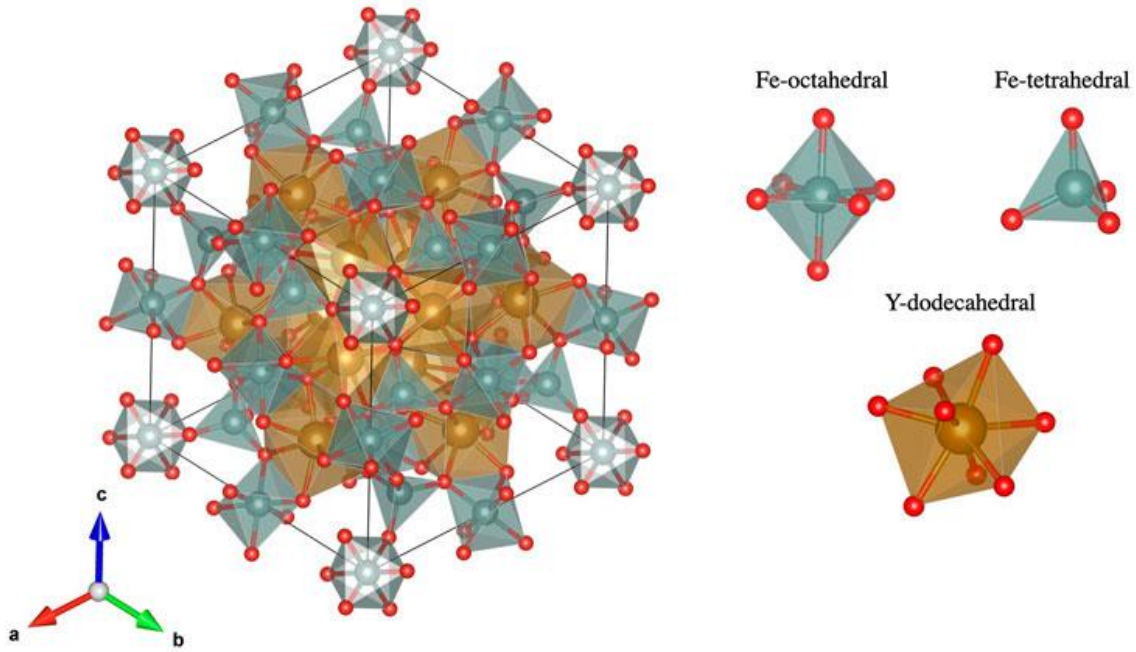

Figure 2.6 Structure of REIG[37]. Oxygen atoms are displayed in red; iron atoms are enclosed within gray octahedrals or tetrahedrals; and rare-earth atoms presented within gold dodecahedrals.

REIG are named for their structural similarity to garnet minerals such as grossularite[35], which has the chemical formula $Ca_3Al_2Si_3O_{12}$. A specific REIG variant

undergoes substitutions, with rare-earth elements replacing Ca and Fe replacing Al or Si, resulting in the formula unit $RE_3Fe_5O_{12}$. A large unit cell contains eight formula units, producing a total of 160 ions. Fig. 2.6 shows the cubic unit cell of the REIG developed by Redies[36] et al. and Momma and Izumi[37]. Oxygen ions occupy the 96h sites (Wyckoff position 20), which surround each cation. These cations encounter three unique environments, as shown in Fig. 2.6 on the right side. The rare-earth ion positioned at the 24c site resides in a dodecahedron formed with the adjacent oxygen ions. Meanwhile, the two Fe ions occupy different lattice sites: one occupies the 16a site, with a coordination number of six oxygen ions (forming an octahedron, Fe-octahedral), while the other resides at the 24d site, located in the center of a tetrahedron (Fe-tetrahedral). The ratio of the Fe-octahedral to Fe-tetrahedral is 2:3.

2.3.2 *Magnetism of REIG*

The structure of REIG consists of three different magnetic sublattices aligned at three crystallographic sites. REIG exhibits ferrimagnetic behavior in which magnetism arises from super-exchange interactions facilitated by oxygen anions. Unlike the octahedral and dodecahedral sites, the tetrahedral sites exhibit antiparallel magnetization, resulting in a net magnetization described by the equation:

$$M_t = M_{dod} + M_{oct} - M_{tet} \tag{2.6}$$

where M_t, M_{dod}, M_{oct}, and M_{tet} represent the total magnetization and the magnetic moment in the dodecahedral site, octahedral site, and tetrahedral site, on this sublattice, respectively. While antiferromagnetic superexchange interactions dominate among all sublattices, the interactions between the Fe octahedral and Fe tetrahedral as well as that between the R dodecahedral and Fe tetrahedral show significant strengths over competing interactions. As a result, the magnetic moments of the dodecahedral and octahedral sublattices are aligned ferromagnetically, meaning they are parallel to each other. This alignment implies that the Fe^{3+} ion's magnetic moment is oriented antiparallel to the moment on the rare-earth ion's dodecahedral site. The rare-earth ion significantly affects both the static and dynamic magnetic properties because the number of 4*f* electrons varies across the lanthanide series, causing substantial fluctuations in the magnetic moment.

The magnetic moment in a magnetic material has a preferential orientation along

specific directions, known as magnetic anisotropy. Magnetic anisotropy can stem from inherent characteristics of the material, such as its crystal structure or shape, or it can be deliberately induced through a meticulous selection of growth-processing techniques. The tendency of magnetization to align along a preferred crystallographic direction is called magneto-crystalline anisotropy. In the presence of asymmetric electronic orbitals ($L \neq 0$), anisotropic interactions occur between the orbitals and crystal field, resulting in specific orientations with lower orbital energies. In cubic structures such as those found in REIG, there are two main orientations: [100] and [111]. The magnetocrystalline anisotropy of a cubic material can be quantified by a series of constants K_i, as presented in the following equation:

$$E = K_1(\alpha_1^2\alpha_2^2 + \alpha_2^2\alpha_3^2 + \alpha_3^2\alpha_1^2) + K_2(\alpha_1^2\alpha_2^2\alpha_3^2) + \ \ldots \tag{2.7}$$

Here α_i represents the cosine of the angles formed by the magnetization vector with the three crystal axes. K_1 and K_2 are referred to as the first and second-order magnetocrystalline anisotropy constants, respectively, and are typically sufficient to characterize the anisotropy of a material.

The three-dimensional configuration of a material gives rise to shape anisotropy, which profoundly influences its magnetic behavior. In the context of thin films, the dipole–dipole interaction among magnetic moments predominantly promotes an in-plane orientation, defining the magnetic easy axis. Consequently, the ground state of the magnetic moments aligns within the film plane, representing the configuration of minimal energy. The density of shape anisotropy, denoted as K_s, is directly proportional to the square of the saturation magnetization M_s.

$$K_s = -\frac{1}{2}\mu_0 M_s^2 \tag{2.8}$$

where μ_0 is the vacuum permeability constant. The magnetization of thin films of materials with weak magnetocrystalline anisotropy is a consequence of the dominant shape anisotropy.

The epitaxial deposition of films onto substrates with slightly disparate lattice constants induces the creation of distorted unit cells or strain, which is known as magnetoelastic anisotropy. The epitaxial strain is classified as either compressive strain (the lattice constant of the film is larger than the substrate) or tensile strain (the lattice constant of the film is less than the substrate). The tensile strain is calculated as a percentage of the

lattice mismatch, given by[38]:

$$\epsilon = \left(\frac{a_f - a_s}{a_s}\right) \tag{2.9}$$

where a_f and a_s are the lattice constants of the film and substrate, respectively. The compressive or tensile strain of the film lattice modifies the orbitals and, through spin-orbit coupling, can change the preferred orientation of magnetization. The magnetostriction coefficient (λ) and epitaxial stress of the material are proportional to the strength of the magnetoelastic energy density. If the tensile strain is large enough, the magnetoelastic anisotropy can overcome the shape anisotropy and produce a simple axis perpendicular to the film.

PMA in REIG has attracted considerable interest in spintronic devices, by reducing the power consumption and producing high-frequency magnetization dynamics[39,40]. PMA in metallic ferromagnets poses challenges because of the stray fields, limiting bit size, and significant damping losses that limit read–write speeds and energy efficiency. Specific crystal structures exhibit distinct electric-field symmetries correlated with their respective crystal fields. Micro/nanopatterning, large strain-induced anisotropy, and substitutional doping in REIG have been reported as successful methods to achieve PMA[41].

A micro/nanopatterning method applied to YIG has successfully induced PMA[42]. This technique involves the precise etching of rectangular nanostrips with nanometer-scale thicknesses from continuous YIG films, as depicted schematically in Fig. 2.7a. This strategic fabrication requires a very low magnetic saturation field to align along the longest dimension of the YIG nanostrips. With a decrease in the length-to-thickness ratio, the influence of shape anisotropy through the film thickness diminishes, thereby favoring the establishment of PMA along the in-plane easy axis.

Strain-induced PMA in REIG, as illustrated schematically in Fig. 2.7c-d, has been proven effective in surpassing the shape magnetic anisotropy. When the magnetic-elastic anisotropy induced by crystal lattice mismatch exceeds the magnitude of shape anisotropy and exhibits an opposite sign, the easy axis of the film reorients perpendicular to the film plane. Furthermore, the magnetic-elastic anisotropy can be triggered by the disparity in lattice mismatch between the substrate and film. YIG with PMA properties has been successfully attained by utilizing $Gd_3(Sc_2Ga_3)O_{12}$ substrates[12,43]. Kubota et al. discovered

that the suppression of shape magnetic anisotropy was achievable under specific conditions. They found that when the magnetostriction coefficient (λ_{111}) reached a significant value and tensile strain was applied to the thin film, a crucial transformation occurred: the easy axis became perpendicular to the sample plane[44,45].

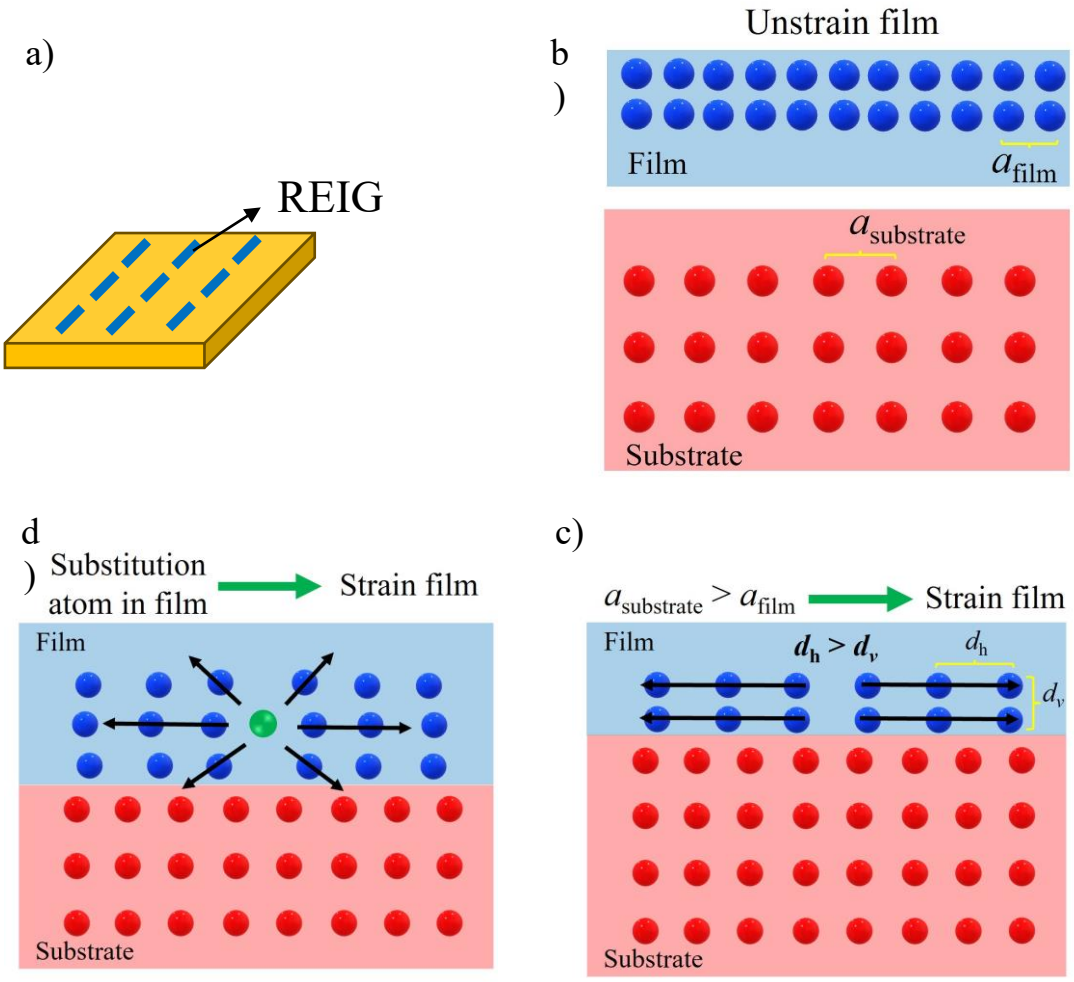

Figure. 2.7 Illustration showing the achievement of PMA in REIG films. a). Micro–nano patterning technique, b). Unstrained film, c). Strained film where strain is induced by lattice mismatch between substrate and film, and d). Strain filmed where strain is induced by using a substitution element in the film.

The utilization of the magnetostriction coefficient to induce PMA has been successfully demonstrated in various REIG materials, including TmIG[14,15,44,45], terbium iron garnet[46–48], europium iron garnet[46,48,49], and dysprosium iron garnet[50]. The use of a substitution atom in the epitaxial REIG film, as schematically shown in Fig. 2.6d, is one of the methods for obtaining PMA. The incorporation of dopant elements such as Bi[51,52], Ce[53], and Dy–Ce[54] into YIG has emerged as a successful strategy for attaining robust PMA.

2.4 Characterization Methods

2.4.1 *X-ray Fluorescence*

X-ray fluorescence (XRF) is a technique utilized to measure the elemental composition of a given sample by analyzing radiation. Typically, a primary radioactive source, predominantly photons, interacts with the sample via the photoelectric effect. Here, the photon energy can dislodge an electron from its inner orbital, provided the photon energy exceeds the electron's binding energy, typically found within the K or L shell during XRF analysis. Following this, an electron from an outer orbital transitions to occupy the vacant position, emitting energy equal to the difference between the involved orbitals, thereby generating distinct signatures for each element. This energy emission manifests as fluorescence radiation, with its intensity correlating to the energy discrepancy between the electron shells. The specific energies associated with shell ejections are contingent upon the atomic number, thereby defining the fluorescence characteristics. These emissions, termed characteristic X-rays, are subsequently captured by a detector[55]. The process of XRF is elucidated in Fig. 2.8. Electrons traverse shells encircling a positively charged nucleus, as depicted in Bohr's atomic model, which outlines various energy levels and sublevels denoted as K, L, and M. The innermost K-shell can accommodate two electrons, while the L-shell comprises three sublevels capable of hosting up to eight electrons. The M-shell consists of five sublevels and can hold up to eighteen electrons. Specific electron transitions characterize various fluorescent emissions. First, the site from which an electron is ejected is determined, as in the case of K-radiation, where an electron is removed from the K-shell and replaced by an electron from an outer shell. The origin of the replacement electron is then denoted using Greek letters: α (alpha) for a transition from one shell (e.g., L-shell to K-shell) and β (beta) for a transition spanning two shells (e.g., M-shell to K-shell). Numerical designations (1, 2, 3, etc.) specify changes within sublevels. Therefore, if an electron from sublevel 3 of the L-shell fills a vacancy in the K-shell, the fluorescence emitted would be labeled Kα1 or simply KA1. In this study, the fundamental parameter (FP) calculation method available on XRF Rigaku ZSX Primus II was used for confirming the film compositions of both ZnO:Co and TmIG.

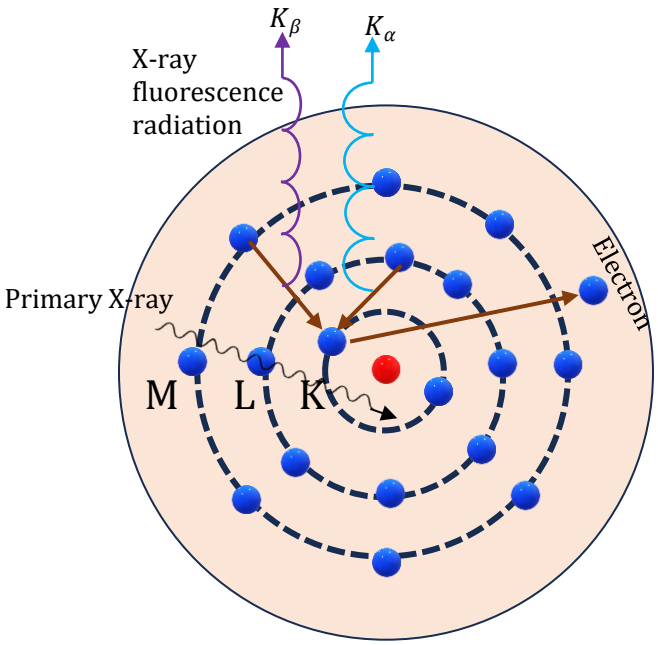

Figure 2.8 Illustration of the XRF principle.

2.4.2 *X-ray Photoelectron Spectroscopy*

X-ray photoelectron spectroscopy (XPS) is a surface chemical-analysis technique that provides quantitative spectroscopic insights. In XPS, when photons with energies surpassing the binding energy of electrons are absorbed by a material, core electrons are ejected (Fig. 2.9). The excess energy is then converted into kinetic energy of the emitted photoelectrons, which can be measured using an electron analyzer[56]. Determining the binding energy becomes straightforward by knowing the incident photon energy and the spectrometer's work function. XPS displays remarkable sensitivity to an element's chemical state, where shifts in binding energy, known as chemical shifts, and the arrangement of XPS peaks are crucial for understanding the local coordination within materials. This study primarily focuses on analyzing DMS films to understand their composition, dopant chemical states, and atomic bonding characteristics. Of particular importance is determining Co's oxidation state in ZnO, which is crucial for assessing the potential for localized 3*d* electron spins, essential for inducing ferromagnetism in ZnO DMS films.

Additionally, examining the bonding state of oxygen atoms in both as-deposited and annealed films provides insights into the relative abundance of native defects such as oxygen

vacancies, which are believed to significantly affect the film's ferromagnetic properties. The investigation employed the Shimadzu-KRATOS XPS, with all binding energies referenced to the C 1s peak at 284.6 eV.

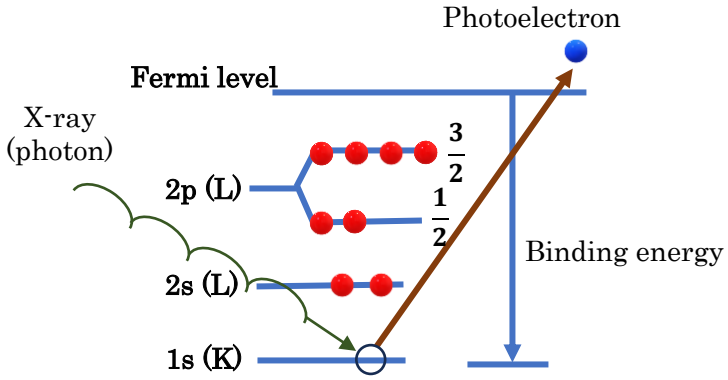

Figure 2.9 Schematic of photoelectron generation in XPS measurement.

2.4.3 *Thermal desorption spectroscopy*

Thermal desorption spectroscopy (TDS) is a method for analyzing the desorption kinetics of chemical species from solid surfaces under controlled heating at low pressures. This technique measures the partial pressures of desorbed atoms and molecules while precisely regulating the heating rate[57]. The process is carried out in a continuously pumped ultrahigh vacuum chamber. When the pumping speed is sufficiently high, compared to the pressure changes caused by desorbed gases, the variation in partial pressure is proportional to the desorption rate. A mass spectrometer is employed to monitor the partial pressures of the gases. Within the mass spectrometer, the desorbed gases are ionized by electrons emitted from a filament, then separated based on their mass-to-charge ratios as they pass through the analyzer, and ultimately detected and recorded by an ion detector. The resulting ion current is proportional to the partial pressures, and hence, to the desorption rates of specific species. A schematic representation of TDS is presented in Fig. 2.10.

This study used TDS WA1000, which is equipped with a quadrupole mass spectrometer. The working chamber was vacuumed to below 7×10^{-8} Pa before heating. The heating was monitored and controlled using a thermocouple under the sample stage. The temperature on the surface of the sample was using the thermocouple. TDS measurement

was conducted to reveal the desorption–absorption of elements in the ZnO:Co film. The heating rate for this instrument was 60 °C/min.

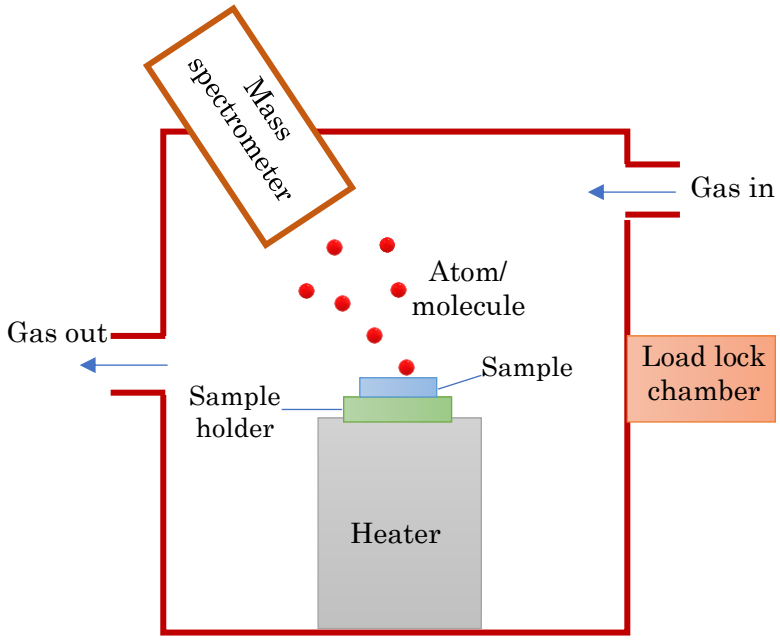

Figure 2.10 Schematic of TDS measurement.

2.4.4 *Energy-dispersive X-ray Spectroscopy*

EDX is a crucial analytical tool for determining the composition of a sample through the analysis of X-rays emitted after the incidence of an electron beam. Upon interaction with the electron beam, an inner shell electron is displaced, creating an electron vacancy. Subsequently, an electron from a higher energy shell fills this vacancy, resulting in the emission of X-rays corresponding to the energy differential between the involved electron shells (Fig. 2.11).

Typically falling within the X-ray frequency range of the electromagnetic spectrum, this phenomenon is pivotal in electron microscopy for X-ray detection. Notably, electron shells are denoted by specific labels such as K, L, and M, with K representing the innermost shell and M the outermost. Prominent transitions associated with these energy levels include Kα (L to K transition), Kβ (M to K transition), and Lα (M to L transition). Each chemical element manifests distinct energy disparities within its electron shells, facilitating the precise identification and characterization of individual elements[58]. In this study, the inhomogeneity

of ZnO:Co films was quantitatively examined using EDX JEM-ARM200F.

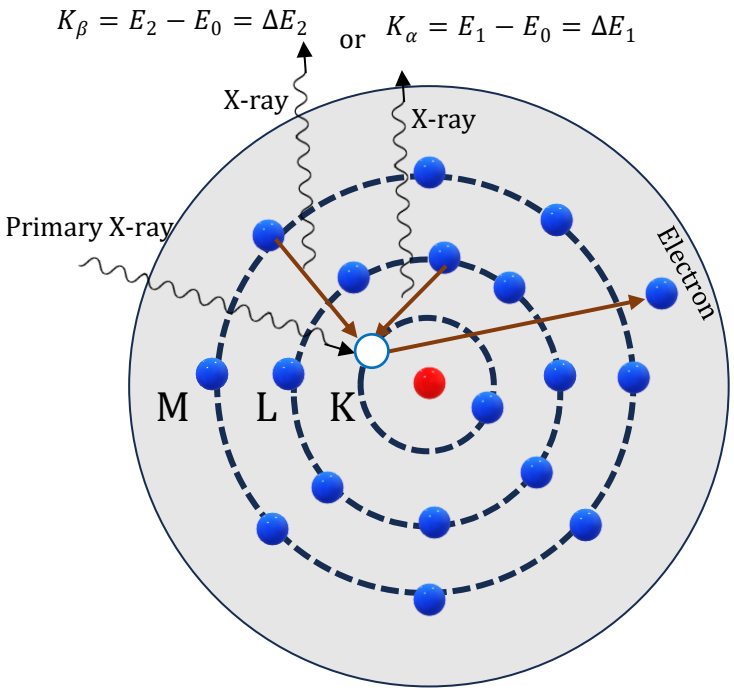

Figure 2.11 Schematic of EDX measurement.

2.4.5 *Transmission electron microscopy*

Transmission electron microscopy (TEM), with its diverse imaging modes and analytical techniques, has become an indispensable tool for the chemical and structural analysis of materials at the nanoscale. The image formation process in TEM can be delineated into two distinct stages. Initially, incident electrons interact with the atoms of the specimen, engaging in both elastic and inelastic scattering phenomena. Subsequently, the electron wavefunction emerging from the exit surface of the specimen traverses through the objective lens and successive magnifying lenses of the electron microscope, culminating in the production of the final magnified image[59].

In this study, phase contrast imaging, known as high-resolution TEM (HR-TEM), is used to visualize the crystal structure of ZnO:Co films. HR-TEM now provides the remarkable capability to explore the atomic arrangement of solid-state materials with a resolution reaching approximately 0.08 nm[60]. As shown in Fig. 2.12, HR-TEM uses a large

objective aperture to selectively capture multiple electron beams, including direct and diffracted beams, to construct images.

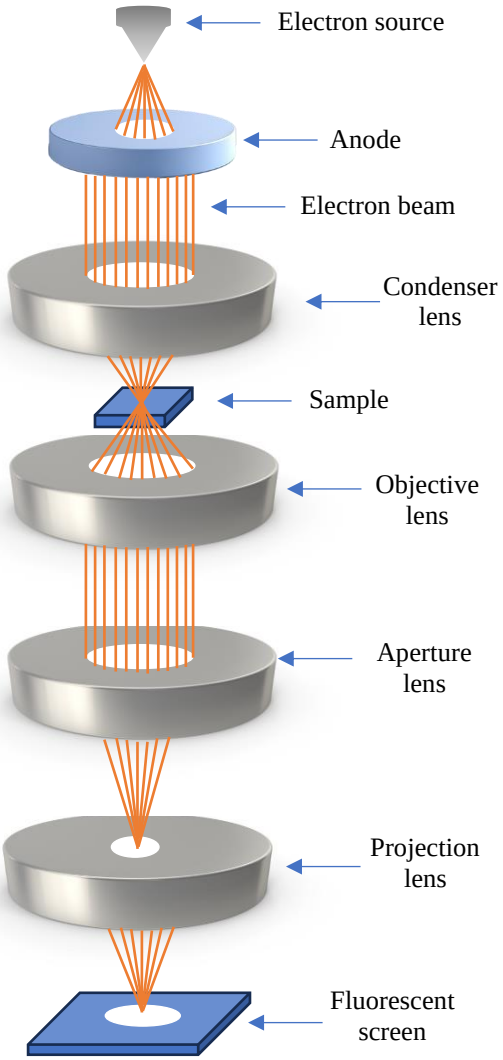

Figure 2.12 Illustration of TEM measurement.

The interaction of electron waves with the sample modulates their phase relative to the un-scattered wave, resulting in interference patterns that generate contrast in the image. This reveals the periodicity of the crystal lattice as lattice fringes. Accurate sample orientation along a zone axis is crucial for visualizing the crystal lattice through the lattice fringe spacing. Cross-sectional HR-TEM was performed to investigate the nanoscale inhomogeneity of ZnO:Co for as-deposited and post-annealing times (8 h).

2.4.6. *Atomic Force Microscopy*

Atomic Force Microscopy (AFM) stands as a superlative, high-resolution form of scanning probe microscopy, renowned for its efficacy in quantifying and visualizing sample topography at the nanoscale. In AFM, elucidating the sample's topographical characteristics relies on the interaction between the sample surface and a mechanical probe during measurement[61]. This probe typically features an exceedingly diminutive and acute tip affixed to the extremity of a cantilever, which may be fabricated from either single-crystalline silicon or silicon dioxide. Two principal methodologies are employed to gauge the force between the surface and the probe, as shown in Fig. 2.13.

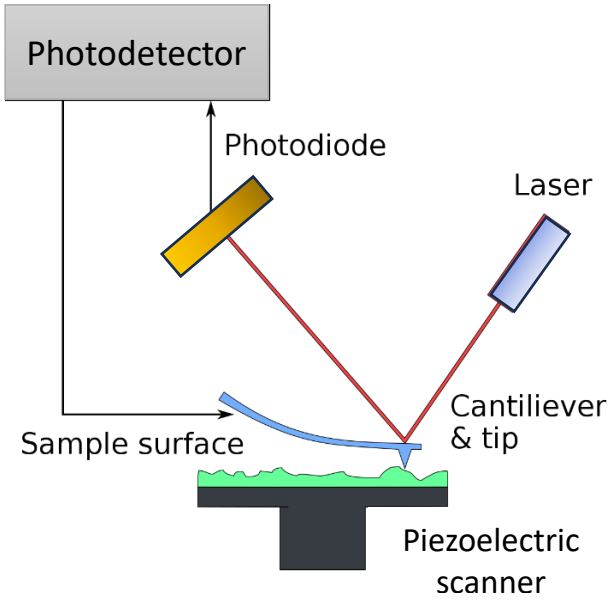

Figure 2.13 Schematic of AFM measurement.

The first, contact mode, entails direct contact between the tip and the sample surface, with the dominant interaction force arising from Van der Waals interactions. Conversely, tapping mode, a non-contact modality, involves the application of a drive signal, typically characterized by standard frequencies, to the "Tapping Piezo," thereby inducing mechanical oscillations of the probe at its resonance frequency. The interaction between the tip and the sample surface modulates the amplitude or phase of the cantilever oscillation relative to the drive signal. The AFM technique was harnessed to investigate the surface morphology of films. In this study, the surface roughness of the ZnO:Co and TmIG films was investigated using the Hitachi AFM 5100N instrument.

2.4.7. *Surface profilometer*

The thickness of the deposited films, especially for ZnO:Co film, was measured using Veeco Dektak 150 profilometer. The Dektak 150 Profiler utilizes an electromechanical approach for precise measurements, where the sample is dynamically traversed beneath a diamond-tipped stylus. A meticulously engineered stage orchestrates this movement, executing user-defined parameters such as scan length, velocity, and stylus pressure with exactitude. The stylus, intricately linked to a linear variable differential transformer (LVDT), faithfully translates surface irregularities into vertical motion as it traverses the film. This motion is meticulously captured as electrical signals, reflecting the dynamic positioning of the LVDT core (Fig. 2.14). Subsequently, an AC reference signal, modulated by the LVDT displacement, undergoes meticulous conditioning and conversion into digital data via a high-fidelity integrating analog-to-digital converter[62].

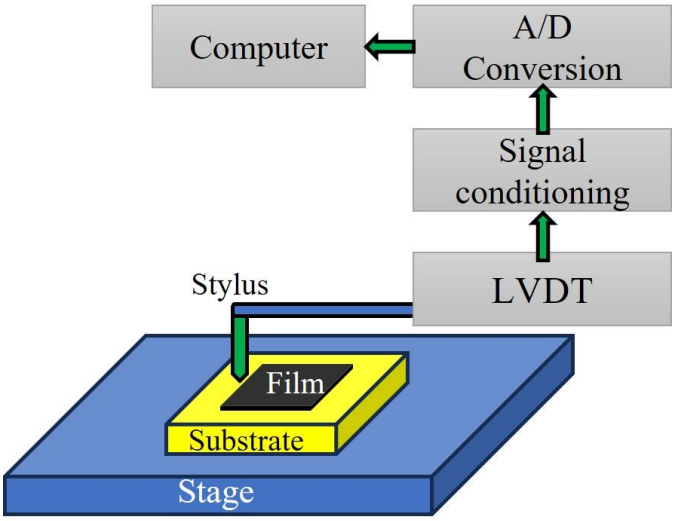

Figure 2.14 Block diagram of surface profilometer

In film thickness measurement, a targeted region of the sample is shielded during deposition to create a distinct contrast between the deposited film and the substrate. The scan area subjected to measurement encompasses the space delineated by the substrate and the deposited film, enabling precise determination of film thickness.

2.4.8 *X-ray diffraction*

X-ray diffraction (XRD) is a crucial method in material analysis, renowned for its ability to reveal the atomic and molecular arrangements within crystals. X-rays, a type of electromagnetic radiation, primarily undergo diffraction via Thomson scattering. When interacting with a material, X-rays undergo modifications due to their interactions with electrons within the material, while maintaining their kinetic energy or wavelength. In crystalline materials, incident X-rays are diffracted in specific directions determined by the crystal's lattice structure[63]. The density of electrons within the three-dimensional crystal lattice can be inferred from the angles and intensities of the diffracted beams. Further examination provides essential crystallographic details, including atomic positions, grain sizes, and strain. XRD follows the equation $q = K_{out} - K_{in} = G$, where K_{out} and K_{in} represent the wave vectors of the diffracted and incident X-rays, respectively, and G denotes a reciprocal lattice vector.

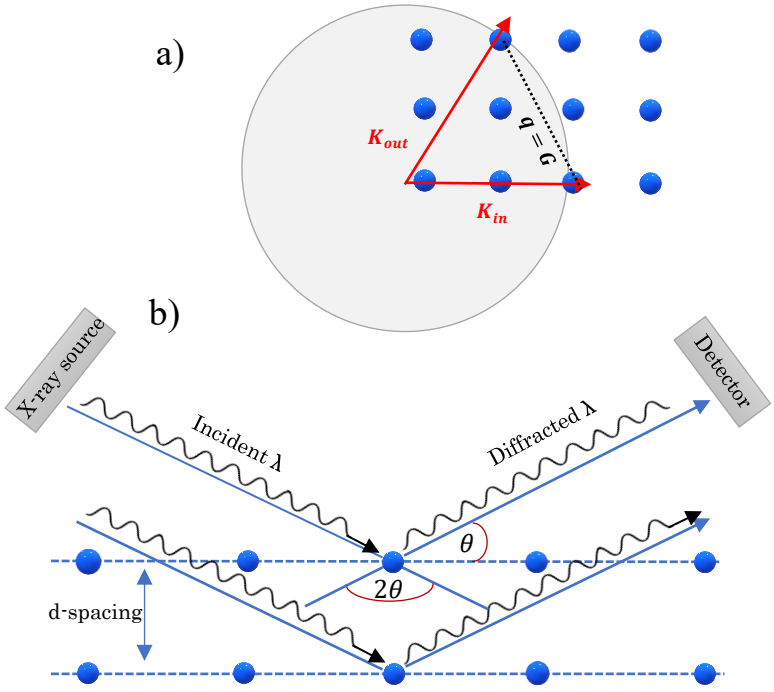

Figure 2.15 a). Schematic of Ewald Sphere. b). Illustration of Bragg's Law

This principle is visually depicted in Fig. 2.15a, where all possible G vectors are situated within a sphere known as the Ewald sphere of diameter $2|K| = 4\pi/\lambda$. By assuming $G = nG_{hkl}$, Bragg's Law can be derived as $n\lambda = 2d_{hkl}\sin\theta$, where the angle between K_{in} and K_{out}

is 2θ. The interpretation of Bragg's formula is illustrated in Fig. 2.15b, where incident X-rays are reflected by lattice planes (*hkl*), and diffraction occurs only when the path difference of waves reflected by adjacent planes equals an integer multiple (n) of the wavelength. A typical XRD setup comprises an X-ray tube, a sample holder, and an X-ray detector. X-rays are produced in the tube by heating a filament to emit electrons that strike a certain material (usually Cu, Fe, Mo, or Cr). Cu is the most commonly used target material, yielding X-rays with a characteristic wavelength of $\lambda(K_\alpha)$ = 1.5418 Å. In this study, phase identification of ZnO:Co and TmIG films was performed using the Bruker D8 Discover instrument, to reveal the crystal structure.

2.4.9 *Vibrating Sample Magnetometer*

Vibrating Sample Magnetometer (VSM) is a crucial instrument for evaluating the magnetic properties of materials, including saturation magnetization, coercivity, and remanence, by analyzing hysteresis loop magnetization on the applied field. The determination of magnetic moments through a VSM relies on Faraday's principle. By inducing electromagnetic currents within a series of coils through the deliberate movement of a magnetic sample nearby, this method provides precise data regarding the sample's magnetic moment[64]. In a VSM setup, the sample is suspended using a non-magnetic quartz rod between two electromagnets equipped with pick-up coils, as illustrated in Fig. 2.16.

The opposite end of the sample rod connects to a vibrating-translational head, enabling vertical sample oscillation and accurate positioning in the X, Y, and Z directions. The magnetic sample's oscillation within a magnetic field disturbs the flux lines generated by the pick-up coils, resulting in a noticeable change in electromotive force (EMF). Calibration of this EMF against a standard magnetic specimen allows for precise determination of the test sample's magnetization. This setup involves sweeping the magnetic field within the range of +10 kOe to -10 kOe, generating a characteristic hysteresis loop. Hysteresis measurements at room temperature were performed using a Lakeshore VSM, calibrated before each orientation measurement with a Ni reference to ensure highly accurate saturation magnetization values for the magnetic films. In this study, VSM was employed to

investigate the hysteresis loop of ZnO:Co films at room temperature.

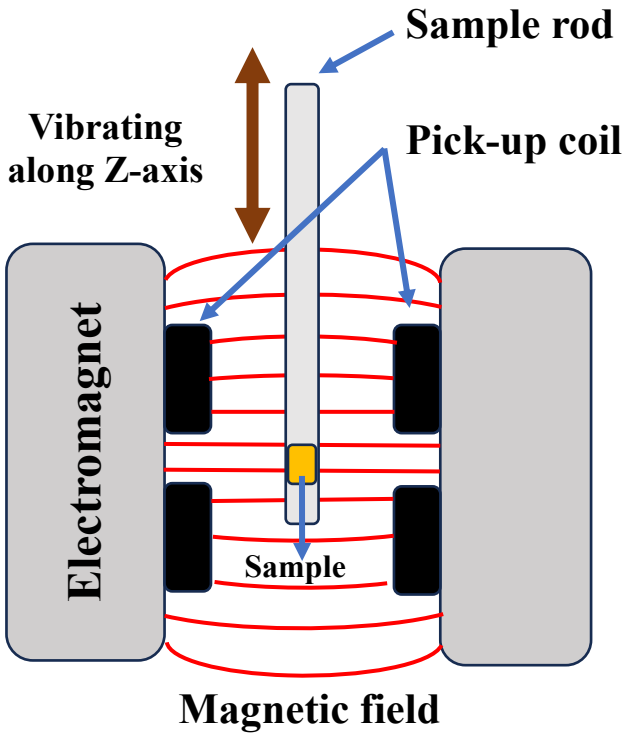

Figure 2.16 Illustration of VSM measurement.

2.4.10 *Superconducting Quantum Interference Device Magnetometry*

Superconducting quantum interference device (SQUID) exploits the Josephson effect to detect tiny fluctuations in magnetic flux. Typically configured as a ring of superconducting materials punctuated by one or more Josephson junctions, SQUID measurement offers unparalleled sensitivity to magnetic fields, making it an indispensable tool in magnetic material science[65]. This structure allows electron Cooper pairs to tunnel through, facilitated by a thin insulating layer between the superconducting sections. SQUID exists in two configurations: a) alternating current (AC) with a single Josephson junction and b) DC with two Josephson junctions. The DC SQUID is notably more sensitive than its AC counterpart, operating on the principle of quantum-mechanical interference of Cooper pair wavefunctions as they traverse the junctions modulated by a magnetic field within a loop. Maintaining a constant biasing current in the SQUID results in voltage fluctuations

synchronized with phase changes at the junctions, depending on the magnetic flux variations. This allows for measuring flux alterations through oscillation counting, with the SQUID capable of detecting tiny magnetic fields down to 10^{-14} T. Fig. 2.17 depicts a schematic of a Josephson junction utilized in SQUID magnetometry. Throughout this dissertation, magnetic measurements were conducted using a quantum design magnetic property measurement system (MPMS).

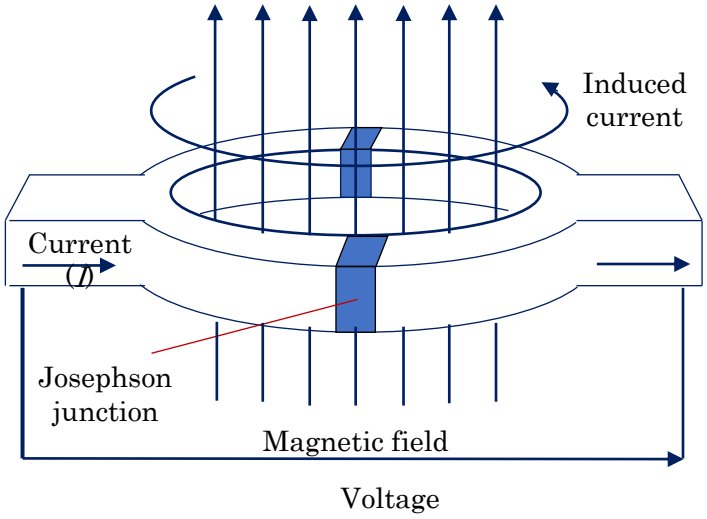

Figure 2.17 Illustration of Josephson junction.

The magnetic properties determined through SQUID magnetometry include the dependences of magnetization on the applied field (*M–H*) and temperature. *M–H* measurement involves sweeping a magnetic field from zero to positive saturation, reversing direction back to zero, and then proceeding to negative saturation before returning to zero. Parameters obtained from hysteresis measurement include coercivity (H_c), saturation magnetization (M_s), and saturating field (H_s). The magnetization depending on temperature follows two protocols: field-cooled (FC) and zero-field-cooled (ZFC). For FC, the sample is cooled from 300 to 5 K under an applied field and then reheated to 300 K under the same field, with the magnetization measured over time. This technique reveals the transitions in magnetic properties such as the Curie temperature (T_c). For ZFC, the sample is heated above the magnetic blocking temperature (T_b) and then, cooled to a low temperature (~5 K) without applying any field. Subsequently, a field is applied at 5 K, and the sample is heated to 300 K under this field while monitoring the magnetization. The bifurcation between the FC and ZFC curves at the blocking temperature indicates superparamagnetism. In this study, SQUID

was used to investigate the magnetic properties of ZnO:Co and TmIG films.

2.4.11 *Ferromagnetic resonance*

Ferromagnetic resonance (FMR) is a measurement technique that reveals the magnetization dynamics in magnetic films. This measurement facilitates the determination of magnetic damping, effective magnetization, and magnetic anisotropy. Magnetization dynamics is modeled using the Landau–Lifshitz–Gilbert (LLG) equation, as follows[66]:

$$\frac{\partial \boldsymbol{m}}{\partial t} = -|\gamma|\boldsymbol{m} \times \boldsymbol{H}_{eff} + \alpha \boldsymbol{m} \times \frac{\partial \boldsymbol{m}}{\partial t} \tag{2.10}$$

The symbols $\boldsymbol{m}, \alpha$, and $\boldsymbol{H}_{eff}$ are the normalized magnetization (M/M_s), gyromagnetic ratio, Gilbert damping parameter, and effective magnetic field, respectively. The observation of an FMR signal is a consequence of the effect of spin precession on the magnetization, as shown in Fig. 2.18, which is driven by an external AC magnetic field generated by microwave power.

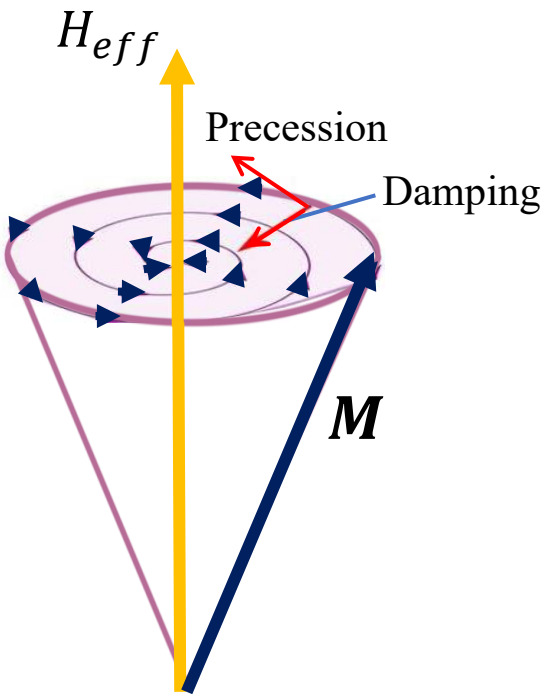

Figure 2.18 Illustration of the magnetization dynamics of the moment with an applied magnetic field.

The signal is proportional to the amount of microwave power absorbed by the film. At resonance, there is a sharp increase in absorption. The resonance frequency depends on various magnetic properties, including the gyromagnetic ratio, saturation magnetization, magnetic anisotropy, and applied external field.

During FMR measurement, the film is subjected to microwave radiation at a constant frequency while the external magnetic field is systematically adjusted. Upon meeting the resonance conditions, characterized by the alignment of the external field with the sample's magnetic properties, there is a discernible absorption of energy, which can be detected through FMR monitoring. Typically, FMR results are analyzed by examining the first derivative of the absorption spectrum. In this investigation, measurements were carried out using the Bruker EMX spectrometer.

2.4.12 *Kerr effect*

The Kerr effect stands as one among several magneto-optical phenomena. When incident plane-polarized light interacts with a magnetized surface, its polarization undergoes rotation, a phenomenon known as the Kerr effect[67]. This effect can be adequately described through a phenomenological model represented as follows:

$$\vec{\boldsymbol{D}} = \epsilon\left(\vec{\boldsymbol{E}} + iQ_k\vec{\boldsymbol{m}} \times \vec{\boldsymbol{E}}\right) \tag{2.11}$$

Where ϵ represents the dielectric constant, and Q_K denotes a material-specific parameter characterizing the intensity of the Kerr effect. The vector $\vec{\boldsymbol{D}}$ signifies the secondary light amplitude generated through the magneto-optical interaction between the illuminating plane light wave's electric vector $\vec{\boldsymbol{E}}$ and the sample's magnetization vector $\vec{\boldsymbol{m}}$. When the incident light interacts with the magnetic sample, electrons within the material undergo vibrational motion. This motion, governed by the Lorentz force ($\vec{\boldsymbol{m}} \times \vec{\boldsymbol{E}}$), results in a Lorentz movement, denoted by θ_L. Projection of this movement onto the plane perpendicular to the direction of reflected light propagation yields the magneto-optical or Kerr amplitude $\vec{\boldsymbol{K}}$. This Kerr amplitude, polarized perpendicularly to the standard reflected amplitude $\vec{\boldsymbol{N}}$, which is polarized within the incident light plane, contributes to the rotation of the polarization vector by $\Phi_K=|\vec{\boldsymbol{K}}|/|\vec{\boldsymbol{N}}|$. By utilizing an analyzer, this rotation enables domain contrast. Various Kerr

microscopy configurations exist, each sensitive to different magnetization orientations derived from understanding the Lorentz movement. To achieve a detectable Kerr rotation, an appropriate direction of incident light must be aligned with the direction of magnetization. When the polarizer is oriented either parallel or orthogonal to the incidence plane $\theta \neq 0$, the setup is termed the longitudinal Kerr effect (Fig. 2.19.).

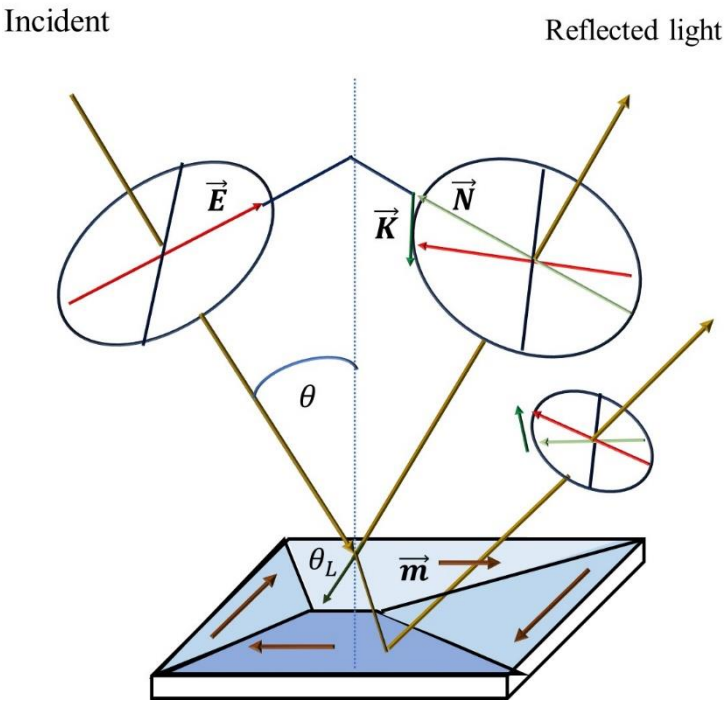

Figure 2.19 Schematic of the magneto-optical interaction for longitudinal Kerr effect

In such instances, the Kerr amplitude is proportional to the sine of the angle of incidence, $\sin(\theta)$. Consequently, when magnetization lies parallel to the surface, maximal Kerr amplitude occurs with the incident light plane parallel to the magnetization direction, disappearing for normal incidence. Thus, the oblique longitudinal Kerr effect is employed for domain imaging. Normal incidence ($\theta = 0$), known as the polar Kerr effect, is utilized for imaging domains magnetized perpendicular to the sample surface. In the transverse Kerr effect, where in-plane magnetization is normal to the incidence plane, incident light with $\vec{E}$ parallel to this plane generates a Kerr amplitude parallel to N, inducing amplitude variation but no rotation. However, when incident light polarization is at a 45° angle to the incidence

plane, modulation of the component of $\vec{\boldsymbol{E}}$ normal to the plane and subsequent rotation of polarization allows sensitivity to in-plane magnetization upon reflection. Through the process of superposition, this leads to the polarization rotation, enabling sensitivity to in-plane magnetization. In this study, the magnetic domain structure of the TmIG film was visualized using a Kerr microscope (Evico microscope).

References

1. J. T. Gudmundsson, *Plasma Sources Sci. Technol.* **29** (2020), doi:10.1088/1361-6595/abb7bd.
2. K. Wasa, S. Hayakawa, *Rev. Sci. Instrum.* **40**, 693–697 (1969).
3. W. D. Gill, E. Kay, *Rev. Sci. Instrum.* **36**, 277–282 (1965).
4. X. J. Liu, C. Song, F. Zeng, F. Pan, B. He, W. S. Yan, *J. Appl. Phys.* **103** (2008), doi:10.1063/1.2919065.
5. Z. Ye, H. Ling, Y. Ling, Q. Fu, *ACS Appl. Electron. Mater.* (2024), doi:10.1021/acsaelm.4c00031.
6. V. D. Duong, P. Cao Van, T. Nguyen Thi, H. Y. Ahn, V. A. Cao, J. Nah, G. Kim, K. S. Lee, J. W. Kim, J. R. Jeong, *J. Alloys Compd.* **927**, 166800 (2022).
7. G. Vilela, H. Chi, G. Stephen, C. Settens, P. Zhou, Y. Ou, D. Suri, D. Heiman, J. S. Moodera, *J. Appl. Phys.* **127** (2020), doi:10.1063/1.5135012.
8. C. H. Choi, S. H. Kim, *Thin Solid Films*. **515**, 2864–2871 (2007).
9. R. Siddheswaran, R. Medlín, C. E. Jeyanthi, S. G. Raj, R. V. Mangalaraja, *Appl. Phys. A Mater. Sci. Process.* **125**, 1–9 (2019).
10. G. Li, H. Bai, J. Su, Z. Z. Zhu, Y. Zhang, J. W. Cai, *APL Mater.* **7** (2019), doi:10.1063/1.5090292.
11. Y. Meng, P. Chen, W. He, H. Zhuang, J. Li, J. Dong, X. Li, L. Wang, Q. Guo, J. Yang, Y. Ji, X. Shen, X. Yu, G. Yu, J. Li, X. Han, R. Yu, *Small*. **2308724**, 1–8 (2024).
12. J. Ding, C. Liu, Y. Zhang, U. Erugu, Z. Quan, R. Yu, E. McCollum, S. Mo, S. Yang, H. Ding, X. Xu, J. Tang, X. Yang, M. Wu, *Phys. Rev. Appl.* **14**, 1 (2020).
13. S. Chen, Y. Xie, Y. Yang, D. Gao, D. Liu, L. Qin, W. Yan, B. Tan, Q. Chen, T. Gong, E. Li, L. Bi, T. Liu, L. Deng, *Chinese Phys. B.* **31** (2022), doi:10.1088/1674-1056/ac4cc4.
14. C. N. Wu, C. C. Tseng, K. Y. Lin, C. K. Cheng, S. L. Yeh, Y. T. Fanchiang, M. Hong, J. Kwo, *AIP Adv.* **8**, 6–12 (2018).
15. C. N. Wu, C. C. Tseng, Y. T. Fanchiang, C. K. Cheng, K. Y. Lin, S. L. Yeh, S. R. Yang, C. T. Wu, T. Liu, M. Wu, M. Hong, J. Kwo, *Sci. Rep.* **8** (2018), doi:10.1038/s41598-018-29493-5.
16. T. Dietl, H. Ohno, F. Matsukura, J. Cibert, D. Ferrand, *Science (80-.).* **287**, 1019–

1022 (2000).

17. M. Shatnawi, A. M. Alsmadi, I. Bsoul, B. Salameh, G. A. Alna'Washi, F. Al-Dweri, F. El Akkad, *J. Alloys Compd.* **655**, 244–252 (2016).
18. M. Ivill, S. J. Pearton, S. Rawal, L. Leu, P. Sadik, R. Das, A. F. Hebard, M. Chisholm, J. D. Budai, D. P. Norton, *New J. Phys.* **10** (2008), doi:10.1088/1367-2630/10/6/065002.
19. T. J. Castro, P. A. M. Rodrigues, A. C. Oliveira, F. Nakagomi, J. Mantilla, J. A. H. Coaquira, A. Franco, H. V. S. Pessoni, P. C. Morais, S. W. Da Silva, *J. Appl. Phys.* **121** (2017), doi:10.1063/1.4973526.
20. B. Huang, D. Zhu, X. Ma, *Appl. Surf. Sci.* **253**, 6892–6895 (2007).
21. H. S. Hsu, J. C. A. Huang, Y. H. Huang, Y. F. Liao, M. Z. Lin, C. H. Lee, J. F. Lee, S. F. Chen, L. Y. Lai, C. P. Liu, *Appl. Phys. Lett.* **88** (2006), doi:10.1063/1.2212277.
22. A. Simimol, A. A. Anappara, S. Greulich-Weber, P. Chowdhury, H. C. Barshilia, *J. Appl. Phys.* **117** (2015), doi:10.1063/1.4922050.
23. M. P. F. de Godoy, X. Gratens, V. A. Chitta, A. Mesquita, M. M. de Lima, A. Cantarero, G. Rahman, J. M. Morbec, H. B. de Carvalho, *J. Alloys Compd.* **859**, 157772 (2021).
24. L. R. Shah, H. Zhu, W. G. Wang, B. Ali, T. Zhu, X. Fan, Y. Q. Song, Q. Y. Wen, H. W. Zhang, S. I. Shah, J. Q. Xiao, *J. Phys. D. Appl. Phys.* **43** (2010), doi:10.1088/0022-3727/43/3/035002.
25. A. Chakraborty, R. Bouzerar, S. Kettemann, G. Bouzerar, *Phys. Rev. B - Condens. Matter Mater. Phys.* **85**, 1–7 (2012).
26. K. Kuwahara, N. Itagaki, K. Nakahara, D. Yamashita, G. Uchida, K. Kamataki, K. Koga, M. Shiratani, *Thin Solid Films*. **520**, 4674–4677 (2012).
27. N. Itagaki, K. Kuwahara, K. Matsushima, D. Yamashita, H. Seo, K. Koga, M. Shiratani, *Opt. Eng.* **53**, 087109 (2014).
28. I. Suhariadi, N. Itagaki, M. Shiratani, *ACS Appl. Nano Mater.* **3**, 2480–2490 (2020).
29. N. A. Spaldin, *Magnetic Materials ; Fundamentals and Application* (Cambridge University Press, Second., 2011).
30. T. Sharma, R. Jain, N. Ahmad, M. Ahmed, S. Oh, S. I. Siddiqui, *J. Mater. Res. Technol.* **26**, 7483–7489 (2023).

31. D. Chakraborti, thesis, North Carolina State (2007).
32. J. M. D. Coey, M. Venkatesan, C. B. Fitzgerald, *Nat. Mater.* **4**, 173–179 (2005).
33. S. F. Maehrlein, I. Radu, P. Maldonado, A. Paarmann, M. Gensch, A. M. Kalashnikova, R. V. Pisarev, M. Wolf, P. M. Oppeneer, J. Barker, T. Kampfrath, *Sci. Adv.* **4** (2018), doi:10.1126/sciadv.aar5164.
34. J. Walowski, M. Münzenberg, *J. Appl. Phys.* **120** (2016), doi:10.1063/1.4958846.
35. S. C. Abrahams, S. Geller, *Acta Crystallogr.* **11**, 437–441 (1958).
36. M. Redies, G. Michalicek, J. Bouaziz, C. Terboven, M. S. Müller, S. Blügel, D. Wortmann, *Front. Mater.* **9**, 1–11 (2022).
37. K. Momma, F. Izumi, *J. Appl. Crystallogr.* **44**, 1272–1276 (2011).
38. A. Biswas, Y. H. Joong, in *Epitaxy*, M. Zhong, Ed. (IntechOpen, 2018), p. 10.
39. A. Hirohata, K. Yamada, Y. Nakatani, L. Prejbeanu, B. Diény, P. Pirro, B. Hillebrands, *J. Magn. Magn. Mater.* **509** (2020), doi:10.1016/j.jmmm.2020.166711.
40. A. Hirohata, K. Takanashi, *J. Phys. D. Appl. Phys.* **47** (2014), doi:10.1088/0022-3727/47/19/193001.
41. S. Mokarian Zanjani, M. C. Onbaşlı, *J. Magn. Magn. Mater.* **499**, 166108 (2020).
42. E. Popova, N. Keller, F. Gendron, L. Thomas, M.-C. Brianso, M. Guyot, M. Tessier, S. S. P. Parkin, *J. Vac. Sci. Technol. A.* **19** (2001), doi:https://doi.org/10.1116/1.1392395.
43. J. Fu, M. Hua, X. Wen, M. Xue, S. Ding, M. Wang, P. Yu, S. Liu, J. Han, C. Wang, H. Du, Y. Yang, J. Yang, *Appl. Phys. Lett.* **110**, 3–8 (2017).
44. M. Kubota, A. Tsukazaki, F. Kagawa, K. Shibuya, Y. Tokunaga, M. Kawasaki, Y. Tokura, *Appl. Phys. Express*. **5** (2012), doi:10.1143/APEX.5.103002.
45. M. Kubota, K. Shibuya, Y. Tokunaga, F. Kagawa, A. Tsukazaki, Y. Tokura, M. Kawasaki, *J. Magn. Magn. Mater.* **339**, 63–70 (2013).
46. V. H. Ortiz, M. Aldosary, J. Li, Y. Xu, M. I. Lohmann, P. Sellappan, Y. Kodera, J. E. Garay, J. Shi, *APL Mater.* **6** (2018), doi:10.1063/1.5078645.
47. S. Damerio, C. O. Avci, *J. Appl. Phys.* **133** (2023), doi:10.1063/5.0139602.
48. E. R. Rosenberg, L. Beran, C. O. Avci, C. Zeledon, B. Song, C. Gonzalez-Fuentes, J. Mendil, P. Gambardella, M. Veis, C. Garcia, G. S. D. Beach, C. A. Ross, *Phys. Rev. Mater.* **2** (2018), doi:10.1103/PhysRevMaterials.2.094405.

49. C. R. Warren, V. Ortiz, L. Scipioni, J. Greer, J. Shi, Y. Kodera, J. E. Garay, *J. Magn. Magn. Mater.* **560** (2022), doi:10.1016/j.jmmm.2022.169513.
50. J. J. Bauer, E. R. Rosenberg, S. Kundu, K. A. Mkhoyan, P. Quarterman, A. J. Grutter, B. J. Kirby, J. A. Borchers, C. A. Ross, *Adv. Electron. Mater.* **6** (2020), doi:10.1002/aelm.201900820.
51. Y. Lin, L. Jin, H. Zhang, Z. Zhong, Q. Yang, Y. Rao, M. Li, *J. Magn. Magn. Mater.* **496**, 165886 (2020).
52. S. Das, R. Mansell, L. Flajšman, L. Yao, S. van Dijken, *J. Appl. Phys.* **134** (2023), doi:10.1063/5.0184675.
53. M. Kuila, A. Sagdeo, L. A. Longchar, R. J. Choudhary, S. Srinath, V. Raghavendra Reddy, *J. Appl. Phys.* **131** (2022), doi:10.1063/5.0085572.
54. Y. Zhang, Q. Du, C. Wang, W. Yan, L. Deng, J. Hu, C. A. Ross, L. Bi, *APL Mater.* **7** (2019), doi:10.1063/1.5112827.
55. P. J. Potts, P. C. Webb, *J. Geochemical Explor.* **37**, 1–2 (1992).
56. G. Greczynski, L. Hultman, *J. Appl. Phys.* **132** (2022), doi:10.1063/5.0086359.
57. Z. Silvestri, S. Azouigui, S. Bouhtiyya, S. Macé, M. D. Plimmer, P. Pinot, F. Tayeb-Chandoul, R. Hannachi, *Rev. Sci. Instrum.* **85** (2014), doi:10.1063/1.4870921.
58. T. Oikawa, *Japanese J. Tribol.* **51**, 33–38 (2006).
59. D. J. Smith, in *Microscopy for Nanotechnology* (Kluwer Academic, 2005), pp. 427–450.
60. A. Thust, *Phys. Rev. Lett.* **102**, 5–8 (2009).
61. E. Meyer, *Prog. Surf. Sci.* **41**, 3–49 (1992).
62. *Dektak 150 Surface Profiler User's Manual* (Veeco Instruments Inc., Revision., 2007).
63. G. F. Harrington, J. Santiso, *J. Electroceramics*. **47**, 141–163 (2021).
64. S. Foner, *Rev. Sci. Instrum.* **30**, 548–557 (1959).
65. R. L. Fagaly, *Rev. Sci. Instrum.* **77** (2006), doi:10.1063/1.2354545.
66. Y. Wang, R. Ramaswamy, H. Yang, *J. Phys. D. Appl. Phys.* **51** (2018), doi:10.1088/1361-6463/aac7b5.
67. S. . Bader, *J. Magn. Magn. Mater.* **100**, 440–454 (1991).

Chapter 3

Structure and Magnetic Properties of ZnO:Co films Fabricated by RF magnetron Sputtering Using Nitrogen

3.1 Introduction

Incorporating a small fraction of magnetic ions or atoms into the crystal lattice of a semiconductor creates a new class of materials known as diluted magnetic semiconductors (DMS)[1]. These materials are highly valuable for spintronic devices, as their magnetic properties such as the Curie temperature and coercivity, can be controlled electrically[2]. Among the atomic classifications of semiconductors and transition metals, zinc oxide (ZnO) and Co attract considerable attention for DMS materials. As a semiconductor, ZnO has many advantages such as a wide band gap, large exciton binding energy, electron mobility, high thermal conductivity, and high solubility for transition-metal ions[3,4]. Co has a large magnetic moment and ionic radius close to that of zinc[5]. Therefore, its high solubility in ZnO provides a high critical temperature. The predicted room-temperature ferromagnetic properties also make Co-doped ZnO (ZnO:Co) a promising candidate as a DMS material[6]. Controlling the magnetic properties at room temperature without secondary phases or separation of Co is the main challenge associated with ZnO:Co. Several reports have proposed solutions for this issue, including tuning the concentrations of Co[7–9], oxygen vacancies[10–12], and zinc interstitial defects[13,14]. However, the tuning of the material composition produces controversial results. Therefore, an alternative method is required to obtain the ferromagnetic state of ZnO:Co more clearly in both the result and explanation. Nanoscale inhomogeneities, which can significantly increase the critical temperature, have been reported[15]. The technical difficulty of creating and controlling inhomogeneous atomic distributions is a challenge to realizing nanoscale inhomogeneity in these materials. On the other hand, the control of the film structure of ZnO, from amorphous to crystalline state, has been reported[16–18]. In this technique, nitrogen gas is introduced into the chamber during deposition. The nitrogen atoms adsorbed during deposition disrupt the crystallization of ZnO. Subsequently, post-annealing vaporizes the nitrogen, improving the crystalline quality of ZnO. This technique has the potential to obtain inhomogeneities represented by defects and amorphous ZnO:Co films.

In this study, Co-doped ZnO films were investigated, which were grown by RF magnetron sputtering using nitrogen (ZnO:CoN) and subsequently subjected to post-annealing. This technique was explored as a potential solution to overcome the difficulties in controlling inhomogeneities and improve the magnetic properties of DMS materials. Additionally, ZnO:Co films without nitrogen and using oxygen were fabricated for

comparison.

3.2 Methods

Radio-frequency (RF) magnetron sputtering (ULVAC, MPS) using three cathodes—two for the ZnO target at 100 W and one for Co at 50 W—was employed to grow ZnO:Co, ZnO:CoN (using nitrogen), and ZnO:CoO (using oxygen) films on an SiO_2 substrate, as shown in Fig. 3.1. The SiO_2 substrate, which had been ultrasonically cleaned with acetone and methanol for 5 min followed by immersion in deionized water, was placed in a substrate holder 70 mm away from the target.

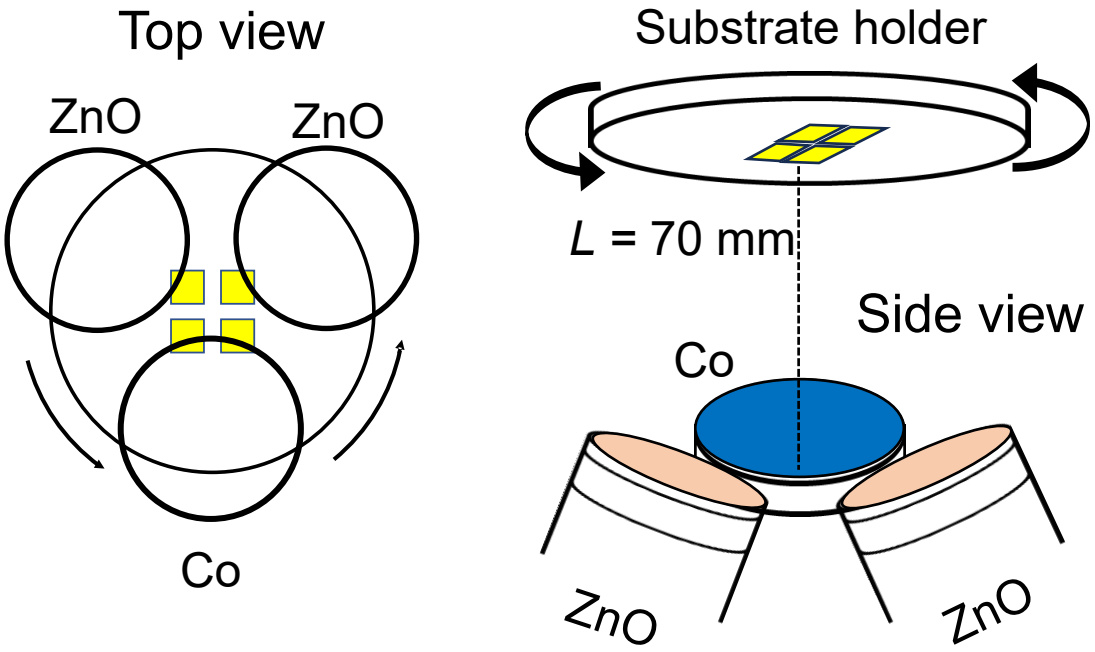

Figure 3.1 Geometric position of target and substrate holder in sputtering chamber.

During the experiments, the base pressure, substrate holder rotation speed, and argon, nitrogen, and oxygen gas flow rates were 6.8×10^{-5} Pa, 10 rpm, 6.2 sccm, 24.2 sccm, and 1.8 sccm, respectively. To adjust the inhomogeneity of the films, the composition and microstructure were controlled by varying the postannealing temperature (T_{an}) in the air for each sample of each film. This process was applied to ZnO:Co (400 and 800 °C), ZnO:CoN (400, 600, 800, and 1000 °C), and ZnO:CoO (400 °C). XRD measurements were conducted to investigate the crystal structure and grain size. The magnetic properties were determined

using vibrating sample magnetometry (VSM) and SQUID MPMS3. Additionally, the elements such as nitrogen, oxygen, cobalt, and zinc in the films were analyzed using XRF, XPS, and TDS, at a heating rate of 60 °C/min from 50 to 1000 °C.

3.3 Results

3.3.1 *Effect of Post-annealing on The Structure and Magnetic Properties of ZnO:Co*

The stability of the plasma during the deposition process was demonstrated by the stability of the total pressure and RF reflection coefficient, which were 0.35 Pa and 0, respectively. The total thickness measured by the Dektak profilometer was ~380 nm. The chemical composition of the ZnO:Co film, according to the post-annealing conditions is presented in Fig. 3.2.

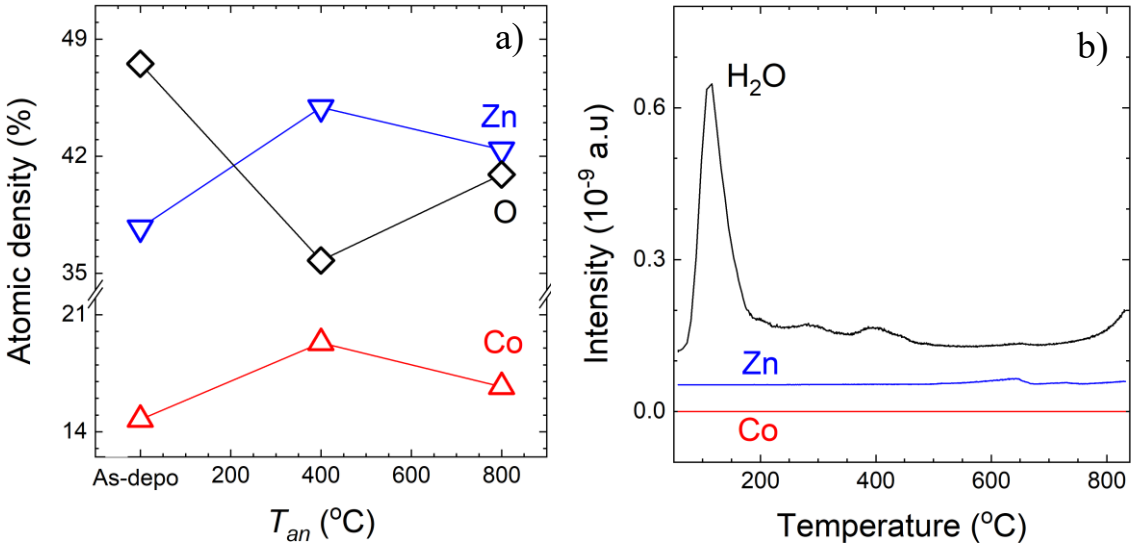

Figure 3.2 Chemical concentration of ZnO:Co film. a). XRF and b). TDS.

The composition investigated by the FP method available in the XRF tools revealed that the T_{an} of 800 °C resulted in the ratio between zinc (Zn) and oxygen (O) being close to 1, indicating an approach to the ZnO bulk. The Co and Zn content were highest and the O concentration was the lowest at 400 °C. On the contrary, the as-deposited condition resulted in the lowest concentration of Zn and Co, and highest of O. The change in film concentration could be attributed to the absorption and desorption of O during annealing in air[19,20]. TDS measurement was performed to confirm the adsorption-desorption of each element of the ZnO:Co film, as shown in fig. 3.2b. The results indicate that the ZnO:Co film is

contaminated with hydrogen. This finding can be attributed to the exposure of the oxide film to ambient water vapor, which effectively cures any oxygen vacancies that may occur[21]. While the concentration of Co and Zn remains relatively constant in response to the post-annealing effect.

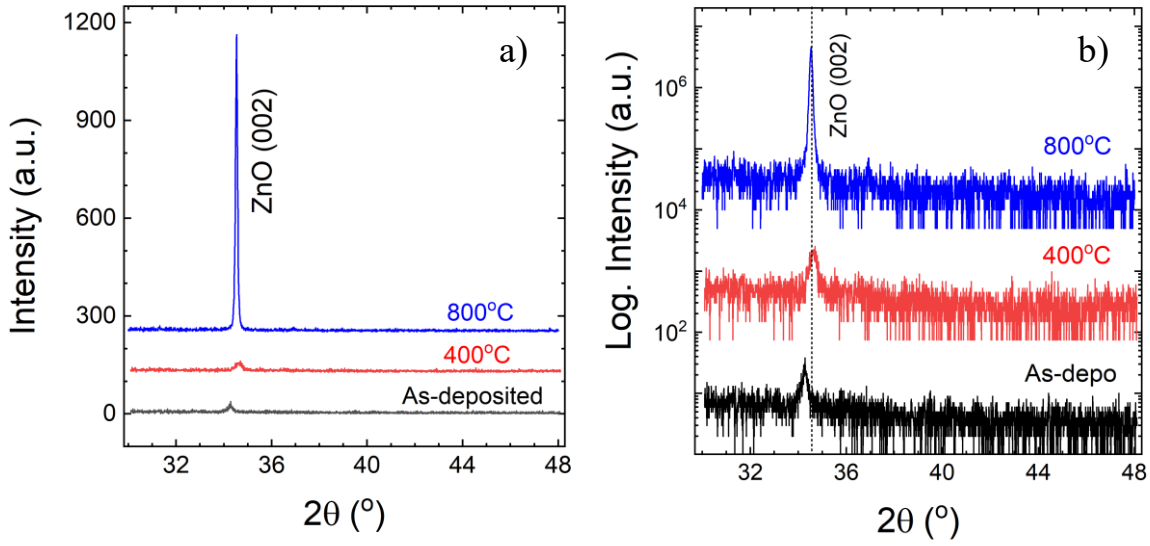

Figure 3.3 XRD curve of the ZnO:Co film. a). Normal intensity and b). Log. intensity.

XRD measurements were conducted to reveal the crystal structure of the ZnO:Co films, as a function of the post-annealing temperature (T_{an}), as depicted in Fig. 3.3. The result exhibits diffraction peaks at 34.3, 34.6, and 34.5° for as-deposited and T_{an} at 400 and 800 °C, respectively. The presence of a diffraction peak around 34° indicates that all films have a wurtzite (002) structure. This suggests that Co has been successfully incorporated into the ZnO structure[22,23].

The post-annealing treatment slightly shifted the peak to a higher degree. The observed peak shift could be attributed to several factors such as the smaller Co ionic radius (compared to that of Zn) and the presence of oxygen vacancies formed after post-annealing treatment [24–26]. Compared to the films annealed at 400 °C and as-deposited conditions, films annealed at 800 °C significantly improved crystal quality. The alteration in grain size and porosity of the film during post-annealing plays a significant role in the formation of long-range crystal order[26–28]. In addition, the change in the Zn/O ratio, which is close to 1 at the highest annealing temperature, is also believed to improve the crystal quality of the film.

The effect of post-annealing on the surface morphology profiles of the as-deposited

films and films with T_{an} of 400 and 800 °C were evaluated via atomic force microscopy (AFM) with a scan size of 5 × 5 μm^2 and 2 × 2 μm^2, as shown in Fig. 3.4. An increase in grain size was observed in the surface morphology. In the as-deposited condition, the grain boundaries were clearly observed on the surface with a grain size of 75.9 nm and root mean square (RMS) roughness of 1.3 nm. With increasing T_{an}, the grain boundaries coalesced to form islands, increasing the grain size to 145.6 and 288.7 nm and roughness to 3.2 and 8.2 nm.

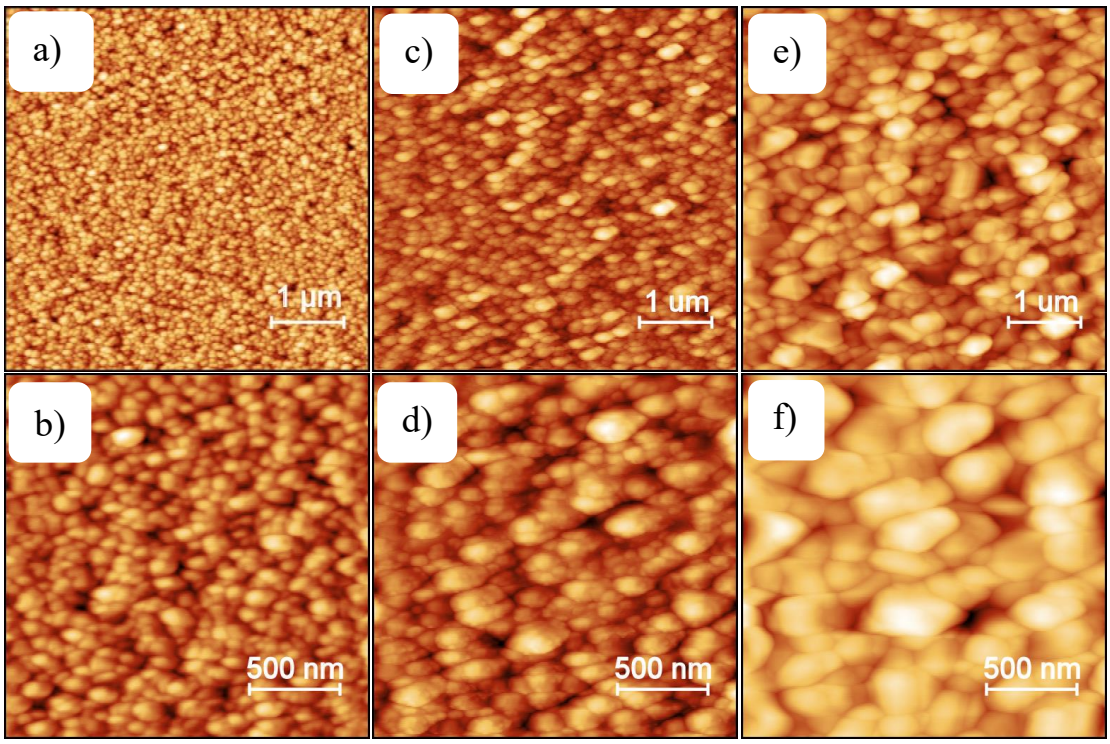

Figure 3.4 Surface profile of ZnO:Co films for different postannealing temperature. (a–b). as-deposited, (c–d). T_{an} of 400 °C, and (e–f). 800 °C.

The magnetization dependence of the applied field was measured using VSM at room temperature (300 K) of ZnO:Co films is presented in Fig. 3.5a. A clear hysteresis loop is observed for the film annealed at 400 °C, indicating that ferromagnetic properties are obtained for this condition. The as-deposited film and film annealed at 800 °C tend to exhibit paramagnetic properties. To study the magnetic properties at a T_{an} of 400 °C more thoroughly, the dependence of magnetization on a field (*M–H*) at low temperature (4 K) and the dependence of magnetization on temperature (*M–T*) were investigated. The clear hysteresis loop and coercivity of 131.1 mT, as shown in Fig. 3.5b, indicates that the film has

ferromagnetic properties.

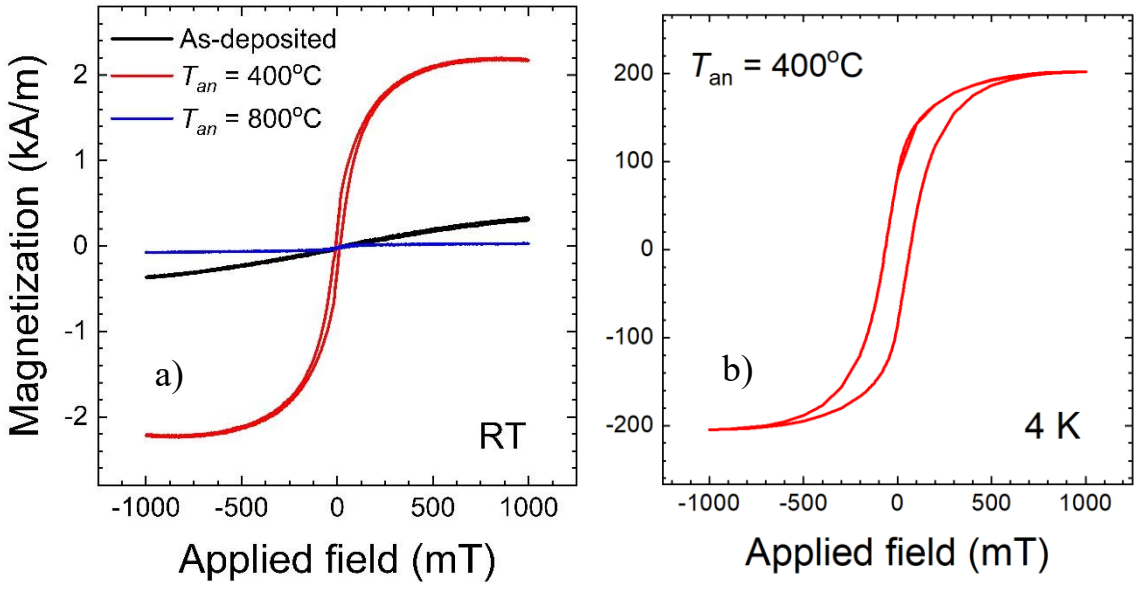

Figure 3.5 Dependence of the magnetization on the applied field of the ZnO:Co film. a). As-deposited, T_{an} 400 and 800 °C at RT and b). T_{an} 400 °C at 4 K.

The protocol of the temperature-dependent magnetization measurement is as follows: First, the film was cooled in the absence of an applied field to 4 K, and then the magnetization was measured when heated to 300 K in a field of 10 mT, known as ZFC protocol. Second, the sample was re-cooled to 4 K and measured in a field of 10 mT, called FC protocol. The FC curve demonstrated a gradual increase in magnetization with decreasing temperature, while the ZFC exhibited a certain peak. The emerging peak of 27 °C on the ZFC curve was the critical temperature that represents the transition between blocked and superparamagnetic moments, known as the blocking temperature (T_b). The clear split and peak curve observed in the ZFC–FC curves, as shown in Fig. 3.6, indicated that the film exhibited superparamagnetic properties[29,30].

Figure 3.7 presents the ZFC–FC curves of ZnO:Co films with a T_{an} of 400°C for various applied fields. It can be observed that an increase in the applied field reduces T_b and collapses the bifurcation between the ZFC and FC curves. This behavior indicates that the Co element in ZnO:Co is nanoscale, resulting in a reduced energy barrier when exposed to an applied field. Consequently, thermal fluctuations can reorient the superparamagnetic moments at lower temperatures[31–33]. In addition, the magnetization observed in the FC curve

at 300 K is non-zero, indicating that the Curie temperature of this film exceed room temperature[34].

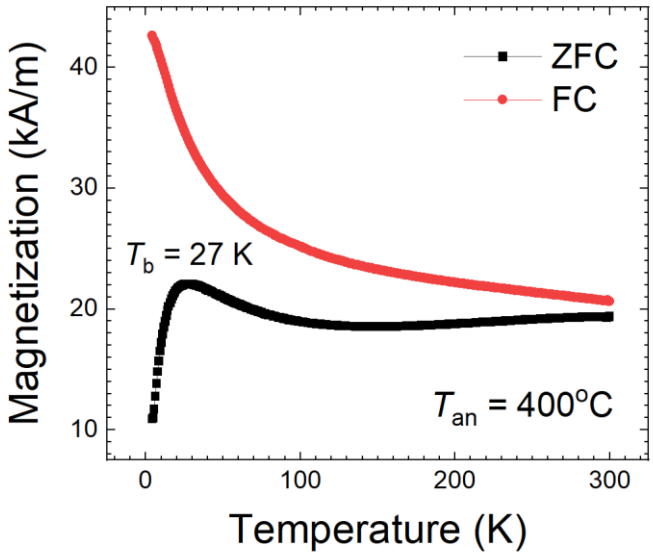

Figure 3.6 ZFC–FC curve of ZnO:Co film for T_{an} of 400 °C.

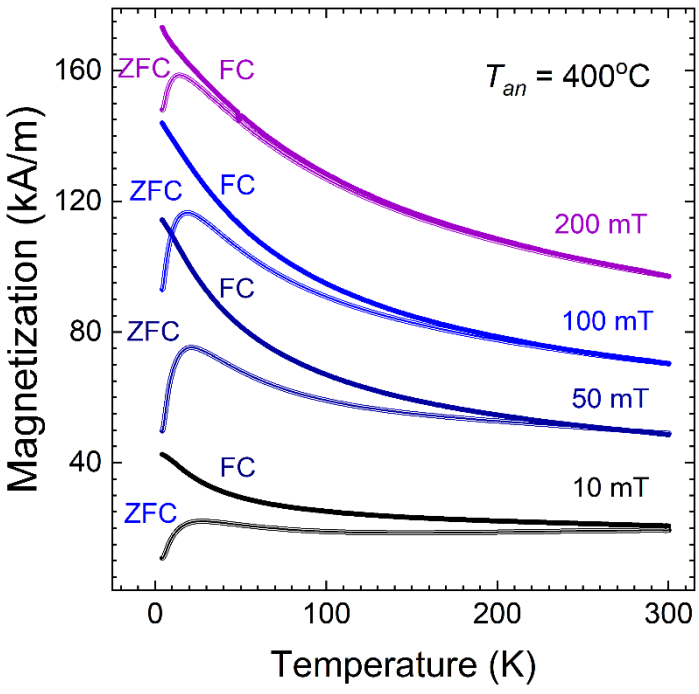

Figure 3.7 ZFC–FC curve under various applied fields for ZnO:Co film with T_{an} of 400 °C

The appearance of superparamagnetic–ferromagnetic properties in the ZnO:Co film at T_{an} of 400 °C is attributed to the high Co content[8,35,36] and O vacancies (O_v)[11,19]. The Co content of 30%, which exceeds the solubility limit with ZnO (25%), has the potential to form Co clusters on the film. The appearance of Co clusters in the film will enhance the magnetization significantly, as reported by other groups[37–39]. O_v contribute to the enhancement of magnetic interactions through the BMP mechanism[10,20,40]. In the BMP mechanism, dopants introduced into the ZnO lattice interact through a donor impurity band created by lattice defects such as oxygen vacancies. The spin in the Co ions is antiparallel to the spin of donor electrons inhabiting hydrogenic orbits, owing to the spin coupling between them. This coupling can align all spins within this extended orbit. As a result of the overlap of various orbits, an impurity band is formed, which aligns the spins in parallel directions and strengthens the ferromagnetic ordering of the films[35,41,42].

XPS measurements were carried out for the ZnO:Co film with a T_{an} of 400 °C to confirm the presence of Co clusters, which may be the origin of ferromagnetic properties in this film. The binding-energy spectra were corrected using the C 1s standard at 284.6 eV. The XPS pattern of Co in Fig. 3.8a shows that the difference in binding energy between the $2p_{1/2}$ and $2p_{3/2}$ peaks is 15.1 eV, indicating the appearance of Co clusters[5,34]. The concentration of Co, as measured by XRF, is high and exceeds the solubility limit in ZnO (25%), resulting in the formation of Co clusters[23,43–45]. Fig. 3.8b shows the O 1s curve deconvoluted in two peaks. The lower energy peak at 529.6 eV corresponds to O^{2-}[5,25], While the higher bond energy peak at 531.4 eV can be attributed to either oxygen vacancies[25] or oxygen bonding with hydrogen[46]. However, XPS signals originating from missing oxygen atoms are improbable. Therefore, an O-H signal indicating the presence of hydroxyl water in the film is more appropriate[21]. This presence of O-H is confirmed by the TDS data in Fig. 3.2b, which shows a peak of H_2O molecules appearing when annealed at temperatures above 100°C, indicating the presence and subsequent desorption of these molecules. The O-H signal is due to the adsorption of hydroxyl water on the oxide film under ambient conditions. Clear $2p_{3/2}$ and $2p_{1/2}$ peaks are observed in the XPS spectra of Zn, as shown in Fig. 3.8c. The binding-energy difference between each peak is 23.1 eV, indicating the bivalent state of Zn[47–49]. While both Zn $2p_{3/2}$ and Zn $2p_{1/2}$ for the ZnO:Co film consists of two peaks, the lower energy peak is attributed to Zn–O[50,51] and higher energy peak is attributed to Zn–Co[50,51] or

O-H[52].

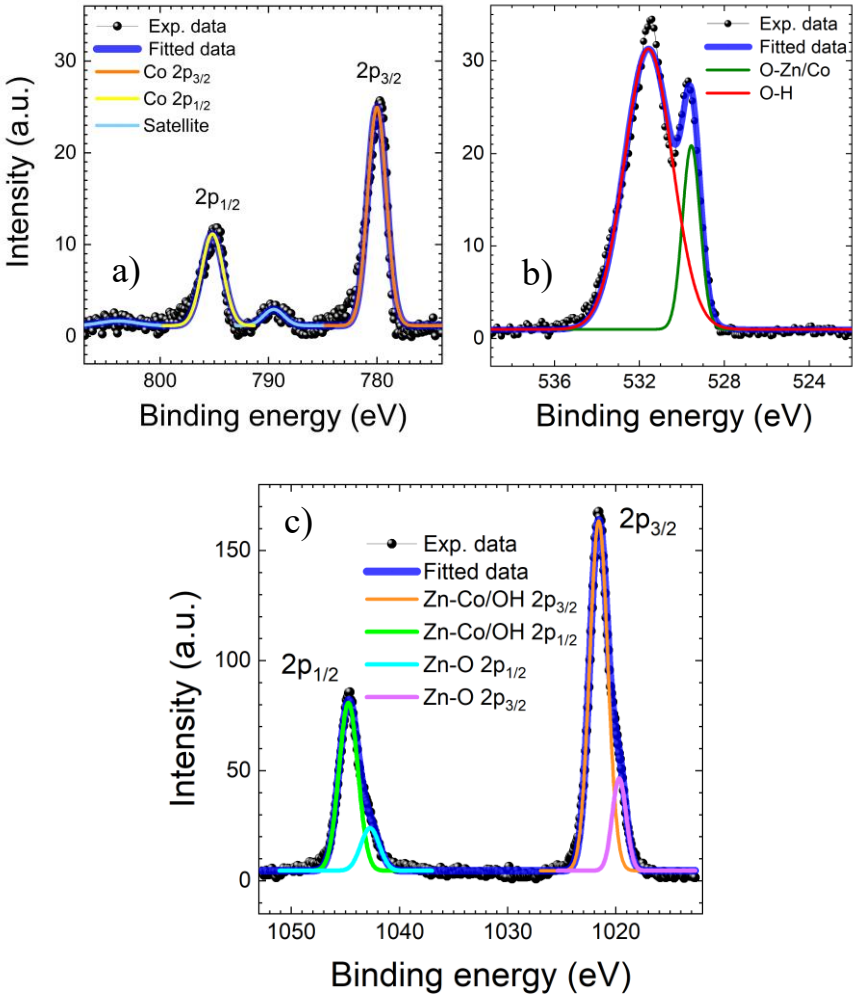

Figure 3.8 XPS spectra of ZnO:Co film for T_{an} of 400 °C. a). Co 2p, b). O 1s, c). Zn 2p

3.3.2 *Effect of Nitrogen on the Structure and Magnetic Properties of ZnO:Co*

The composition of the film was investigated by XRF measurements using the FP method, as shown in Fig. 3.9a. The concentrations of Zn and Co are relatively constant at ~50 and 7%. Postannealing at temperatures above 400 °C induces significant changes in the composition of O and N, where the amount of O increases from 35.6 to 40.7% and that of N decreases from 7.7 to 2.4%. These results indicate that increasing the postannealing temperature above 400 °C induces N desorption and the vacancies get filled by O. TDS measurement was performed to confirm the N desorption of the film. As demonstrated in Fig. 3.9b, N begins to desorb at T_{an} above 400 °C and reaches its peak around 600 °C, which is consistent with the XRF results. The reduction in N concentration toward the postannealing treatment is also in line with the results of a previous report[18]. In comparison with the ZnO:Co film without nitrogen, the addition of N_2 gas during deposition influences reduces the Co concentration from 19.3 to 7.5% and thickness of the film from 380 to 340 nm. It can be explained that the presence of N_2 in the sputtering chamber during deposition reacts with the Co target to form cobalt nitride (CoN)[53–56]. This affects the entire sputtering process, reducing the sputtering yield[57,58].

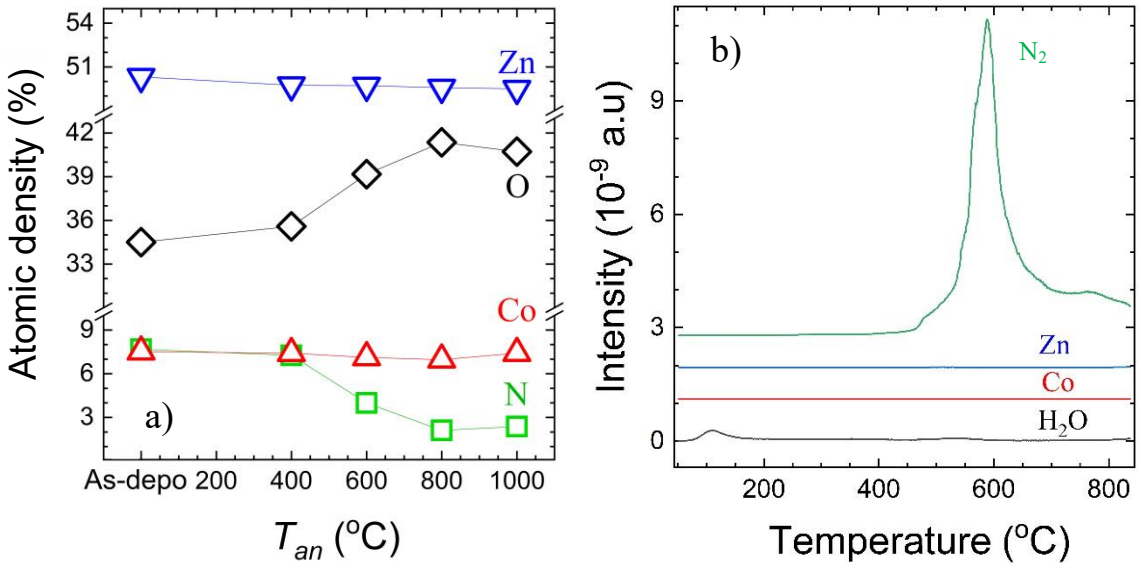

Figure 3.9 Composition of the ZnO:CoN films a). XRF and b). TDS.

Fig. 3.10a displays the XRD pattern for ZnO:CoN in the 30–77° range at various T_{an}. Diffraction peaks around 34°, which are assigned to the ZnO (002) plane, are observed in all

films. To distinguish each film more clearly, the XRD patterns are presented for the short ranges of 30–37° and 67–76° in Fig. 3.10b and 3.10c. No secondary phases were detected under any conditions, while a slight shift in peak position about 0.5° were observed for the film subjected to post-annealing at 600°C, 800°C, and 1000°C.

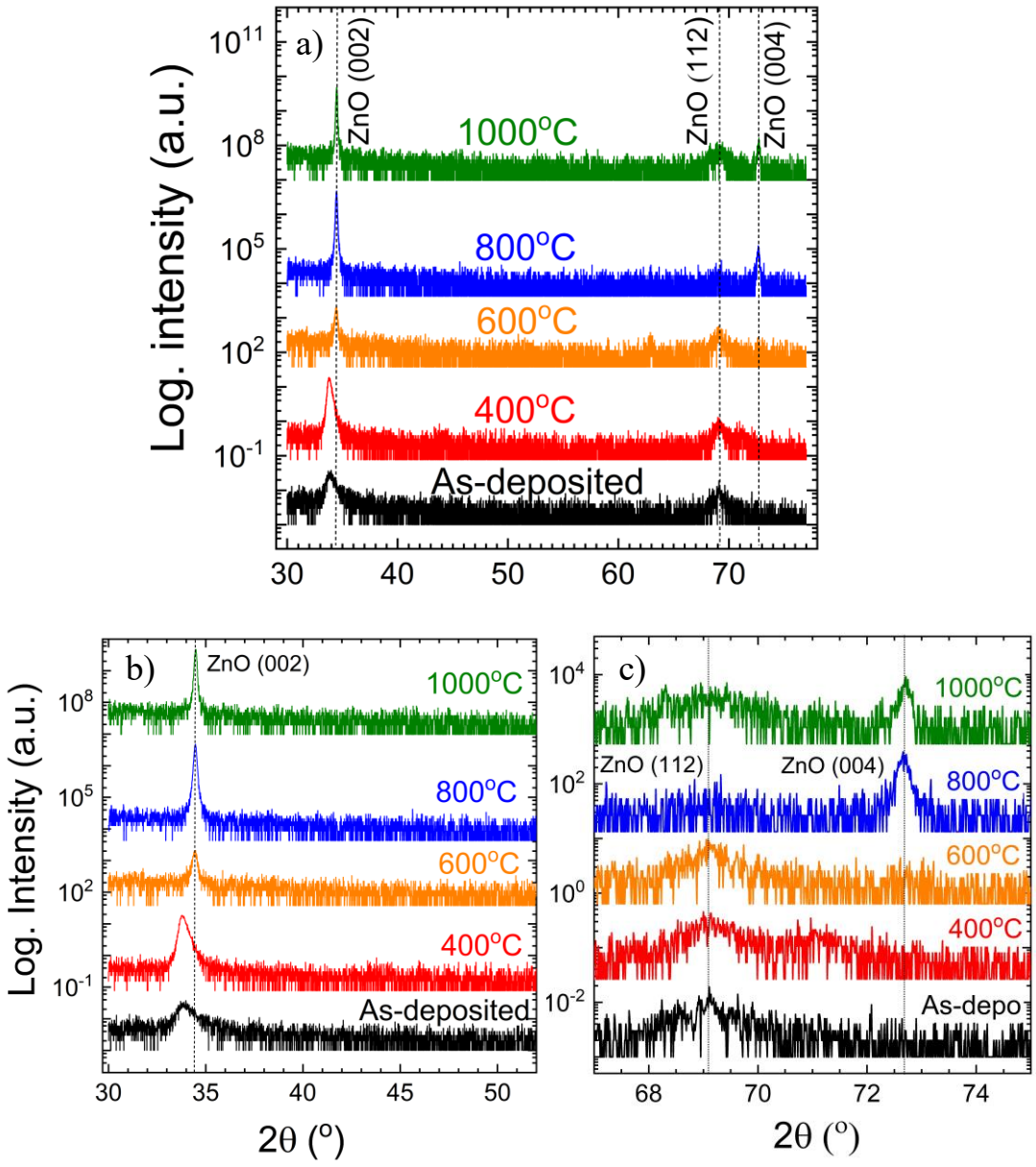

Figure 3.10 XRD curves of ZnO:CoN film for various T_{an} ranges. a). 30–76 °C, b). 30–37 °C, c). 67–76 °C.

This shift indicates that residual stress is induced by the difference in ionic radii between the impurity and matrix elements[59–61]. Substituting N for O in the ZnO:Co crystal lattice expands the crystal lattice along the c-axis, producing a slight shift in the XRD peak.

Furthermore, T_{an} of 800 and 1000 °C improve crystal quality owing to the reduced nitrogen content as a defect. The vacancies left by nitrogen are filled by O, thus bringing the Zn to O ratio close to that of the ZnO bulk. For all T_{an}, except 800 °C, a weak diffraction peak corresponding to the ZnO (112) plane is observed for all films, while peaks corresponding to the ZnO (004) plane are found at 800 and 1000 °C. The high intensity peak in the (002) plane, compared to that for the (112) and (004) planes, indicates that all films have a wurtzite structure with a preferred c-axis orientation[34].

The lattice parameters (a, b, c) were calculated by utilizing Bragg's law from the hexagonal structure of ZnO[62]. This was done to confirm the effect of different T_{an}.

$$d = \frac{\lambda}{2\,sin\theta} \tag{3.1}$$

$$c = \frac{\lambda}{sin\theta} \tag{3.2}$$

$$\frac{1}{d^2} = \frac{4}{3}\left(\frac{h^2+hk+k^2}{a^2}\right) + \left(\frac{l}{c}\right)^2 \tag{3.3}$$

The interplanar distance, diffraction angle, and XRD wavelength of CuKα (1.54 Å) are denoted by d, λ, and θ, respectively, while the Miller indices h, k, and l represent the crystallographic planes.

The dependence of the lattice parameters on T_{an} is plotted in Fig. 3.11a. According to the calculations, the c/a ratios for the as-deposited, 400, 600, and 1000 °C conditions are 1.6697, 1.6782, 1.6339, and 1.6272, respectively. Except for the T_{an} of 400 °C, the increase in T_{an} induces a shortening of the c-axis and a slight expansion of the a-axis lengths, resulting in low alterations in the crystal-lattice volume.

These findings indicate that increasing T_{an} above 400 °C, which involves the substitution of N and O concentrations, decreases the c/a ratio, eventually approximating the ZnO bulk ratio of 1.6333. Fig. 3.11b demonstrates the effect of N/(N+O) ratio on the lattice parameters. The change in lattice parameters occurs because of reducing impurities with ionic radii larger than that of the host elements. The ionic radius of N^{3-} (1.46 Å) is larger than that of O^{2-} (1.38 Å), while the ionic radius of Co^{2+} (0.58 Å) is slightly lower than that of Zn^{2+} (0.60 Å) and O^{-2} [25,59,61]. This difference in ionic radii may result in alterations in the

distances of the Zn–N and Zn–O bonds[63].

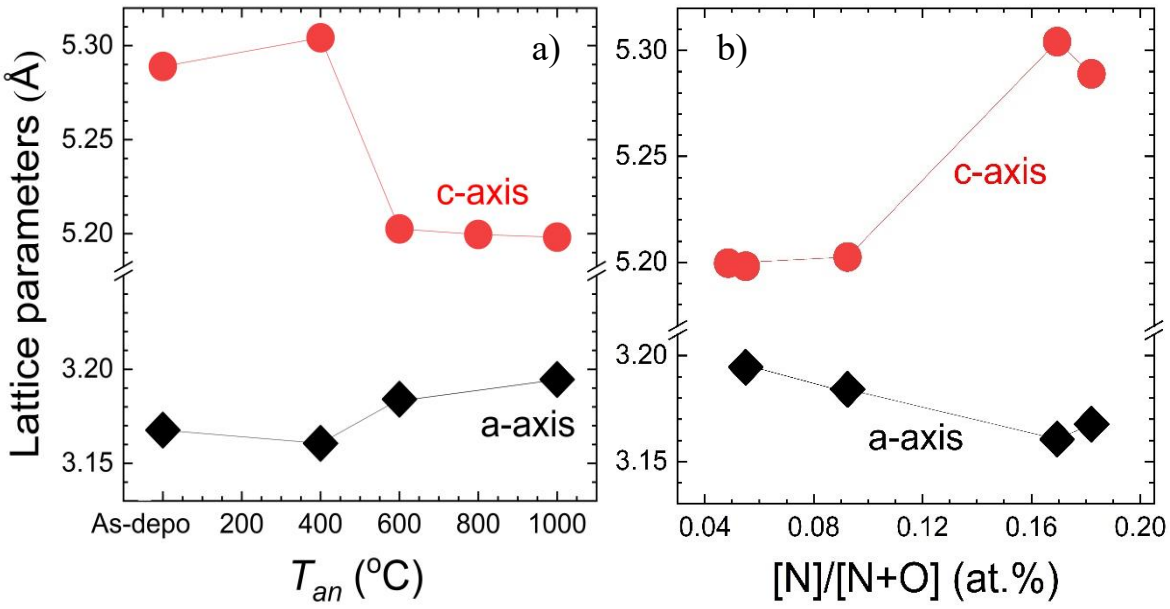

Figure 3.11 Dependence of the lattice parameters on (a). T_{an} and (b). N–O ratio in the ZnO:CoN film.

The presence of impurities that affect the crystal quality of the ZnO:CoN film is evaluated using the full width at half maximum (FWHM) value and the grain size using Scherer's formula (Eq. 3.4). FWHM is (β) determined by counting the width of the peak at half of its maximum intensity, corresponding to the diffraction peak (002) plane.

$$D = \frac{0.9\lambda}{\beta cos\theta} \tag{3.4}$$

Fig. 3.12 shows the effect of T_{an} on both the grain size and FWHM value of the ZnO:CoN film. Increasing the T_{an}, which induces a substitution of N and O, leads to a notable decrease in the FWHM and increase in the grain size. Specifically, the film annealed at 400 °C exhibits the highest FWHM and smallest grain size among all films, suggesting a higher presence of structural defects in the ZnO:CoN film. Conversely, the film annealed at 1000 °C displays the largest grain size and the lowest FWHM value, indicating higher crystal quality.

The effect of inhomogeneity on the surface morphology profiles of the as-deposited films and films with T_{an} of 400, 800, and 1000 °C is evaluated via AFM for a scan size of $5 \times 5\ \mu m^2$ and $2 \times 2\ \mu m^2$, as shown in Fig. 3.13. The increase in grain size is observed

from the surface morphology and is consistent with the increased grain size measured by XRD. In the as-deposited condition, the grain boundaries are clearly observed on the surface with a grain size of 113.7 nm and RMS of 2.5 nm. As T_{an} increases, the grain boundaries coalesce to form islands, resulting in an increase in the grain size to 134.9, 426.6, and 634.2 nm. Concurrently, the roughness increases, to an RMS of 3.7, 12.2, and 14.9 nm, respectively.

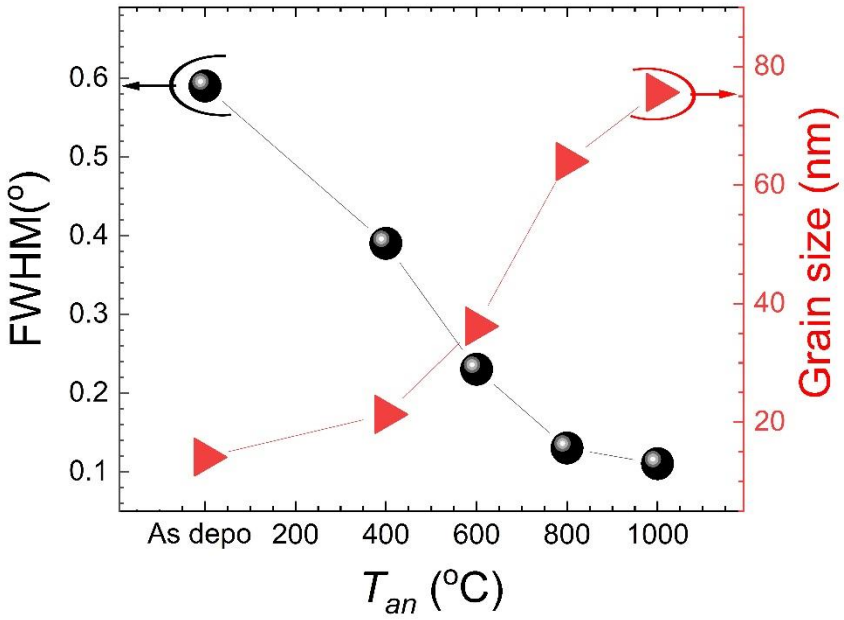

Figure 3.12 Dependence of FWHM and grain size of the ZnO:CoN film on T_{an}.

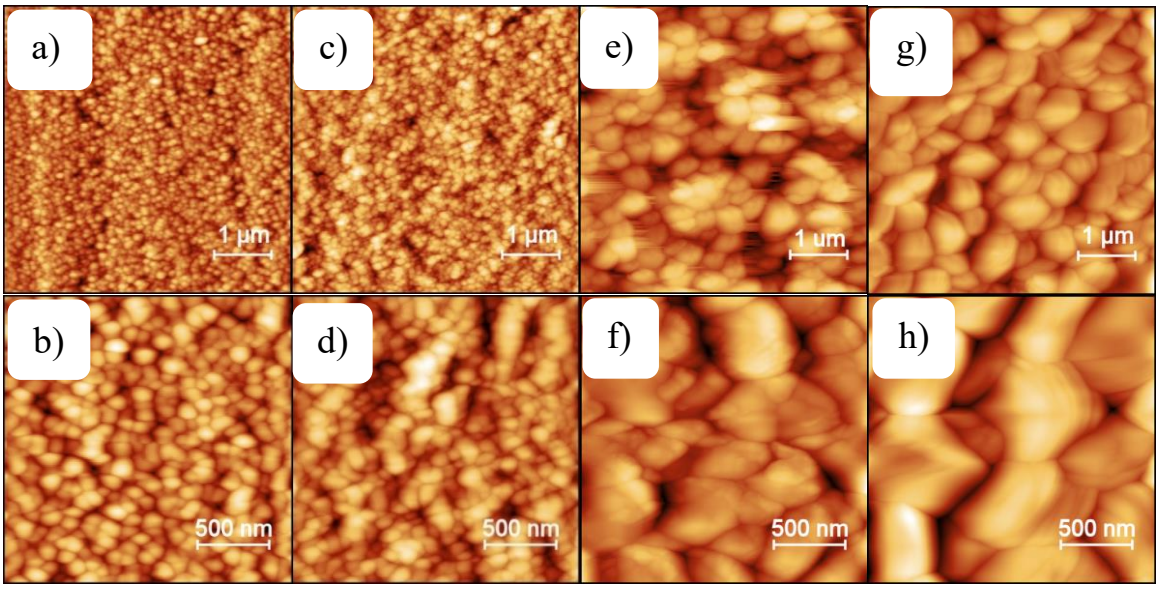

Figure 3.13 Surface profile of ZnO:CoN films for different postannealing times. (a–b), (c–d), (e–f), (g–h). for the as-deposited films and films with T_{an} of 400 , 800, and 1000 °C, respectively.

The field-dependent magnetization of the ZnO:CoN films measured by SQUID at room temperature (300 K) for different T_{an} is presented in Fig. 3.14. The paramagnetic background of the substrate is discounted. The clear hysteresis loop with high magnetization is obtained only for a T_{an} of 400 °C. The absence of coercivity in the hysteresis loop indicates that superparamagnetic properties are dominant in this film.

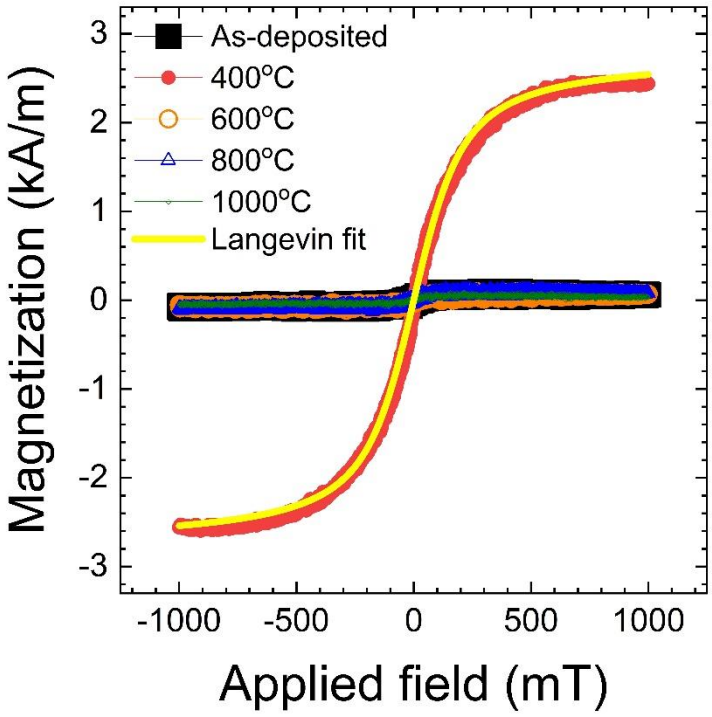

Figure 3.14 Dependence of magnetization on the applied field of the ZnO:CoN films with various T_{an}

To confirm the superparamagnetism of the film with a T_{an} of 400 °C, the hysteresis loop was fitted by the Langevin function with the equation as follows[29,62,64]:

$$M = M_s\left(coth\frac{\mu H}{k_B T}\right) - \left(\frac{k_B T}{\mu H}\right) \tag{3.5}$$

where M_s, μ, H, and k_B are the saturation field, magnetic moment, applied field, and Boltzmann constant, respectively. The fitting showed a good fit for a saturation field of 2.7 kA/m, indicating the existence of superparamagnetic properties in the film, as reported by others[29,65].

The unique magnetic properties of the ZnO:CoN films, especially for a T_{an} of 400 °C, drove author to explore these conditions more deeply by measuring the magnetization at low

temperatures. Fig. 3.15 shows the hysteresis loop of a ZnO:CoN film at 4 K. The observed coercive field was 58.1 mT, which indicated that the film had ferromagnetic properties in this state.

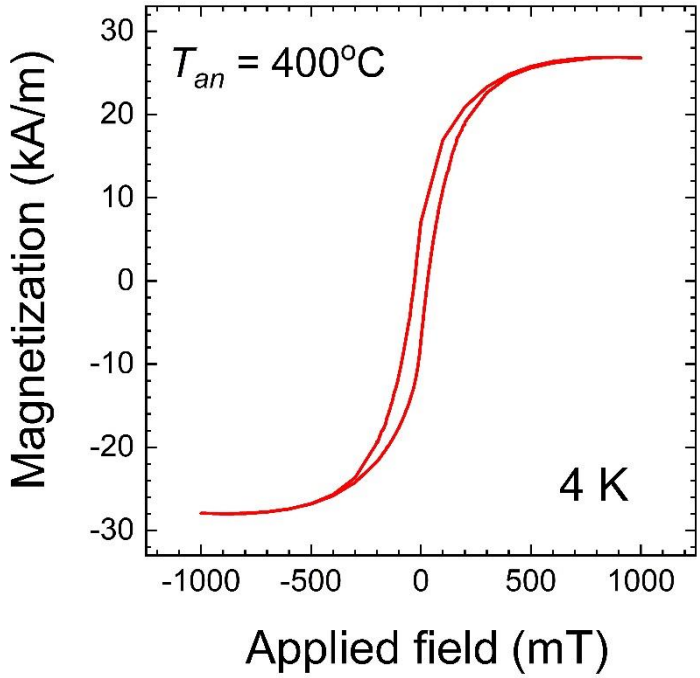

Figure 3.15 Hysteresis loop for ZnO:CoN film at a T_{an} of 400 °C measured at 4 K.

The curve in Fig. 3.16 demonstrates the temperature-dependent magnetization at 10 mT for both FC and ZFC protocols. The magnetization in the ZFC curve reaches its peak (T_b) at 38 K and decreases afterward. The ZFC–FC curve shows clear bifurcation, which corroborates that superparamagnetic properties exist in this film[29,30]. The magnetization in the FC curve increases exponentially with decreasing temperature, indicating that the magnetic moment continues to align as the thermal energy decreases. The reduction in thermal energy leads to a decrease in the fluctuation of magnetic moment. At low temperatures, typically below 10 K, the magnetic moments tend to align and remain aligned even after the external field is removed. This phenomenon explains the observation of hysteresis loops at low temperatures.

Figure 3.17 presents the ZFC–FC curves of ZnO:Co films with a T_{an} of 400 °C for various applied fields. Similar to ZnO:Co without nitrogen and other reports, an increase in the applied field reduces T_b and collapses the bifurcation between the ZFC and FC curves. This behavior indicates that the Co element in ZnO:Co is nanoscale, resulting in a reduced

energy barrier when exposed to an applied field. Consequently, thermal fluctuations can reorient the superparamagnetic moments at lower temperatures[31–33]. Furthermore, the magnetization observed in the FC curve at 300 K is non-zero, indicating that the Curie temperature of this film exceed room temperature[34].

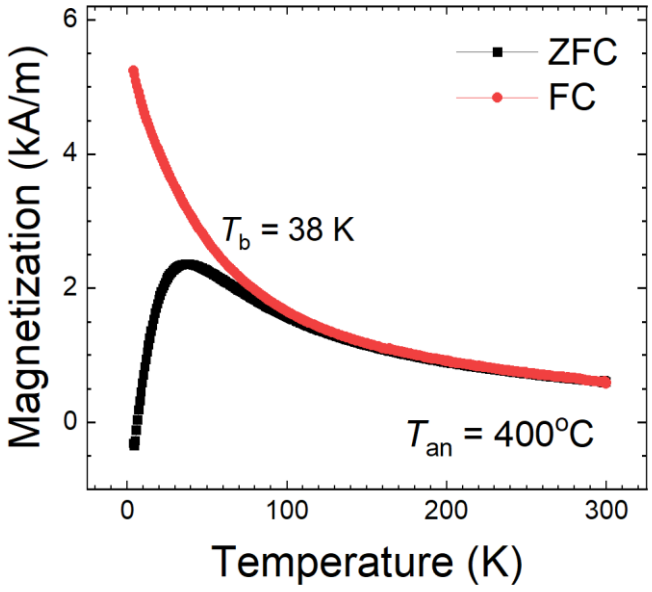

Figure 3.16 ZFC-FC curve of ZnO:CoN film for T_{an} 400 ℃.

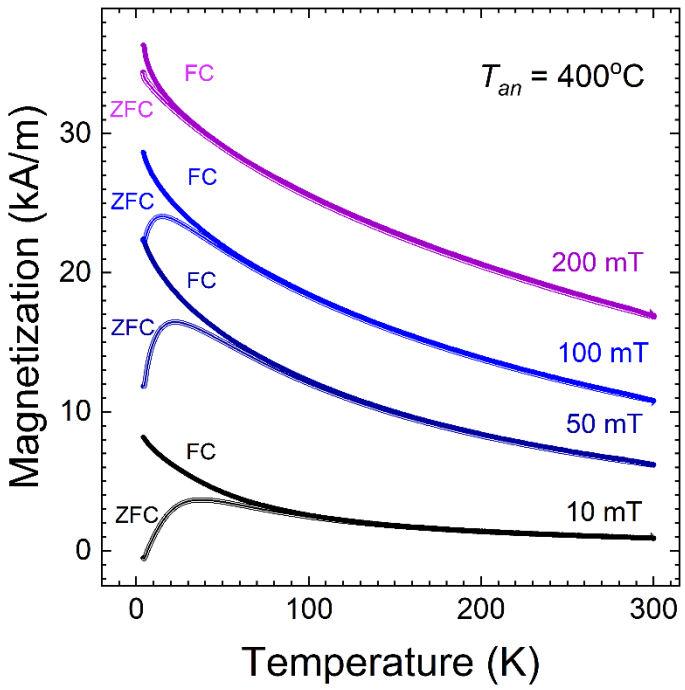

Figure 3.17 ZFC–FC curve of ZnO:CoN film under various applied fields for T_{an} of 400 °C.

To explore the origin of the magnetic properties of the ZnO:CoN film annealed at 400 °C, Co clusters, which significantly affect the magnitude of magnetization, was evaluated by XPS measurements. Clear peaks of Co, O, and Zn were observed in this curve, as shown in Fig. 3.18, indicating that these elements were present, as measured by XRF.

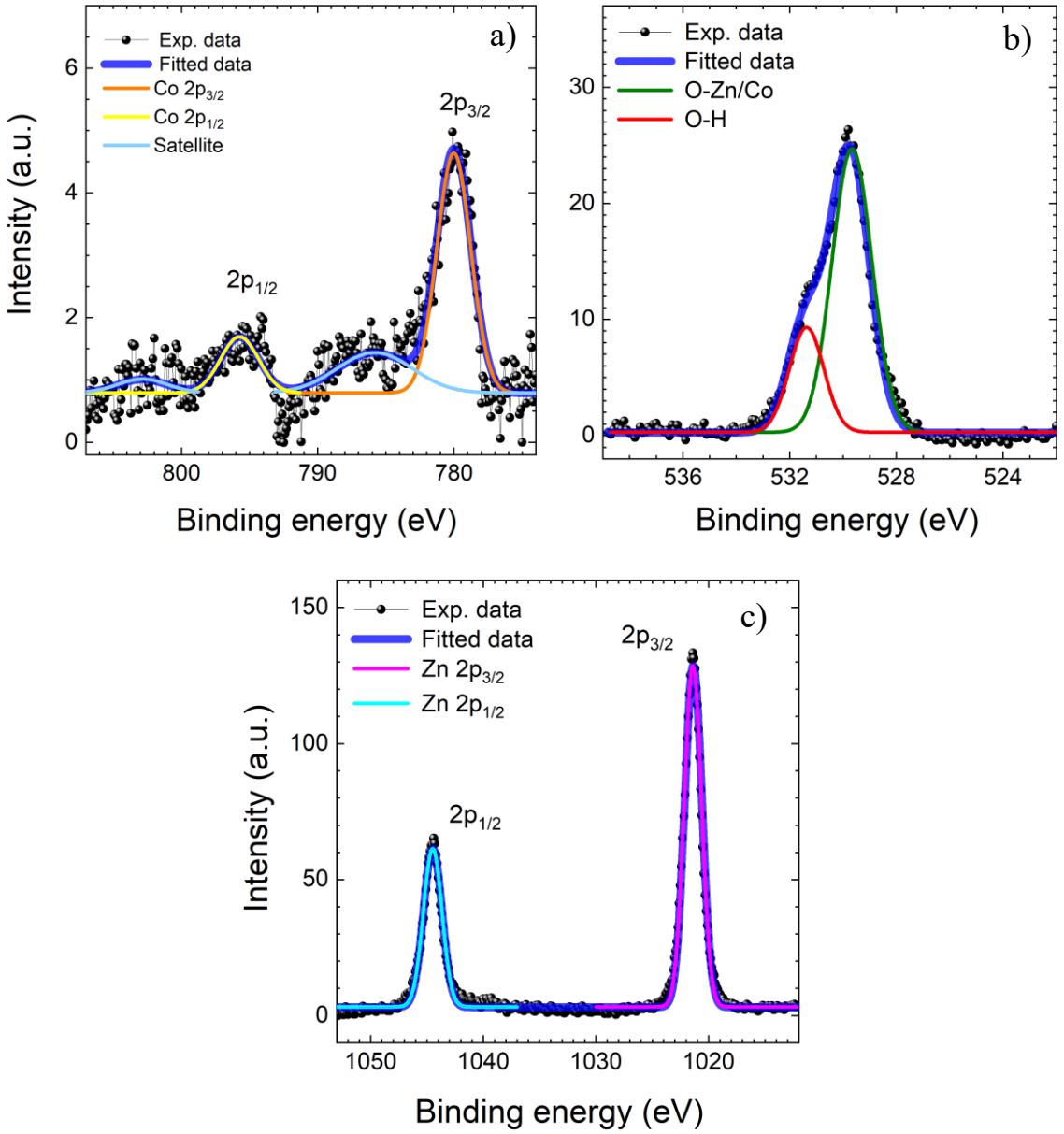

Figure 3.18 XPS spectra of ZnO:CoN film for T_{an} of 400 °C. a). Co 2p, b). O 1s, c). Zn 2p.

The difference in the binding energies of the Co states between the $2p_{1/2}$ and $2p_{3/2}$ peaks is 15.6 eV, as shown in Fig. 3.18a, indicating the absence of Co clusters[25,34,41,47–49].

The presence of Co below the solubility limit of ZnO is believed to be the main factor behind the absence of Co clusters in the film. The O state in the film measured by XPS was deconvoluted into two peaks (Fig. 3.18b). The higher energy peak at 531.4 eV corresponded to O-H[21], while the lower energy peak at 529.6 eV corresponded to O^{2-}. Compared to the ZnO:Co film without N, the addition of N to ZnO:Co results in reducing the O-H intensity. The reduction of O-H in ZnO:CoN could be attributed to filling by the N^{3-}. The peaks of Zn $2p_{3/2}$ and $2p_{1/2}$ for the ZnO:CoN film were clearly observed at 1021.5 and 1044.6 eV, as shown in Fig. 3.18c. The ΔE was 23.1 eV, corresponding to the bivalent state of Zn^{2+} [41,47–49].

According to these findings, the ferromagnetic–superparamagnetic properties observed in the ZnO:CoN film with T_{an} of 400 °C cannot be attributed to the cobalt clusters. The films annealed at 400 °C exhibit low crystalline quality, as evidenced by the high FWHM values and a large disparity in the lattice parameters. This could potentially result in nanoscale inhomogeneities that would raise the critical temperature. The presence of O_v or the deficiency of O, indicated by XPS and XRF, are also thought to affect the ferromagnetic properties of the ZnO:CoN film. Subsequently, after annealing at 600, 800, and 1000 °C, the film reverts to paramagnetic properties. These findings align with the previous theories proposing nanoscale inhomogeneities and the presence of O_v to account for these observations. The film exhibits an increase in the grain size under these conditions, as the O concentration increases and N concentration decreases. Compared to ZnO:Co without nitrogen, the presence of N reduces the coercivity of the film and increases T_b. The loss of coercivity in the ZnO:CoN film is attributed to the disappearance of the Co clusters, with the addition of N. The increase in H_c and T_b, indicating improved ferromagnetic properties, is attributed to the nanoscale inhomogeneity in the ZnO:CoN film. A detailed discussion on the effect of nanoscale inhomogeneities on the magnetic properties will be elaborated in the next chapter.

3.3.3 *Role of Oxygen in the ZnO:Co Film on the Structure and Magnetic Properties*

Previous studies have demonstrated that O_v and Co play important roles in the structure and magnetic properties of ZnO:Co films. In this section, the concentrations of Co and O_v are effectively reduced by introducing O_2 gas during deposition. The addition of O_2 gas serves two purposes. First, it helps to add the O element by filling these voids in the crystal lattice, thus maintaining the stoichiometry of the film. Second, O_2 is a reactive gas that can mitigate impurities, specifically Co, which can be more easily reduced. The role of O in the structure and magnetic properties of the ZnO:Co film is confirmed by reducing Co and adding O element. The total thickness measured using a Dektak profilometer is ~360 nm. Table 3.1 shows the composition of the ZnO:Co films under various gas conditions, as analyzed by XRF. The concentration of Zn is relatively constant for all ZnO:Co film conditions. In contrast, the addition of reactive gases (both O and N) during deposition reduces the Co concentration (by similar amounts).

Table 3.1 Composition of ZnO:Co film with different gas additions

Gas	Zn	O	Co	N
	Atomic density (%)			
Ar	44.9	35.8	19.3	-
Ar + N_2	49.7	35.6	7.4	7.3
Ar + O_2	45.6	47.0	7.4	-

Figure 3.19a depicts the XRD pattern of ZnO:Co in the 30–48° range under different gas atmospheres during deposition. Across all films, distinct diffraction peaks are consistently observed at approximately 34°, corresponding to the ZnO (002) plane. Furthermore, the observed shift of the (002) peak in Fig. 3.19b can be attributed to variations in the ionic radii of the impurities[49,59,60]. Specifically, in this case, Co^{2+} (0.58 Å) has a smaller ionic radius than O^{2-} (0.60 Å), while N^{3-} has a larger ionic radius than O^{2-}. The addition of O into ZnO:Co during deposition improves the crystal quality, as evidenced by the lowest FWHM compared to other conditions. This is due to the reduction of Co as an impurity and the composition ratio between Zn and O being close to one.

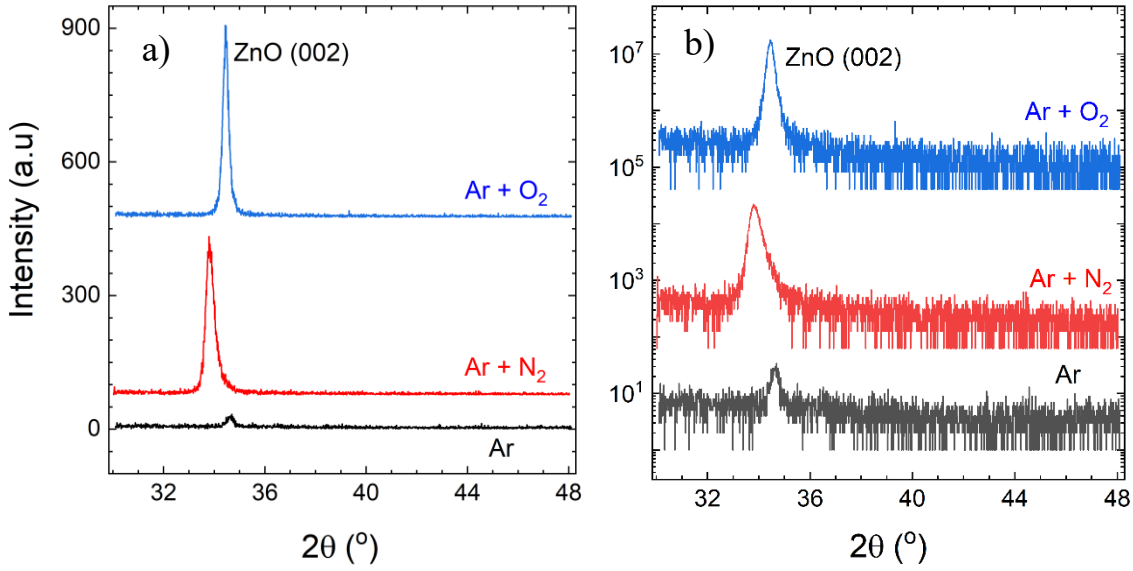

Figure 3.19 Comparison of XRD curves of ZnO:Co film under different gas additions at a T_{an} of 400 °C. a). Normal intensity, b). Log. intensity

Fig. 3.20 shows the comparison of the hysteresis loops of the ZnO:Co films deposited using different gases. The inset of Fig. 3.20, capturing M_s and H_c within a low range, demonstrates the hysteresis loop observed during the growth of ZnO:Co upon introducing O_2. The addition of reactive gas reduces H_c and M_s. Notably, the total concentration of Co and O–N in the film growth by O_2 and N_2 gases are comparable, while M_s and H_c exhibit significant discrepancies. These findings support the notion that the inhomogeneity introduced into the DMS material, specifically in the case of ZnO:CoN via the NMC method, significantly enhances both M_s and H_c, without the formation of Co clusters.

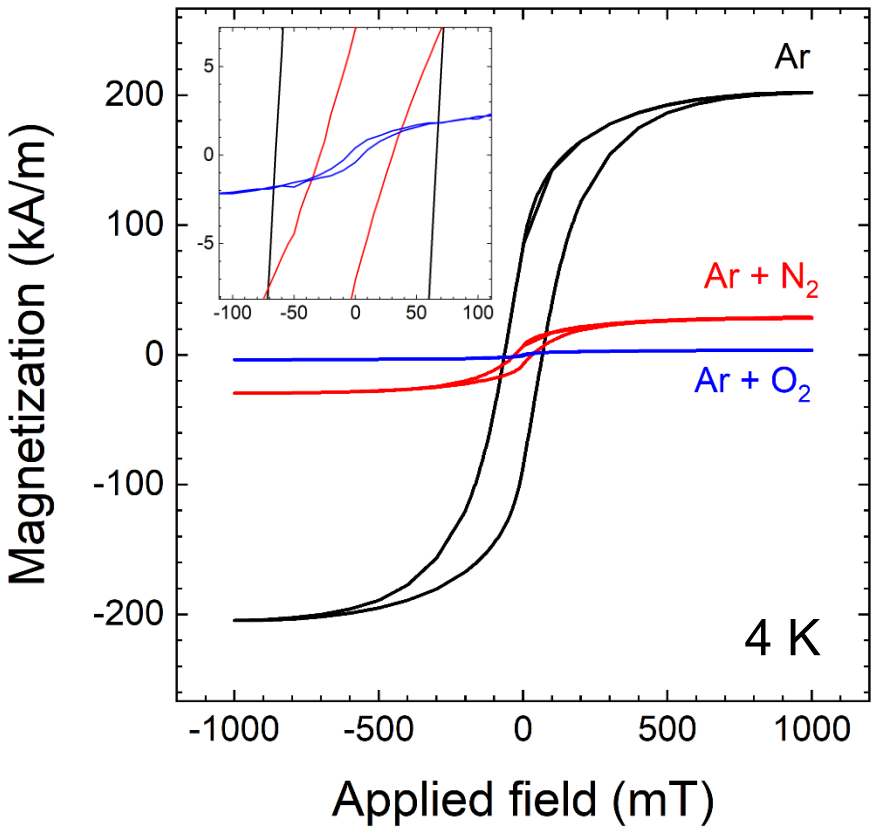

Figure 3.20 Hysteresis loop for ZnO:CoN film under different gas additions for a T_{an} of 400 °C measured at 4 K.

3.4 Conclusions

The physical and chemical properties of the ZnO:Co films fabricated by NMC were investigated. The inhomogeneities in the structure, represented by lattice parameters, grain sizes, and stoichiometry of ZnO, affect the magnetic properties. The superparamagnetic–ferromagnetic properties of the ZnO:CoN films with the highest inhomogeneous structure were obtained at T_{an} of 400 °C, which was the optimum T_{an} before the desorption of N. The analysis of the superparamagnetic–ferromagnetic properties suggested that the incorporation of Co and N atoms into the ZnO structure significantly deteriorated the grain size and produced disparities in both the stoichiometry and lattice of the ZnO:CoN film at 400 °C. Moreover, elevating the T_{an} to 600, 800, and 1000 °C reduced the N concentration, leading to an enhancement in the grain size and lattice parameters more closely resembling those of bulk ZnO. The loss of superparamagnetic–ferromagnetic properties at high T_{an} indicated that the homogeneous structure had reduced the magnetization of the film. In comparison to ZnO:Co without nitrogen, ferromagnetic properties were also observed at a T_{an} of 400 °C. Meanwhile, the as-deposited case and case with a T_{an} of 800 °C exhibited paramagnetism. In contrast to ZnO:CoN, the origin of ferromagnetism in the ZnO:Co film was dominated by the Co cluster and O_v. Moreover, the growth of ZnO:Co using oxygen corroborated the hypothesis positing that a homogeneous structure and low Co content led to reduced M_s and H_c. Based on these studies, NMC has been proven to be an effective technique to control the inhomogeneity in the structure and the phase of magnetic properties of the ZnO:Co film. This method has the potential to be applied in the development of DMS materials.

References

1. T. Dietl, H. Ohno, F. Matsukura, J. Cibert, D. Ferrand, *Science (80-.).* **287**, 1019–1022 (2000).
2. D. D. Awschalom, M. E. Flatté, *Nat. Phys.* **3**, 153–159 (2007).
3. Ü. Özgür, Y. I. Alivov, C. Liu, A. Teke, M. A. Reshchikov, S. Doğan, V. Avrutin, S. J. Cho, H. Morkoç, *J. Appl. Phys.* **98**, 1–103 (2005).
4. P. Kumari, K. P. Misra, S. Chattopadhyay, S. Samanta, *Mater. Today Proc.* **43**, 3297–3302 (2021).
5. M. Shatnawi, A. M. Alsmadi, I. Bsoul, B. Salameh, G. A. Alna'Washi, F. Al-Dweri, F. El Akkad, *J. Alloys Compd.* **655**, 244–252 (2016).
6. C. B. Fitzgerald, M. Venkatesan, J. G. Lunney, L. S. Dorneles, J. M. D. Coey, *Appl. Surf. Sci.* **247**, 493–496 (2005).
7. M. Ivill, S. J. Pearton, S. Rawal, L. Leu, P. Sadik, R. Das, A. F. Hebard, M. Chisholm, J. D. Budai, D. P. Norton, *New J. Phys.* **10** (2008), doi:10.1088/1367-2630/10/6/065002.
8. R. Siddheswaran, R. Medlín, C. E. Jeyanthi, S. G. Raj, R. V. Mangalaraja, *Appl. Phys. A Mater. Sci. Process.* **125**, 1–9 (2019).
9. T. J. Castro, P. A. M. Rodrigues, A. C. Oliveira, F. Nakagomi, J. Mantilla, J. A. H. Coaquira, A. Franco, H. V. S. Pessoni, P. C. Morais, S. W. Da Silva, *J. Appl. Phys.* **121** (2017), doi:10.1063/1.4973526.
10. B. Huang, D. Zhu, X. Ma, *Appl. Surf. Sci.* **253**, 6892–6895 (2007).
11. H. S. Hsu, J. C. A. Huang, Y. H. Huang, Y. F. Liao, M. Z. Lin, C. H. Lee, J. F. Lee, S. F. Chen, L. Y. Lai, C. P. Liu, *Appl. Phys. Lett.* **88** (2006), doi:10.1063/1.2212277.
12. A. Simimol, A. A. Anappara, S. Greulich-Weber, P. Chowdhury, H. C. Barshilia, *J. Appl. Phys.* **117** (2015), doi:10.1063/1.4922050.
13. M. P. F. de Godoy, X. Gratens, V. A. Chitta, A. Mesquita, M. M. de Lima, A. Cantarero, G. Rahman, J. M. Morbec, H. B. de Carvalho, *J. Alloys Compd.* **859**, 157772 (2021).
14. L. R. Shah, H. Zhu, W. G. Wang, B. Ali, T. Zhu, X. Fan, Y. Q. Song, Q. Y. Wen, H. W. Zhang, S. I. Shah, J. Q. Xiao, *J. Phys. D. Appl. Phys.* **43** (2010), doi:10.1088/0022-3727/43/3/035002.

15. A. Chakraborty, R. Bouzerar, S. Kettemann, G. Bouzerar, *Phys. Rev. B - Condens. Matter Mater. Phys.* **85**, 1–7 (2012).
16. K. Kuwahara, N. Itagaki, K. Nakahara, D. Yamashita, G. Uchida, K. Kamataki, K. Koga, M. Shiratani, *Thin Solid Films*. **520**, 4674–4677 (2012).
17. I. Suhariadi, N. Itagaki, M. Shiratani, *ACS Appl. Nano Mater.* **3**, 2480–2490 (2020).
18. N. Itagaki, K. Kuwahara, K. Matsushima, D. Yamashita, H. Seo, K. Koga, M. Shiratani, *Opt. Eng.* **53**, 087109 (2014).
19. H. Ren, G. Xiang, G. Gu, X. Zhang, *Mater. Lett.* **122**, 256–260 (2014).
20. S. Aksu, E. Bacaksiz, S. Ylmaz, I. Polat, M. Altunbaş, M. Türksoy, R. Topkaya, K. Özdogan, *Phys. E Low-Dimensional Syst. Nanostructures*. **44**, 1244–1249 (2012).
21. H. Idriss, *Surf. Sci.* **712**, 2–7 (2021).
22. S. Yang, A. B. Pakhomov, S. T. Hung, B. Ma, C. Y. Wong, *INTERMAG Eur. 2002 - IEEE Int. Magn. Conf.* **38**, 2877–2879 (2002).
23. H. J. Lee, S. Y. Jeong, C. R. Cho, C. H. Park, *Appl. Phys. Lett.* **81**, 4020–4022 (2002).
24. X. L. Li, Z. L. Wang, X. F. Qin, H. S. Wu, X. H. Xu, G. A. Gehring, *J. Appl. Phys.* **103** (2008), doi:10.1063/1.2832652.
25. B. Salameh, A. M. Alsmadi, M. Shatnawi, *J. Alloys Compd.* **835**, 155287 (2020).
26. P. Shunmuga Sundaram, T. Sangeetha, S. Rajakarthihan, R. Vijayalaksmi, A. Elangovan, G. Arivazhagan, *Phys. B Condens. Matter*. **595**, 412342 (2020).
27. L. Dejam, S. Mohammad Elahi, H. H. Nazari, H. Elahi, S. Solaymani, A. Ghaderi, *J. Mater. Sci. Mater. Electron.* **27**, 685–696 (2016).
28. F. K. Shan, G. X. Liu, W. J. Lee, B. C. Shin, *J. Appl. Phys.* **101** (2007), doi:10.1063/1.2437122.
29. M. Opel, K. W. Nielsen, S. Bauer, S. T. B. Goennenwein, J. C. Cezar, D. Schmeisser, J. Simon, W. Mader, R. Gross, *Eur. Phys. J. B.* **63**, 437–444 (2008).
30. A. Chanda, S. Gupta, M. Vasundhara, S. R. Joshi, G. R. Mutta, J. Singh, *RSC Adv.* **7**, 50527–50536 (2017).
31. J. H. Park, M. G. Kim, H. M. Jang, S. Ryu, Y. M. Kim, *Appl. Phys. Lett.* **84**, 1338–1340 (2004).
32. S. R. Shinde, S. B. Ogale, J. S. Higgins, H. Zheng, A. J. Millis, V. N. Kulkarni, R. Ramesh, R. L. Greene, T. Venkatesan, *Phys. Rev. Lett.* **92**, 96–99 (2004).

33. S. Zhou, G. Talut, K. Potzger, A. Shalimov, J. Grenzer, W. Skorupa, M. Helm, J. Fassbender, E. Čižmár, S. A. Zvyagin, J. Wosnitza, *J. Appl. Phys.* **103** (2008), doi:10.1063/1.2905236.
34. X. J. Liu, C. Song, F. Zeng, F. Pan, *Thin Solid Films*. **516**, 8757–8761 (2008).
35. S. Kumar, P. D. S. Surender, *J. Mater. Sci. Mater. Electron.* **29**, 11719–11729 (2018).
36. M. P. F. De Godoy, A. Mesquita, W. Avansi, P. P. Neves, V. A. Chitta, W. B. Ferraz, M. A. Boselli, A. C. S. Sabioni, H. B. De Carvalho, *J. Alloys Compd.* **555**, 315–319 (2013).
37. L. C. Nistor, C. Ghica, V. Kuncser, D. Pantelica, J. J. Grob, G. Epurescu, M. Dinescu, *J. Phys. D. Appl. Phys.* **46** (2013), doi:10.1088/0022-3727/46/6/065003.
38. N. Jedrecy, H. J. Von Bardeleben, D. Demaille, *Phys. Rev. B - Condens. Matter Mater. Phys.* **80**, 1–6 (2009).
39. N. Jedrecy, M. Hamieh, C. Hebert, J. Perriere, *Nanoscale*. **9**, 10431–10439 (2017).
40. H. Gu, W. Zhang, Y. Xu, M. Yan, *Appl. Phys. Lett.* **100** (2012), doi:10.1063/1.4717741.
41. P. R. Chithira, T. Theresa John, *J. Magn. Magn. Mater.* **496**, 165928 (2020).
42. Q. Liu, C. L. Gan, C. L. Yuan, G. C. Han, *Appl. Phys. Lett.* **92**, 5–8 (2008).
43. M. Tay, Y. Wu, G. C. Han, T. Chong, Y. K. Zheng, S. J. Wang, Y. Chen, X. Pan, *J. Appl. Phys.* **100** (2006), doi:10.1063/1.2348632.
44. Y. Gao, G. Li, Z. Wang, S. Liu, Q. Wang, *Appl. Surf. Sci.* **416**, 521–526 (2017).
45. Z. W. Jin, M. Murakami, T. Fukumura, Y. Matsumoto, A. Ohtomo, M. Kawasaki, H. Koinuma, *J. Cryst. Growth*. **214**, 55–58 (2000).
46. A. Jilani, M. S. Abdel-wahab, H. Y. Zahran, I. S. Yahia, A. A. Al-Ghamdi, A. Alshahrie, A. M. El-Naggar, *Optik (Stuttg).* **164**, 143–154 (2018).
47. N. L. Tarwal, K. V. Gurav, T. Prem Kumar, Y. K. Jeong, H. S. Shim, I. Y. Kim, J. H. Kim, J. H. Jang, P. S. Patil, *J. Anal. Appl. Pyrolysis*. **106**, 26–32 (2014).
48. K. C. Kim, E. kwon Kim, Y. S. Kim, *Superlattices Microstruct.* **42**, 246–250 (2007).
49. V. Pazhanivelu, A. Paul Blessington Selvadurai, R. Murugaraj, I. Panneer Muthuselvam, F. C. Chou, *J. Mater. Sci. Mater. Electron.* **27**, 8580–8589 (2016).
50. U. Ilyas, P. Lee, T. L. Tan, R. V. Ramanujan, S. Zhang, R. Chen, H. D. Sun, R. S. Rawat, *Int. J. Mod. Phys. Conf. Ser.* **32**, 1460341 (2014).

51. U. Ilyas, R. S. Rawat, T. L. Tan, P. Lee, R. Chen, H. D. Sun, L. Fengji, S. Zhang, *J. Appl. Phys.* **111** (2012), doi:10.1063/1.3679129.
52. M. Wang, L. Jiang, E. J. Kim, S. H. Hahn, *RSC Adv.* **5**, 87496–87503 (2015).
53. M. Gupta, Seema, N. Pandey, S. M. Amir, S. Pütter, S. Mattauch, *J. Magn. Magn. Mater.* **489**, 165376 (2019).
54. N. Pandey, M. Gupta, R. Gupta, S. M. Amir, J. Stahn, *Appl. Phys. A Mater. Sci. Process.* **125**, 1–8 (2019).
55. M. H. N. Assadi, Y. B. Zhang, S. Li, *J. Appl. Phys.* **105** (2009), doi:10.1063/1.3075903.
56. S. Berg, T. Nyberg, *Thin Solid Films*. **476**, 215–230 (2005).
57. V. Kambilafka, P. Voulgaropoulou, S. Dounis, E. Iliopoulos, M. Androulidaki, K. Tsagaraki, V. Šály, M. Ružinský, P. Prokein, E. Aperathitis, *Thin Solid Films*. **515**, 8573–8576 (2007).
58. J. T. Gudmundsson, *Plasma Sources Sci. Technol.* **29** (2020), doi:10.1088/1361-6595/abb7bd.
59. B. Yao, D. Z. Shen, Z. Z. Zhang, X. H. Wang, Z. P. Wei, B. H. Li, Y. M. Lv, X. W. Fan, L. X. Guan, G. Z. Xing, C. X. Cong, Y. P. Xie, *J. Appl. Phys.* **99** (2006), doi:10.1063/1.2208414.
60. S. Kunj, K. Sreenivas, *Curr. Appl. Phys.* **16**, 748–756 (2016).
61. C. W. Zou, H. J. Wang, M. L. Yi, M. Li, C. S. Liu, L. P. Guo, D. J. Fu, T. W. Kang, *Appl. Surf. Sci.* **256**, 2453–2457 (2010).
62. S. Ghoshal, P. S. Anil Kumar, *J. Magn. Magn. Mater.* **320**, 93–96 (2008).
63. C. H. Park, S. B. Zhang, S. H. Wei, *Phys. Rev. B - Condens. Matter Mater. Phys.* **66**, 1–3 (2002).
64. B. Martínez, F. Sandiumenge, L. Balcells, J. Arbiol, F. Sibieude, C. Monty, *Phys. Rev. B - Condens. Matter Mater. Phys.* **72**, 1–8 (2005).
65. V. Ney, V. Venkataraman, B. Henne, K. Ollefs, F. Wilhelm, A. Rogalev, A. Ney, *J. Appl. Phys.* **119** (2016), doi:10.1063/1.4947455.

Chapter 4

Impact of nanoscale inhomogeneity in ZnO:CoN film on magnetic properties

4.1 Introduction

Transition-metal (TM)–doped ZnO presents a compelling avenue for the development of diluted magnetic semiconductor (DMS)[1]. Among these TMs, Co stands out because of its substantial magnetic moment and ionic radius closely matching that of Zn, facilitating high solubility within ZnO and consequently elevating the critical temperature. However, a significant hurdle faced by Co-doped ZnO (ZnO:Co) is the challenge of elevating the critical temperature to room temperature without encountering secondary phases or Co segregation. Numerous studies have explored ways to achieve this goal, such as by adjusting the Co concentration[2–5], oxygen vacancies[6–8], and Zn interstitial defects[9,10]. Despite these efforts, the exact origin of the magnetization or the mechanisms that drive the increase in critical temperature remain controversial topics. Therefore, an alternative methodology is imperative to realize a robust ferromagnetic state in ZnO-based DMS.

In 2012, Chakraborty et al. conducted a groundbreaking study revealing that nanoscale inhomogeneities of TM atoms within a semiconductor matrix could enhance the Curie temperature by up to 1600%[11]. This enhancement occurred even when the total density of TMs and the crystalline structure remain unchanged, highlighting the critical role of TM distribution in influencing the Curie temperature of DMS. The realization regarding the inhomogeneity was challenging because when the inhomogeneity was intentionally changed, the crystalline structure or density of the TM atoms could also be disturbed significantly.

In the previous chapter, the inhomogeneity of ZnO:Co films induced by nitrogen-mediated crystallization (NMC) was investigated, and it was demonstrated that the microstructure and magnetic properties could be finely tuned by this process. In this protocol, ZnO and Co were sputtered in an Ar/N_2 atmosphere, followed by thermal annealing. During deposition, the presence of adsorbed nitrogen atoms perturbed the crystallization of ZnO:Co. Subsequently, post-annealing replaced the nitrogen with oxygen, inducing solid-state crystallization. The size and density of the crystal grains were modulated by the temperature and duration of annealing[12–14]. In addition, post-annealing induced changes in the magnetic properties of ZnO:Co[15–17]. The annealing temperature dependence was investigated, and a critical temperature of 400 °C was identified to lead to the formation of superparamagnetic ZnO:CoN (hereafter referred to as CoN-doped ZnO, as the atomic density of nitrogen is comparable to that of Co). However, there is a lack of understanding regarding the

quantification of nanoscale inhomogeneities and their correlation with magnetic properties.

The primary aim of this study is to propose a quantitative approach for characterizing nanoscale inhomogeneity and to analyze its impact on magnetic properties. This investigation specifically delves into the influence of nanoscale inhomogeneities on ZnO:Co films fabricated via NMC, aiming to elucidate the origins of their paramagnetic behavior. To isolate the effects of nanoscale inhomogeneities on magnetic properties, other structural variations, such as crystal structure and chemical composition, are mitigated among the samples. This is achieved by carefully adjusting the postannealing time to ensure that only this parameter differs across the sample set. Finally, an analytical method is presented to quantify the nanoscale inhomogeneity that is believed to enhance the critical temperature in DMS.

4.2 Methods

ZnO:CoN thin films were fabricated on SiO_2 substrates via radio frequency (RF) magnetron sputtering using a ULVAC MPS system equipped with three cathodes: two for ZnO targets operated at 100 W, and one for Co operated at 50 W. The distance between the cathodes' centers and substrates was set at 70 mm. The deposition process was conducted at room temperature, employing a gas mixture of argon and nitrogen at flow rates of 6.2 and 24.2 sccm, respectively. The substrate rotation speed was maintained at 10 rpm throughout the deposition process. Subsequent to deposition, each film underwent postannealing in ambient air at 400 °C for various durations in order to explore the influence of the annealing process on the structure and magnetic properties of the ZnO:CoN films.

X-ray Diffraction (XRD) analysis was conducted utilizing a Bruker D8 Discover instrument to verify the crystal structure. Magnetic properties were determined using a SQUID magnetometer (Quantum design). To evaluate the composition and nanoscale inhomogeneity within the ZnO:CoN films, X-ray fluorescence (XRF) measurements were performed using a Rigaku Primus II system, while high-resolution transmission electron microscopy (HR-TEM) and energy dispersive X-ray spectroscopy (EDX) were performed with a JEOL-ARM 200F instrument. Additionally, the thickness and surface morphology of the ZnO:CoN films were measured using a Dektak profilometer (Veeco Dektak 150) and atomic force microscopy (AFM, Hitachi 5100N), respectively.

4.3 Results

The total thickness measured using the Dektak profilometer was ~340 nm. The chemical composition of the ZnO:CoN film was confirmed by XRF using the FP method. Fig. 4.1 shows the chemical composition of the ZnO:CoN film at different postannealing times (t_{an}). No significant change was observed in the concentration of any element after annealing for different t_{an}.

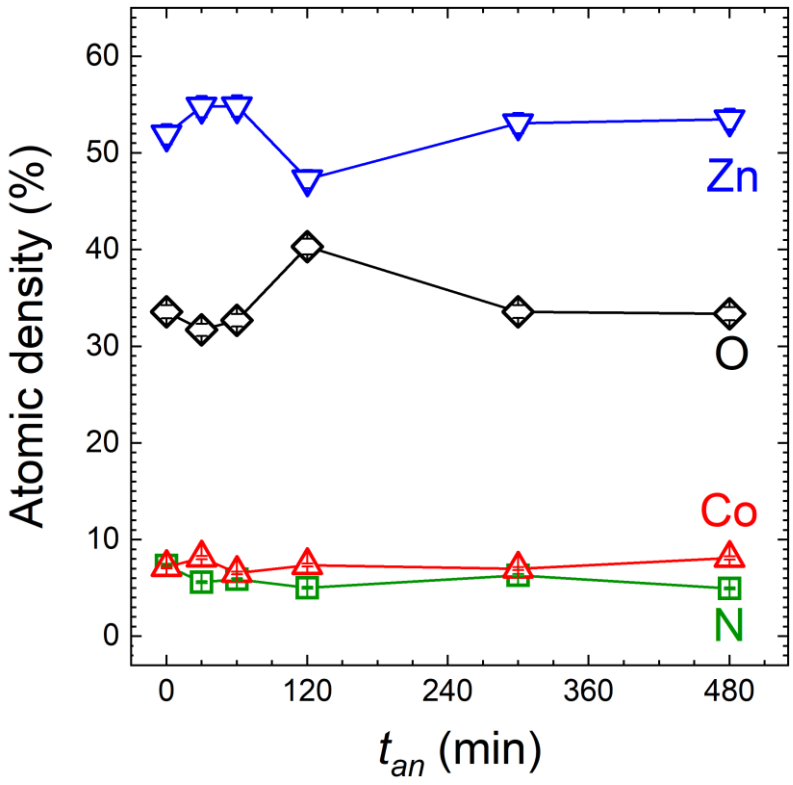

Figure 4.1 Composition of ZnO:CoN films with different post-annealing times.

Figure 4.2a shows the XRD patterns in the range from 30 to 76°. Two peaks from the ZnO (002) and (201) wurtzite structures were observed for all the samples. Their positions did not change (see Figs. 4.2c and 4.2d). Thus, the effect of t_{an} on the lattice constant was not altered by this treatment. Figure 4.2b shows a scaled-up of XRD curve in the 32-51° range. No secondary phases were detected under any conditions. The *M–H* curve was measured at 4 K and is plotted in Fig. 4.3a. Clear hysteresis loops were observed after annealing for more than 30 min. The width of the hysteresis loop, which was characterized by H_c, increased significantly as t_{an} increased (Fig. 4.3a, inset). The height of the hysteresis

loop, which was characterized by the saturation magnetization (M_s), increased slightly. M_s and H_c, as functions of the post-annealing duration are plotted in Fig. 4.3b.

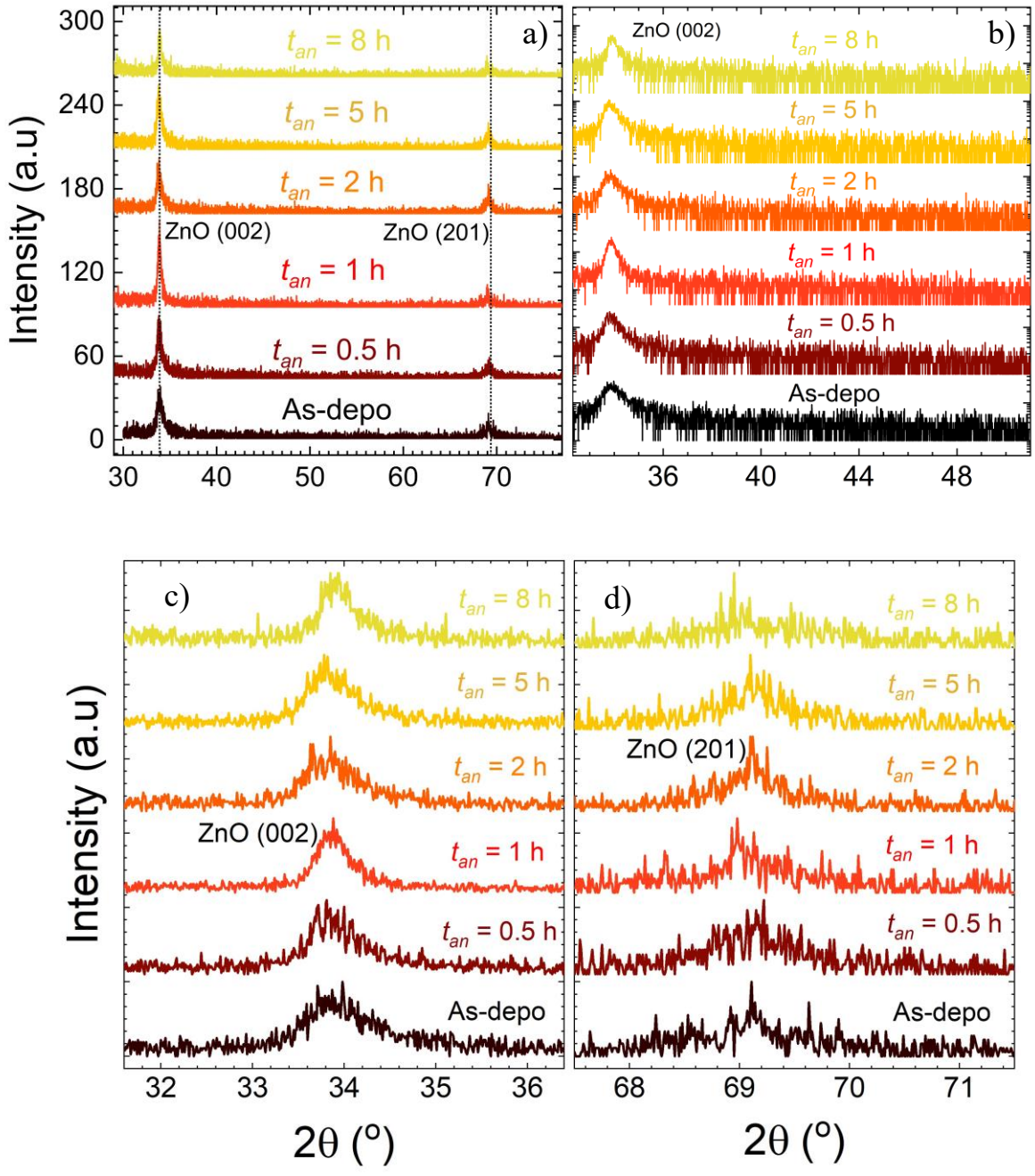

Figure 4.2 XRD pattern for ZnO:CoN films with different post-annealing time. a). Range 30 – 76°, b). 32 – 51°, c). 32 – 36°, and d). 68- 71°.

The obtained H_c value was 40–80 mT and M_s was 29–34 kA/m. These values were higher than that in another report on ZnO:CoN grown by RF magnetron sputtering with

nitrogen [18].

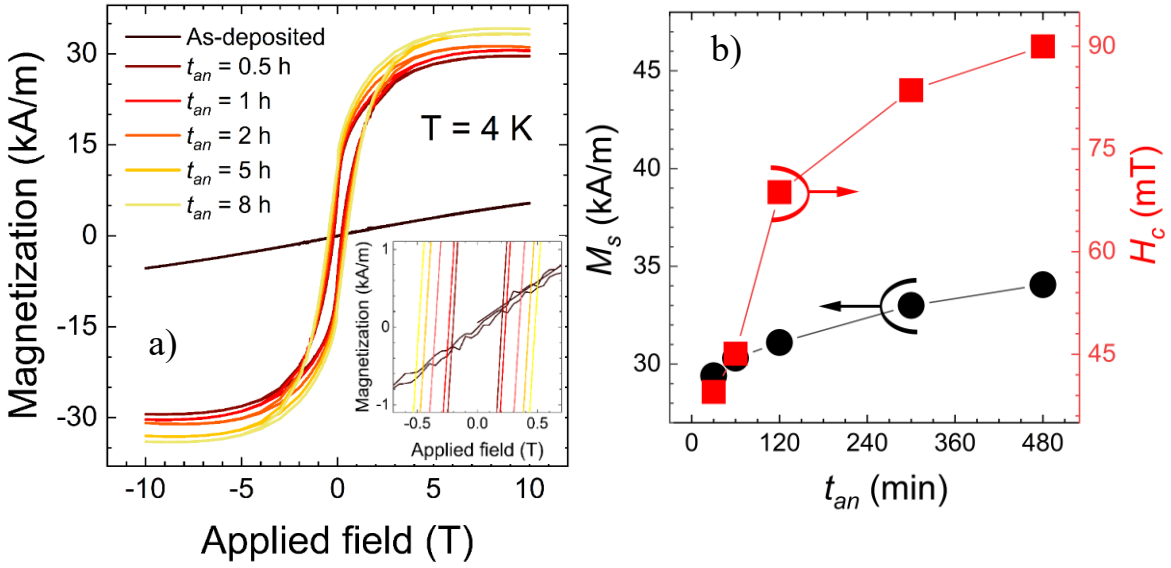

Figure 4.3 a). Dependences of hysteresis loop at 4 K and b). M_s and H_c on postannealing time. Inset shows the low region field.

The temperature-dependent magnetization with the ZFC–FC method is presented in Fig. 4.4a. Except for the as-deposited condition, all ZnO:CoN films showed a similar pattern where the FC curve continued to increase with decreasing temperature, while the ZFC curve reached a clear peak. An enhancement in the T_b and broadening of the ZFC curve were observed with increasing t_{an} (Fig. 4.4b). The obtained T_b was 15–90 K, which was of the same order as that reported by Ney et al.[19] and Opel et al.[20], but lower than that reported by Lee et al.[18].

Because the structure and composition of the ZnO:CoN film did not change largely with annealing time, the change in the distribution of Co atoms, which created inhomogeneities in the nanoscale, was believed to play a crucial role in the enhancement of ferromagnetism in ZnO:CoN. The enhancement in T_b and broadening of the ZFC curve were also the effects of the change in the distribution of Co atoms in the film[21–23]. In the case of the nanocomposite structure, a slight broadening of the size distribution has been known to provide a very broad curve and high T_b in the ZFC curve[24]. Assuming that the Co-rich region forms crystal grains, and that they play a significant role in the magnetic moment in the ZnO:Co films, the size distribution of the crystal grains can be estimated by using the ZFC–FC difference approach[25]:

$$\Delta M_{FC-ZFC} = \frac{M_{FC} - M_{ZFC}}{M_{FC}(T = T_{min}) - M_{ZFC}(T = T_{min})} \tag{4.1}$$

$$\Delta M_{FC-ZFC} = \int_{T}^{\infty} \frac{\mu(T_b)}{\langle \mu \rangle} \cdot \frac{n(T_b)}{N} dT_b \tag{4.2}$$

where μ, n, N, *and* T_{min} are the total magnetic moment, number of particles having T_b, number density of particles, and minimum temperature for the ZFC–FC methods, respectively. Figure 4.5 shows the results of the estimation. The shape of the distribution curve corresponds to the assumption that the NMC and t_{an} enhance the nanoscale inhomogeneity. The peak of the distribution curve of the ZnO:Co film (shown in the black square) is the sharpest and highest among the samples dedicated this study. The peak monotonically gets broader as t_{an} gets longer.

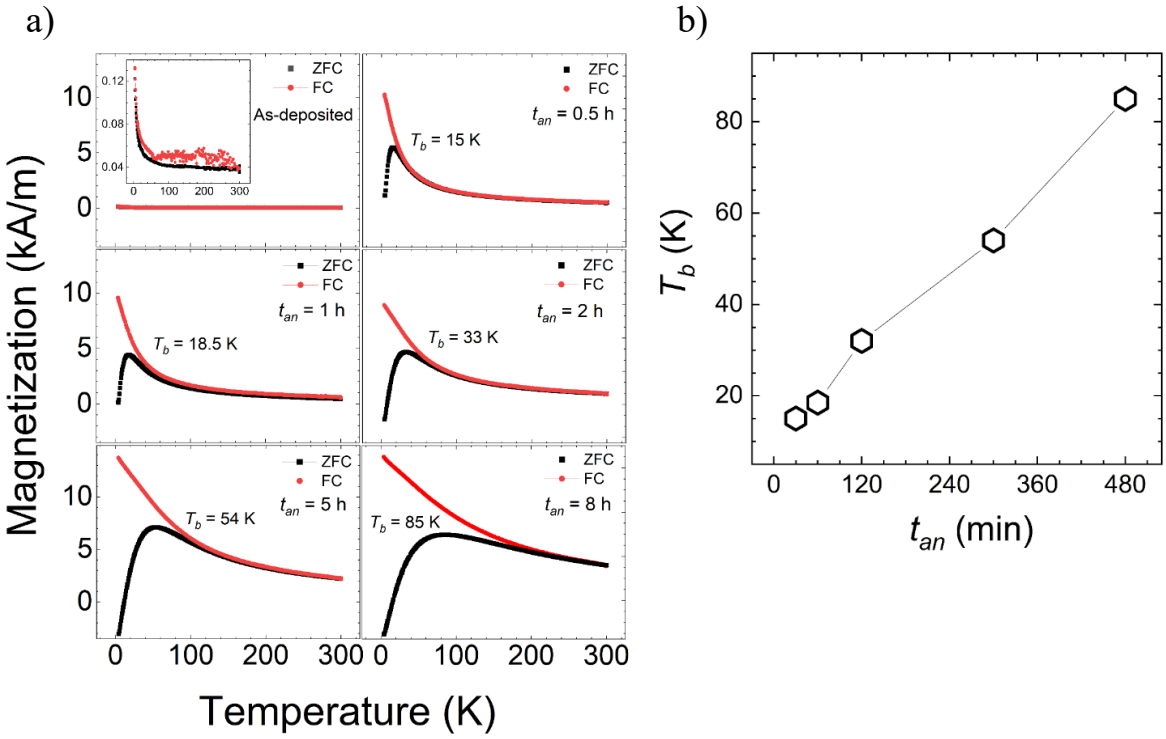

Figure 4.4 a). ZFC–FC curves of ZnO:CoN films with different postannealing times in range of 4–300 K. The inset shows the low-magnetization region. b). Dependence of T_b on postannealing time of ZnO:CoN films.

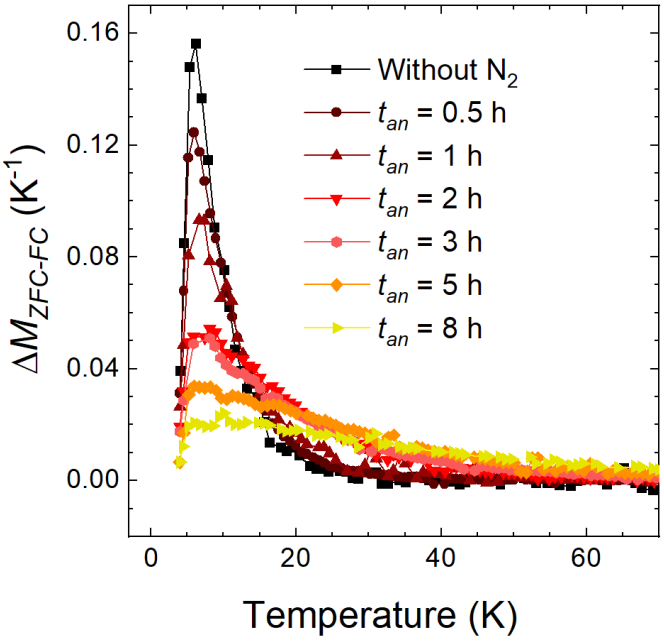

Figure 4.5 Distribution of Co in ZnO:CoN films with different postannealing times, approached by the difference in ZFC–FC.

The effect of nanoscale inhomogeneity on the surface morphology profiles of the as-deposited film and films with a t_{an} of 3, 5, and 8 h was evaluated by AFM for scan size of $5 \times 5\ \mu m^2$ and $2 \times 2\ \mu m^2$, as shown in Fig. 4.6.

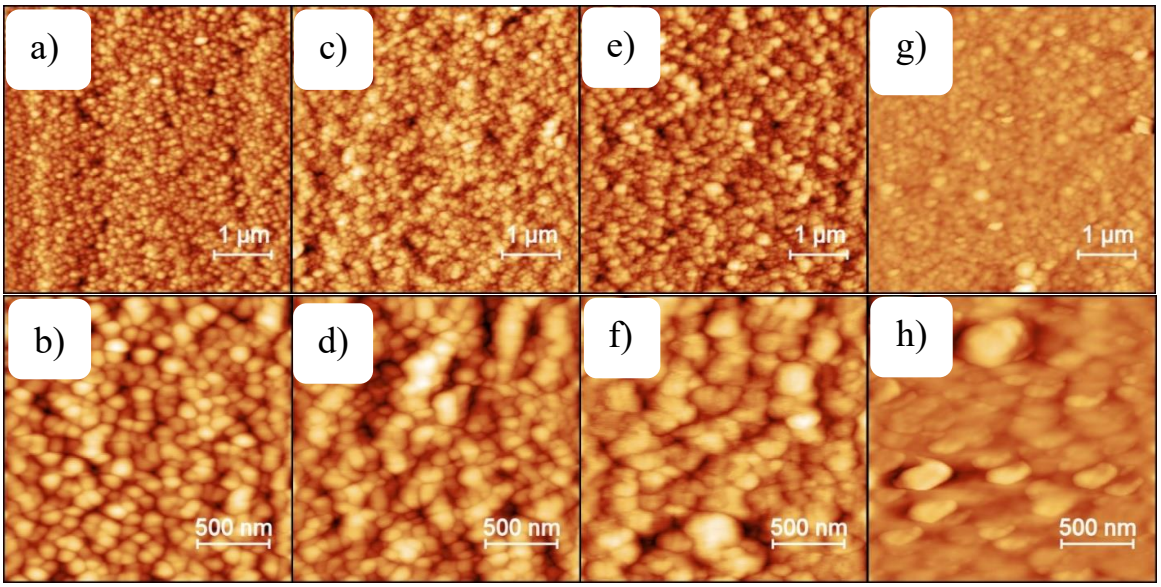

Figure 4.6 Surface profiles of ZnO:CoN films for different post-annealing times. (a–b), (c–d), (e–f), (g–h). for t_{an} of 0, 3, 5, and 8 h, respectively

The variation in grain sizes and roughness was analyzed through surface-morphology observations. In the as-deposited state, distinct grain boundaries were evident on the surface, with an average grain size of 113.7 nm and root mean square (RMS) roughness of 2.5 nm. As the annealing temperature increased, the grain boundaries began to coalesce, forming larger islands. Consequently, the grain size increased to 134.9, 223.5, and 252.3 nm. Correspondingly, the surface roughness also increased, reaching RMS values of 3.7, 4.4, and 5 nm, respectively. These findings confirmed that nanoscale inhomogeneities significantly influenced the surface morphology of the film.

Cross-sectional HR-TEM was performed to investigate the structural properties of ZnO:CoN for the as-deposited films and film with a post-annealing time t_{an} of 8 h. The stripe pattern observed in all films as displayed in Fig. 4.7 resulted from the interference between the different crystal lattices or periodic structures within the ZnO:CoN film, known as Moiré fringes[26,27].

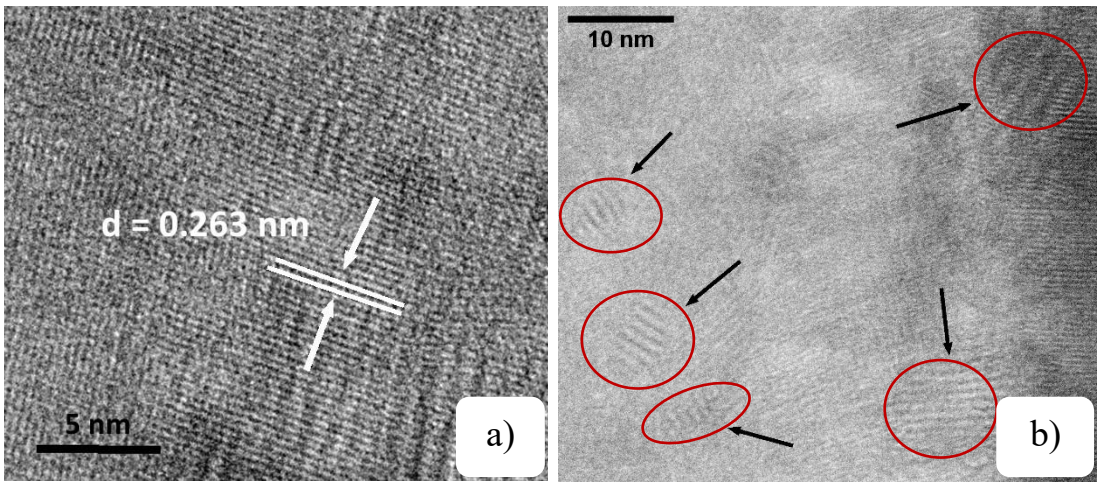

Figure 4.7 Cross-section HR-TEM profile of ZnO:CoN films for a). as-deposited film and b). film with t_{an} of 8 h.

When applying the inverse Fourier transform, the as-deposited ZnO:CoN film presented a relatively homogeneous stripe with an interplanar distance of 0.263 nm. This value agreed with the Bragg's law calculations derived from the XRD pattern, which indicated an interplanar distance in the (002) plane and was consistent with the results in another report[4]. Homogeneous stripe patterns on ZnO:CoN were also reported by Martinez et al.[28] and Ney et al.[29]. Variations in the stripe patterns, such as in the stripe direction and interplanar distance, were observed in the ZnO:CoN film with a t_{an} of 8 h. As reported by

other groups, various stripes can be induced by nanosized Co distributions[30–33]. Moreover, other groups have reported that various stripes appear when the Co density in ZnO (ρ_{Co}) > 25%. In our case, $\rho_{Co} \leq 15\%$. The presence of various striped patterns in the ZnO:CoN films with ρ_{Co} less than the solubility limit confirmed that the post-annealing treatment of ZnO:CoN films containing nitrogen resulted in an inhomogeneous dispersion of the Co density, leading to the formation of nanoscale inhomogeneities in the films. Thus, all the experimental results are consistent, based on the distribution curve estimation.

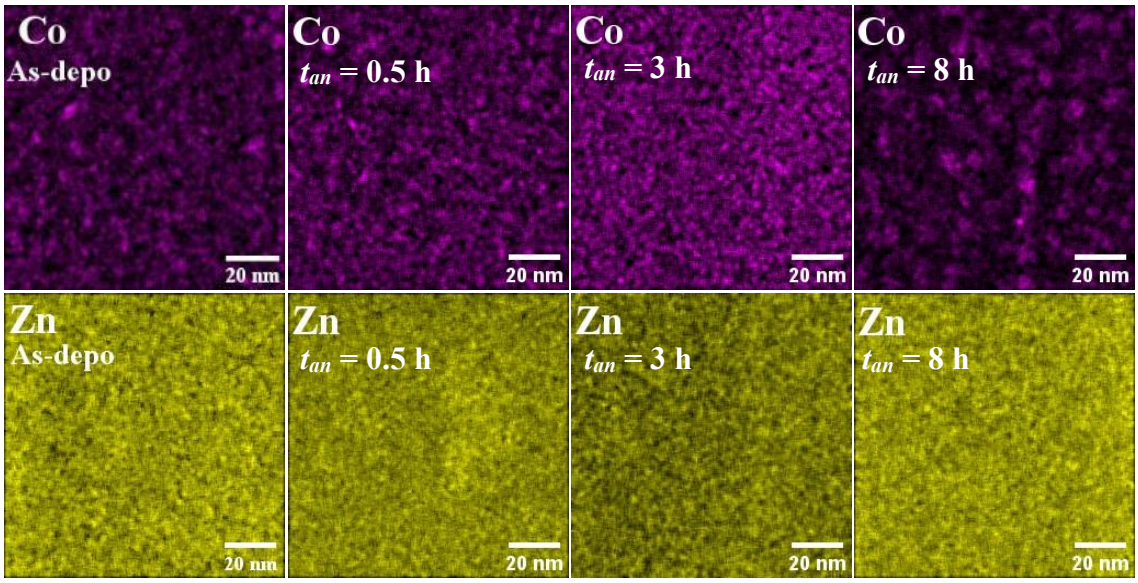

Figure 4.8 EDX results of ZnO:CoN films with different post-annealing times.

However, our ZnO:Co and ZnO:Co samples do not consist of nanocomposites or nanoparticles because they are thin films fabricated by sputtering. The validity of this estimation will be examined by implementing another method to characterize the nanoscale inhomogeneities in the sputtered films. To verify the distribution of ρ_{Co}, EDX measurements were performed on four of the ZnO:CoN samples (t_{an} of 0, 0.5, 3, and 8 h), which are presented in Fig. 4.8. Thus, the density distributions of the Co and Zn atoms were visualized in nanometer resolutions. The modification of the nanoscale inhomogeneity was observable; the distinct changes were observed in the distribution of Co and Zn atoms among different t_{an}. To quantify the distribution of ρ_{Co} and its inhomogeneity, the normalized intensity of Co was calculated using $\rho_{Co}/[\rho_{Co}+\rho_{Zn}]$, where ρ_{Zn} was the density of Zn, and the histogram was plotted as shown in Fig. 4.9a. The curve fitting was performed assuming the following

Gaussian distribution function:

$$f(\rho_{Co}) = \frac{1}{\sigma\sqrt{2\pi}} e^{-\frac{1}{2}\left(\frac{\rho_{Co}-\overline{\rho_{Co}}}{\sigma}\right)} \quad (4.3)$$

where, f(ρ_{Co}), ($\overline{\rho_{Co}}$), and σ are the distribution function, mean, and standard deviation of the Co density on Zn, respectively. The fitting curve reproduced the histogram of all samples quite nicely with an R-squared value of ~0.98. The investigation focused on σ, which represented the variation in the distribution function, as the measure of the nanoscale inhomogeneity, and discovered the monotonic increase in σ based on t_{an} (Fig. 4.9b). The broadening of the distribution curve was direct quantitative evidence for the fact that NMC dispersed the density of Co atoms in ZnO:CoN, which enhanced M_s, H_c, and T_b.

The possibility of the precipitation of metallic Co phases as the origin of ferromagnetism was refused based on this Gaussian fitting analysis. Two different scenarios were considered: the Co precipitates where $\rho_{Co}/[\rho_{Co}+\rho_{Zn}]$ was more than the solubility limit (0.25) and more than the average (0.13 based on XRF). The blue and red shaded areas in Fig. 4.9a represent the integrated distribution function in the range of $\rho_{Co}/[\rho_{Co}+\rho_{Zn}]$ greater than 0.25 (A_{25}) and that between 0.13 and 0.25. The sum of the red and the blue areas represents the integrated distribution function in the range of $\rho_{Co}/[\rho_{Co}+\rho_{Zn}]$ more than 0.13 (A_{13}). If the precipitated Co is dominant to the magnetic moment in ZnO:CoN, the trend of the t_{an} dependence of the M_s will be similar to that of A_{25} or A_{13}, as M_s increases significantly when Co clusters or secondary phases are present[30–33]. Figure 4.9c shows the dependence of A_{25} and A_{13} on t_{an}. As t_{an} increases, A_{25} gradually increases and reaches more than 500% of the original value after 480 min. A_{13} also increases after annealing, during the first 30 min, slightly decreases after 180 min, and reaches more than 25% of the original value finally. Thus, both trends are largely different from the t_{an} dependence of M_s, which increases by less than 10% after annealing for 480 min (black circles in Fig. 4.3b). This quantitative analysis refutes the possibility of the precipitation of Co clusters in ZnO:CoN, which is consistent with the XRD and the XPS (previous chapter) results. Thus, it was concluded that the magnetic moment stems from ZnO:CoN and that the significant increase in T_b was attributed to the nanoscale inhomogeneity.

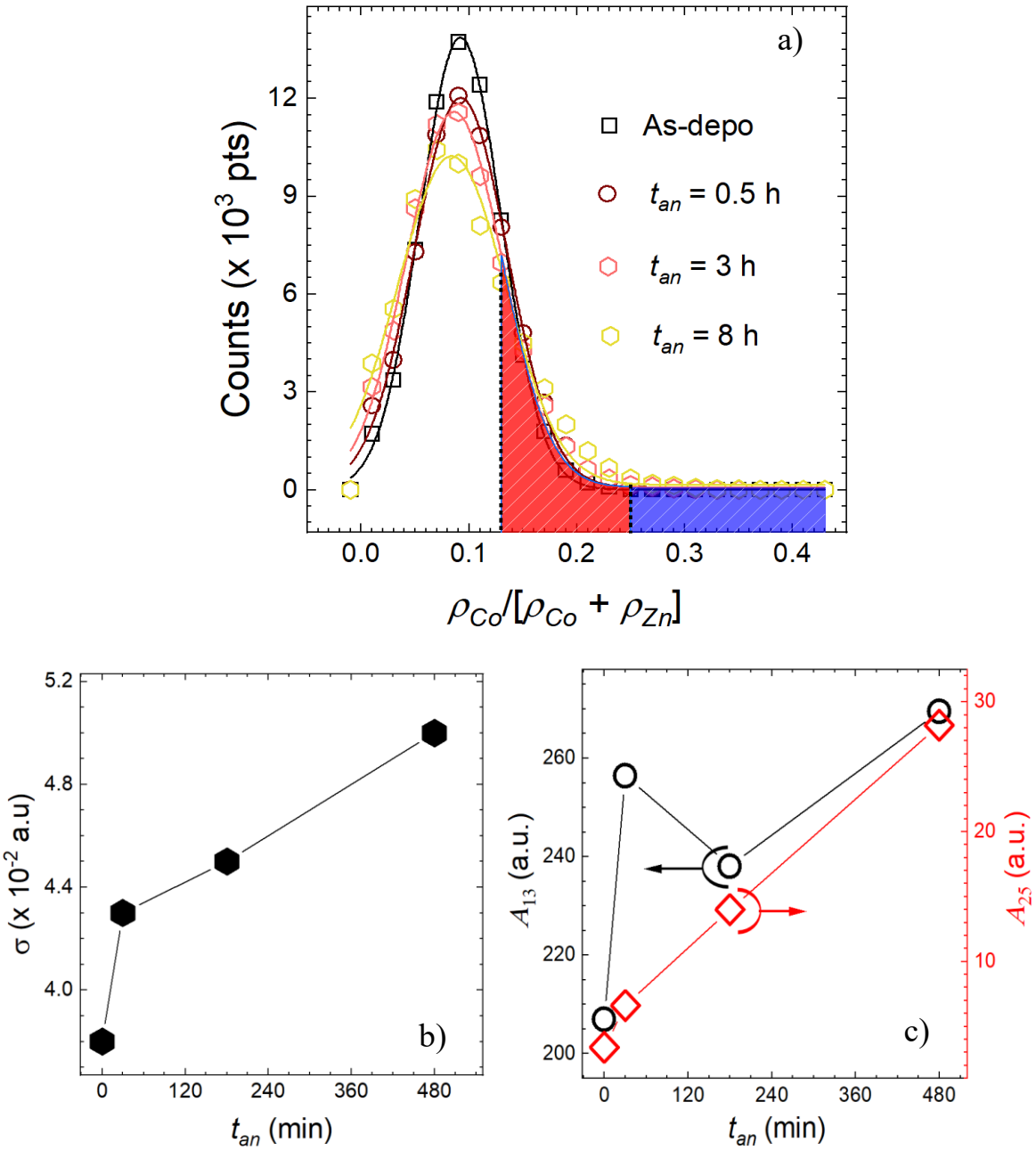

Figure 4.9 Histogram of ρ_{Co} in ZnO:Co with various postannealing times. b). Standard deviation as a function of postannealing time. c). Dependences of shaded area at ρ_{Co} > 13% (red and blue) and > 25% (blue).

4.4 Conclusion

The effects of the postannealing time on the T_b and H_c of ZnO:Co films fabricated using the NMC method were investigated. It was observed that Co was incorporated into the wurtzite structure with a preferred orientation (002) and the blocking temperature was higher than that of ZnO:Co without nitrogen. The observed shift of the (002) peak indicated that the addition of nitrogen during deposition had disrupted the crystallization of the ZnO structure without secondary phases and created defects to form nanoscale inhomogeneity in the ZnO:Co film, which contributed to ferromagnetic properties. The coercivity and blocking temperature increased with increasing postannealing duration, without altering the wurtzite structure or chemical composition, suggesting that the postannealing changed the distribution of Co atoms in the film. The assumption that NMC induced the nanoscale inhomogeneity that largely enhanced H_c and T_b was corroborated based on two different quantitative analyses: the ZFC–FC difference approach and EDX approach. A new method to analyze the nanoscale inhomogeneity from EDX was demonstrated, which provided a direct measure of the inhomogeneity based on statistics. A Gaussian distribution function reproduced the distribution of the $\rho_{Co}/[\rho_{Co}+\rho_{Zn}]$ well and allowed detailed discussion of the origin of the magnetic moment. This result suggested a useful method to characterize the nanoscale inhomogeneity in solids and paved a new way to achieve a deeper understanding of DMS.

References

1. T. Dietl, H. Ohno, F. Matsukura, J. Cibert, D. Ferrand, *Science (80-.).* **287**, 1019–1022 (2000).
2. M. Shatnawi, A. M. Alsmadi, I. Bsoul, B. Salameh, G. A. Alna'Washi, F. Al-Dweri, F. El Akkad, *J. Alloys Compd.* **655**, 244–252 (2016).
3. M. Ivill, S. J. Pearton, S. Rawal, L. Leu, P. Sadik, R. Das, A. F. Hebard, M. Chisholm, J. D. Budai, D. P. Norton, *New J. Phys.* **10** (2008), doi:10.1088/1367-2630/10/6/065002.
4. R. Siddheswaran, R. Medlín, C. E. Jeyanthi, S. G. Raj, R. V. Mangalaraja, *Appl. Phys. A Mater. Sci. Process.* **125**, 1–9 (2019).
5. T. J. Castro, P. A. M. Rodrigues, A. C. Oliveira, F. Nakagomi, J. Mantilla, J. A. H. Coaquira, A. Franco, H. V. S. Pessoni, P. C. Morais, S. W. Da Silva, *J. Appl. Phys.* **121** (2017), doi:10.1063/1.4973526.
6. B. Huang, D. Zhu, X. Ma, *Appl. Surf. Sci.* **253**, 6892–6895 (2007).
7. H. S. Hsu, J. C. A. Huang, Y. H. Huang, Y. F. Liao, M. Z. Lin, C. H. Lee, J. F. Lee, S. F. Chen, L. Y. Lai, C. P. Liu, *Appl. Phys. Lett.* **88** (2006), doi:10.1063/1.2212277.
8. A. Simimol, A. A. Anappara, S. Greulich-Weber, P. Chowdhury, H. C. Barshilia, *J. Appl. Phys.* **117** (2015), doi:10.1063/1.4922050.
9. M. P. F. de Godoy, X. Gratens, V. A. Chitta, A. Mesquita, M. M. de Lima, A. Cantarero, G. Rahman, J. M. Morbec, H. B. de Carvalho, *J. Alloys Compd.* **859**, 157772 (2021).
10. L. R. Shah, H. Zhu, W. G. Wang, B. Ali, T. Zhu, X. Fan, Y. Q. Song, Q. Y. Wen, H. W. Zhang, S. I. Shah, J. Q. Xiao, *J. Phys. D. Appl. Phys.* **43** (2010), doi:10.1088/0022-3727/43/3/035002.
11. A. Chakraborty, R. Bouzerar, S. Kettemann, G. Bouzerar, *Phys. Rev. B - Condens. Matter Mater. Phys.* **85**, 1–7 (2012).
12. K. Kuwahara, N. Itagaki, K. Nakahara, D. Yamashita, G. Uchida, K. Kamataki, K. Koga, M. Shiratani, *Thin Solid Films*. **520**, 4674–4677 (2012).
13. N. Itagaki, K. Kuwahara, K. Matsushima, D. Yamashita, H. Seo, K. Koga, M. Shiratani, *Opt. Eng.* **53**, 087109 (2014).
14. I. Suhariadi, N. Itagaki, M. Shiratani, *ACS Appl. Nano Mater.* **3**, 2480–2490 (2020).

15. H. Ren, G. Xiang, G. Gu, X. Zhang, *Mater. Lett.* **122**, 256–260 (2014).
16. Z. L. Lu, X. F. Bian, W. Q. Zou, M. X. Xu, F. M. Zhang, *J. Alloys Compd.* **492**, 31–34 (2010).
17. S. Aksu, E. Bacaksiz, S. Ylmaz, I. Polat, M. Altunbaş, M. Türksoy, R. Topkaya, K. Özdogan, *Phys. E Low-Dimensional Syst. Nanostructures*. **44**, 1244–1249 (2012).
18. Y. Lee, J. C. Lee, C. W. Su, *IEEE Trans. Magn.* **46**, 1565–1568 (2010).
19. V. Ney, V. Venkataraman, B. Henne, K. Ollefs, F. Wilhelm, A. Rogalev, A. Ney, *J. Appl. Phys.* **119** (2016), doi:10.1063/1.4947455.
20. M. Opel, K. W. Nielsen, S. Bauer, S. T. B. Goennenwein, J. C. Cezar, D. Schmeisser, J. Simon, W. Mader, R. Gross, *Eur. Phys. J. B.* **63**, 437–444 (2008).
21. S. K. Mandal, A. K. Das, T. K. Nath, D. Karmakar, B. Satpati, *J. Appl. Phys.* **100** (2006), doi:10.1063/1.2360387.
22. M. M. Eltabey, A. M. Massoud, C. Radu, *Mater. Chem. Phys.* **186**, 505–512 (2017).
23. T. Wen, K. M. Krishnan, *J. Phys. D. Appl. Phys.* **44** (2011), doi:10.1088/0022-3727/44/39/393001.
24. L. G. Jacobsohn, M. F. Hundley, J. D. Thompson, R. M. Dickerson, M. Nastasi, *J. Vac. Sci. Technol. B Microelectron. Nanom. Struct. Process. Meas. Phenom.* **24**, 321–325 (2006).
25. H. Mamiya, M. Ohnuma, I. Nakatani, T. Furubayashim, *IEEE Trans. Magn.* **41**, 3394–3396 (2005).
26. S. Amelinck, J. Van Landuyt, in *Transmission Electron Microscopy* (2012), pp. 493–538.
27. R. K. Khurana, **140** (2022).
28. B. Martínez, F. Sandiumenge, L. Balcells, J. Arbiol, F. Sibieude, C. Monty, *Phys. Rev. B - Condens. Matter Mater. Phys.* **72**, 1–8 (2005).
29. A. Ney, A. Kovács, V. Ney, S. Ye, K. Ollefs, T. Kammermeier, F. Wilhelm, A. Rogalev, R. E. Dunin-Borkowski, *New J. Phys.* **13** (2011), doi:10.1088/1367-2630/13/10/103001.
30. M. Tay, Y. Wu, G. C. Han, T. Chong, Y. K. Zheng, S. J. Wang, Y. Chen, X. Pan, *J. Appl. Phys.* **100** (2006), doi:10.1063/1.2348632.
31. L. C. Nistor, C. Ghica, V. Kuncser, D. Pantelica, J. J. Grob, G. Epurescu, M. Dinescu,

J. Phys. D. Appl. Phys. **46** (2013), doi:10.1088/0022-3727/46/6/065003.

32. N. Jedrecy, H. J. Von Bardeleben, D. Demaille, *Phys. Rev. B - Condens. Matter Mater. Phys.* **80**, 1–6 (2009).

33. N. Jedrecy, M. Hamieh, C. Hebert, J. Perriere, *Nanoscale*. **9**, 10431–10439 (2017).

Chapter 5

The Growth of $Tm_3Fe_5O_{12}$ Film with Perpendicular Magnetic Anisotropy by On-axis Sputtering

5.1 Introduction

Rare-earth iron garnets have attracted considerable interest in spintronics due to their unique ferrimagnetic insulating properties, which facilitate the long-range propagation of spin waves[1–3]. By exploiting the spin-orbit torque to manipulate the magnetic moment[3], these materials are being explored as candidates for energy-efficient magnetic memory and logic devices[4]. In addition, their low magnetic damping constant holds promise for the realization of domain-wall qubits[5,6]. The perpendicular magnetic anisotropy (PMA), along with the weak magnetic moment resulting from compensated ferrimagnetism, is advantageous for integrated system applications[7–11].

Recently, thulium iron garnet ($Tm_3Fe_5O_{12}$, TmIG), a member of the rare-earth iron garnet family, has received considerable attention for its PMA. TmIG exhibits a remarkably large negative magnetostriction constant of λ_{111} = -5.2 × 10^{-6}. When deposited on a gadolinium gallium garnet ($Gd_3Ga_5O_{12}$, GGG) (111) substrate, it experiences a strain of 0.49%, inducing a sufficiently large PMA to overcome the shape anisotropy[7,12]. The observation of spin-orbit torque (SOT) switching[3,8] and skyrmion transport[11,13] on TmIG multilayers, such as Pt/TmIG/GGG, demonstrates the potential for achieving high-efficiency magnetization switching and ultrafast chiral domain motion. Skyrmions are emerging as promising carriers owing to their topologically stable nanoscale spin structures controllable at ultralow current densities[14,15]. The interfacial Dzyaloshinskii–Moriya interaction (DMI) properties of TmIG multilayers, which stabilize the domain walls and skyrmions, have been successfully identified using the emerging topological Hall effect[13,16–20]. In addition, TmIG exhibits ferrimagnetic insulating properties conducive to long-range spin-wave propagation[21]. The prominence of TmIG as a spin-orbitronic and skyrmionic material is driving research toward the development of memory and logic devices[4,22–24].

Fabrication of TmIG films has been reported using pulsed laser deposition (PLD)[25–27] and off-axis sputtering[12,28,29]. The sputtering method offers advantages over PLD for large-scale fabrication, such as mitigating size limitations on the film area and overcoming issues such as particle coalescence and nonuniform deposition that affect the fabrication of multilayer structures[30–32]. On-axis sputtering, which is commonly used to grow oxide thin films on a large scale, is suitable for industrial-scale fabrication[33]. However, there is a lack of research on the fabrication of TmIG films using on-axis sputtering. This report presents

the fabrication of TmIG films with PMA properties using on-axis sputtering followed by post-annealing treatment.

5.2 Methods

TmIG films were grown epitaxially on GGG (111) substrates by radio-frequency (RF) magnetron sputtering using an on-axis geometry configuration. The optimal growth conditions were determined by systematically adjusting the Tm/Fe ratio at position A on silicon substrates (Fig. 5.1a), different pressures (0.35 Pa, 1 Pa, 10 Pa), and oxygen (O_2) flow ratios (R_o = 0%, 22%, 36% at 1 Pa), where R_o is defined as $O_2/(O_2 + Ar) \times 100\%$. Fig. 5.1b shows the arrangement of the substrate holder and TmIG target, with the red cross indicating their intersection. The distances L_A = 64 mm, L_B = 93 mm, and L_C = 98 mm indicate the distances between the target and each substrate. The angles α, β, and γ, which are measured relative to line L, respectively correspond to 15, 36, and 39°, respectively.

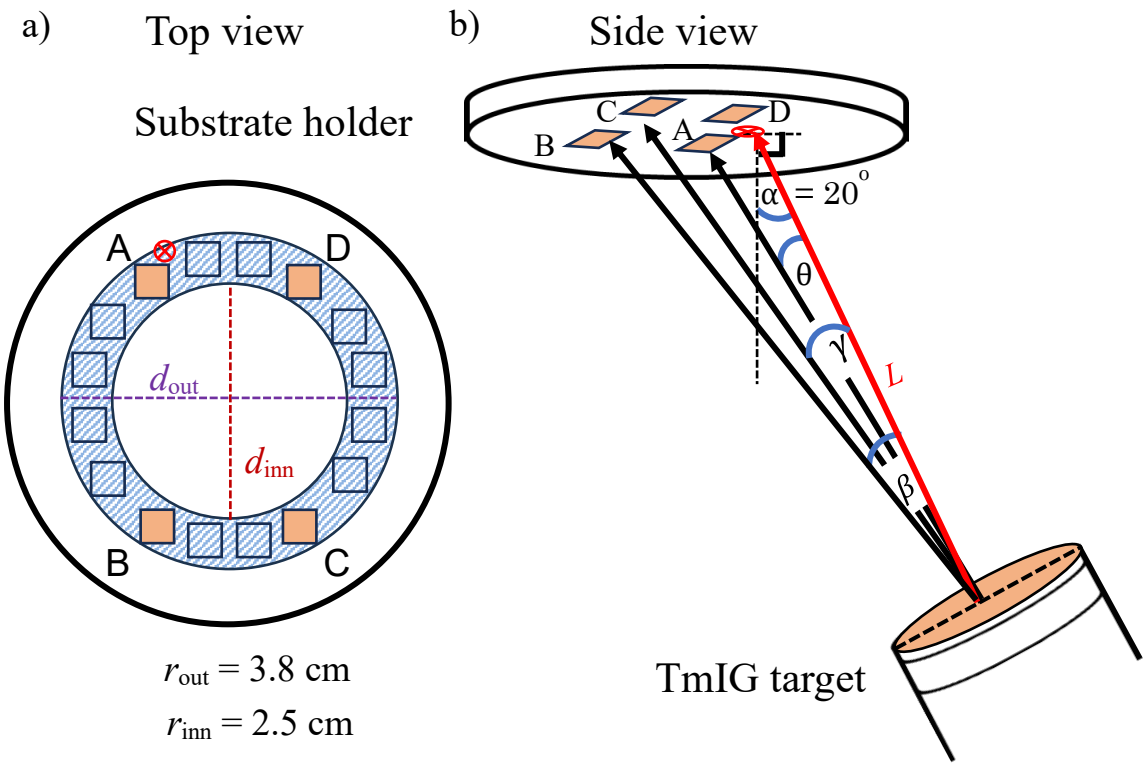

Figure 5.1 Geometric position of substrate holder and TmIG target in sputtering chamber. a). Top view and b). side view.

The film composition was evaluated by X-ray fluorescence (XRF) analysis using a Rigaku ZSX Primus II instrument. Clear peak spectra were observed for the Fe and Tm elements (Fig. 5.2a-d), and the Tm/Fe ratios were determined using the fundamental parameter (FP) method built into the XRF system (Fig. 5.2e–f). The analysis showed that a Tm/Fe ratio close to stoichiometry (0.6) was obtained at a R_o of 22% and pressure of 1 Pa.

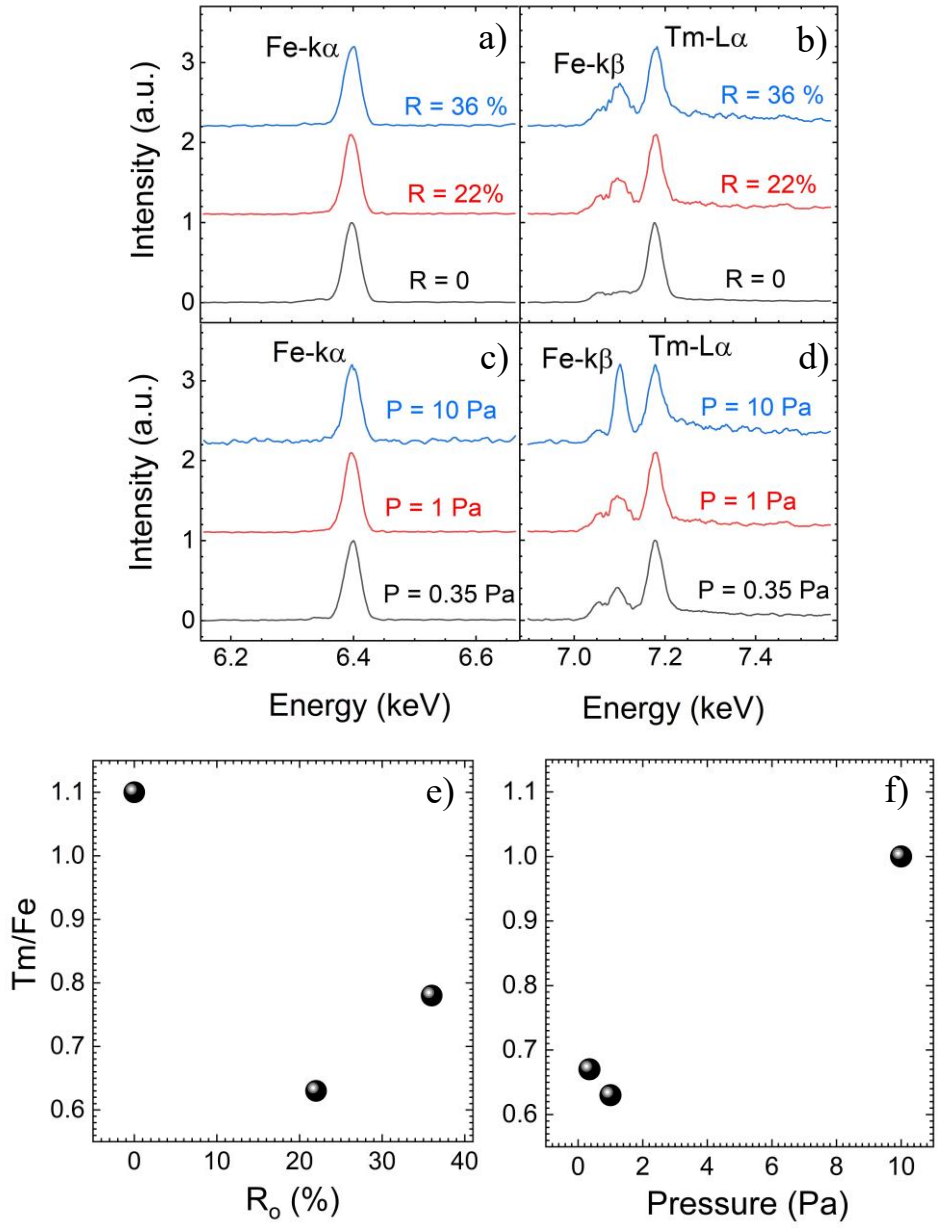

Figure 5.2 Chemical composition of TmIG films. (a–b). XRF spectra with different ratios of oxygen flow rates, (c–d). XRF spectra with different of pressures, and (e-f). Tm/Fe ratio of TmIG films with different R_o and pressures.

Subsequently, TmIG films were deposited on GGG substrates by RF magnetron sputtering with on-axis geometry using two methods, without rotation and with a substrate holder rotation at 10 rpm.

GGG substrates of 1 × 1 cm^2 were placed at three positions (A, B, and C) for no rotation and four positions (A, B, C, and D) for rotation, maintaining the same deposition area with a radius of 3 cm from the central substrate holder, as shown in Figure 1a. The deposition was performed at an RF power of 60 W, with Ar and O_2 supplied at rates of 18 and 5 sccm, respectively. After sputter deposition, post-annealing (T_{an}) was performed at 800 °C for 3 h in an O_2 atmosphere at ambient pressure. In the absence of rotation, deposition was conducted at different thicknesses (6, 18, 24, and 30 nm) to investigate the relationship between X-ray diffraction (XRD) peak intensity and TmIG magnetization as a function of film thickness. Rotation was performed in an O_2 environment at T_{an} of 650, 800, and 950 °C for each film.

The structural investigation of TmIG involved the use of advanced techniques such as high-resolution XRD 2θ–ω scans using Cu Kα radiation (λ = 1.5406 Å) and X-ray reflectivity (XRR) measurements using by a Bruker D8 Discover instrument. To characterize the magnetic properties, a superconducting quantum interference device (SQUID) magnetometer (Quantum Design, MPMS3) was used for direct current (DC) scans at 300 K, while ferromagnetic resonance (FMR) measurements were performed using an electron spin resonance system (Bruker EMX). Films of 4 mm × 2 mm were mounted on quartz rods and exposed to microwave irradiation at a frequency of 9.6 GHz and power of 2.1 mW. Angle-dependent measurements were conducted by systematically altering the angle between the external magnetic field and substrate normal. DC magnetic field scans were executed at each orientation to capture comprehensive data. The magnetic domain structure was visualized using a Kerr microscope (Evico microscope), while the analysis of the labyrinth domain structure at zero field was performed following an alternating current (AC) demagnetization procedure[34]. The surface film morphology was analyzed by employing an atomic force microscope (AFM), specifically, the Hitachi AFM5100N model.

5.3 Results

5.1. *Fabrication of $Tm_3Fe_5O_{12}$ Film with PMA by On-axis Sputtering*

XRD was performed to confirm the crystalline formation of TmIG. Figure 5.3a displays the outcomes of XRD 2θ scans conducted on films deposited at position A with varying thicknesses (18, 24, and 30 nm), followed by postannealing. Each film exhibited a characteristic peak at 51.55°, corresponding to TmIG (444), alongside the substrate peak observed at 51.06°. The consistent presence of this peak, as observed in a previous study[7,12], indicated that the TmIG film maintained uniform lattice strain, a characteristic favorable for perpendicular magnetic anisotropy (PMA). These XRD patterns confirmed the efficacy of the on-axis sputtering for fabricating TmIG films. Notably, the intensity of the TmIG peak increased with longer deposition times at position A.

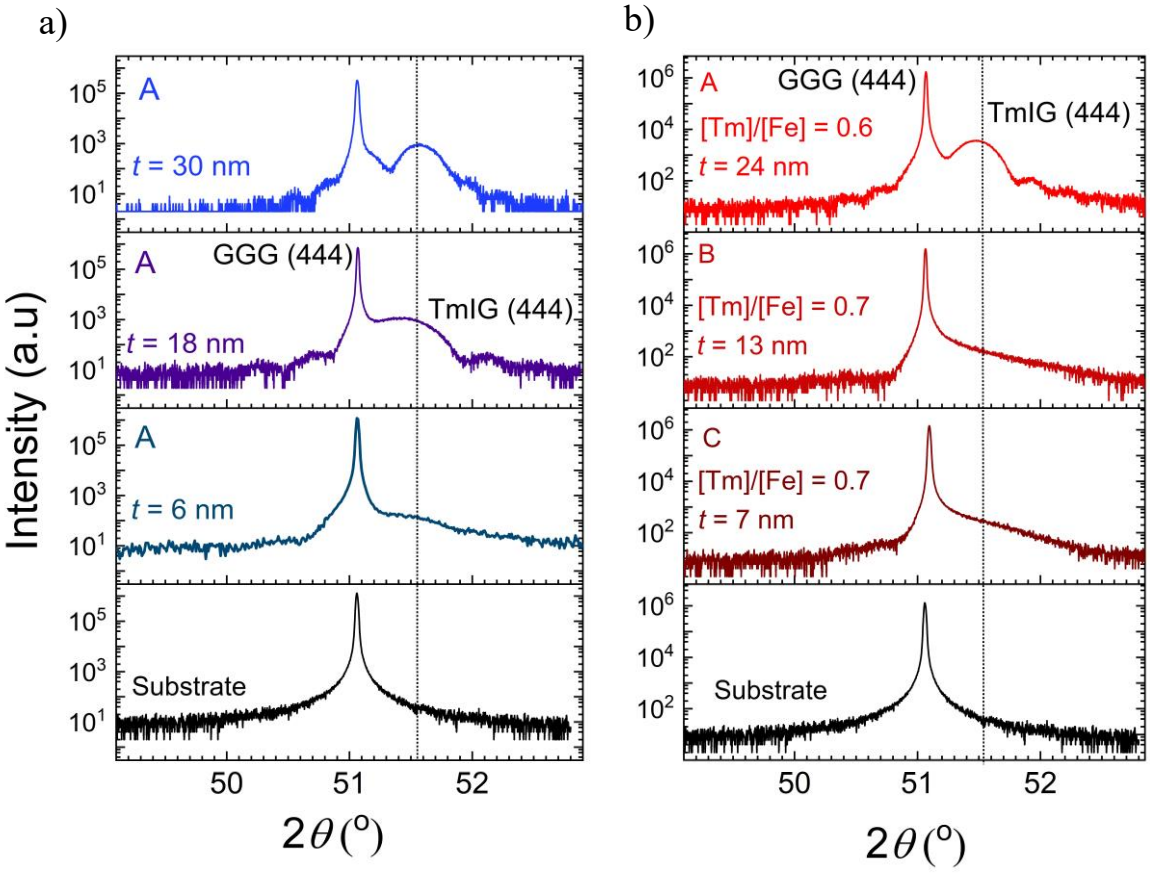

Figure 5.3 XRD patterns of TmIG films. a). Different thickness and b). different position

To investigate the effect of position on the TmIG film, three films were grown under identical conditions, with a film thickness of 24 nm, as shown in Figure 5.3b. Interestingly, a detectable TmIG (444) peak was observed only in one film deposited at position A. In addition, the TmIG film thickness, denoted *t*, varied with position as determined by XRR. Specifically, the thicknesses measured at positions A, B, and C were 24, 13, and 7 nm, respectively. The finding that the thickness (*t*) of the film deposited at position B exceeded that of a thinner film (*t* = 6 nm) deposited at position A suggests that TmIG attainment is not solely dependent on the film volume. It is further influenced by chemical factors, as evidenced by the atomic density measurements performed using XRF.

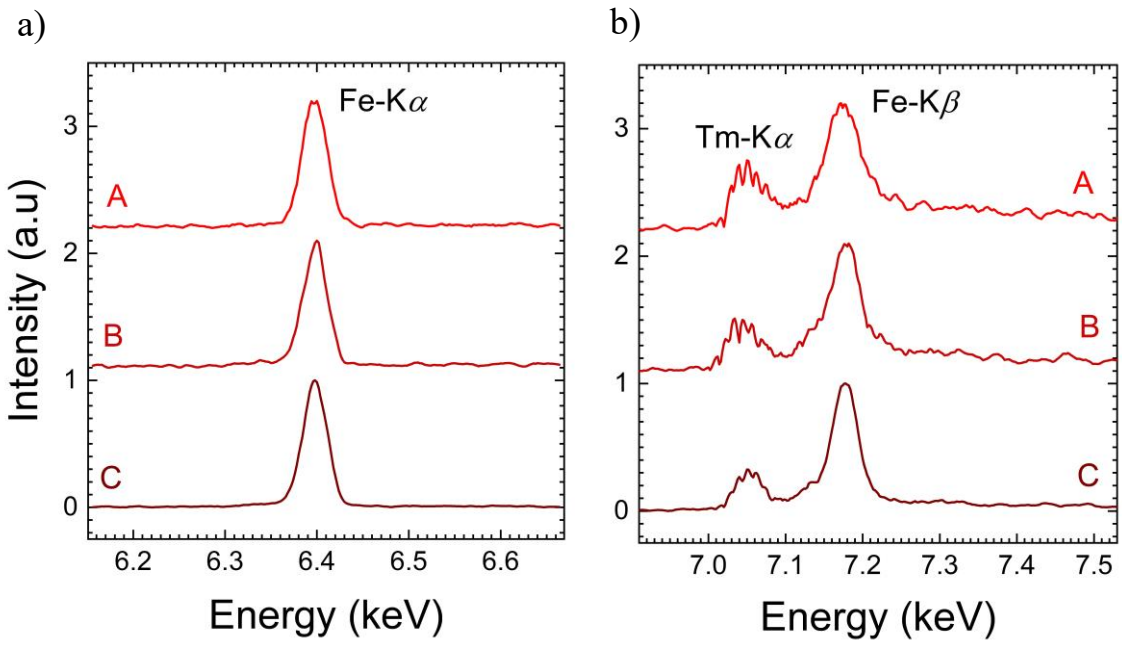

Figure 5.4 XRF curves of TmIG films. a). Fe and b). Tm

The results depicted in Fig. 5.4 present the XRF analysis outcomes. Densities of Tm and Fe were analyzed from the XRF spectra using the analytical software integrated with our XRF system (ZSX Primus II, Rigaku) using the FP method[35]. Evident peaks were discernible within each spectrum. The [Tm]/[Fe] ratio was found to be 0.6 (stoichiometric) for the film grown at position A, while it was 0.7 for the films grown at positions B and C (as illustrated in Fig. 5.4b). To clarify the disparity in the dispersion of sputtered Fe and Tm, a Transportation of Ion in Materials (TRIM) simulation was conducted. The composition concerning the substrate position is delineated alongside the TRIM simulation findings in

Fig. 5.5. The kinetic energy derived from argon was set to either 100 eV or 150 eV, but there was no noticeable distinction between these two conditions. The number of atoms sputtered from the target was quantified at 55 million instances. For each sputtered atom, the spreading angle (φ) was determined. To evaluate the Tm/Fe ratio, histograms were constructed showing the distributions of the spreading angles (ϕ) for both Fe and Tm. A clear positive correlation existed between ϕ and the [Tm]/[Fe] ratio.

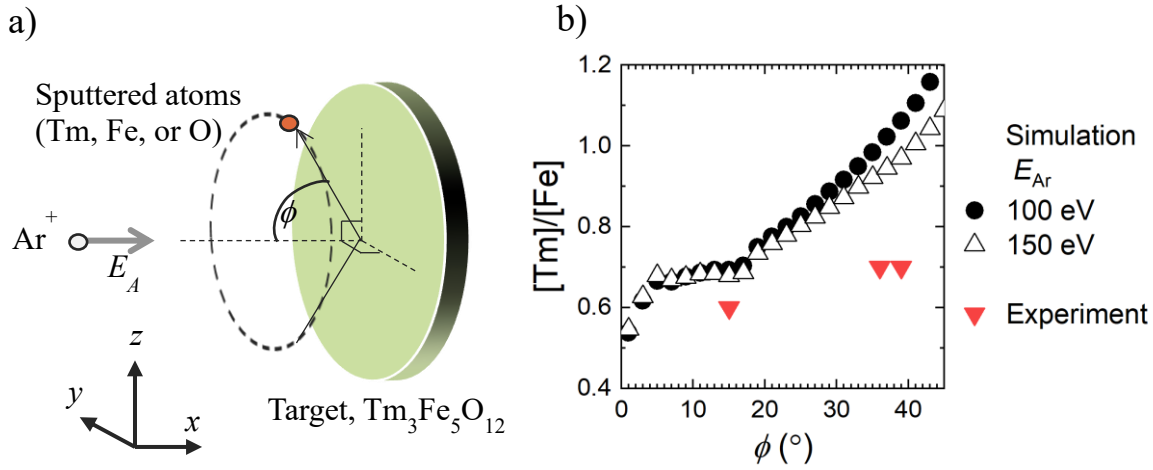

Figure 5.5 Dependence of Tm/Fe ratio on angle, by TRIM simulation. a). Schematic of the model simulation. The spreading angle of Fe and Tm based on the x-axis (ϕ) is examined. b). Graph of the dependence of the Tm/Fe ratio on (ϕ)

When the angle ϕ was within the range of 5 to 18°, the concentration ratio between Tm and Fe was approximately 0.6. However, in the ϕ range above 20°, the concentration ratio surpassed 0.7. It can be postulated that the disparate sputtering angles between Tm and Fe resulted in heterogeneous chemical compositions within the film at varying positions. Future investigations will aim to offer a more quantifiable understanding of how growth conditions influence the chemical composition.

The surface morphology of the film, as shown in Fig. 5.6a, exhibits a root mean square (RMS) roughness of 0.4 nm, which is close to the findings presented in another report[12]. In Figure 5.6b, the hysteresis pattern of the TmIG film positioned at point A, with a thickness of 24 nm, is depicted. Upon applying an in-plane magnetic field, the film demonstrates a higher saturation field that that under the application of an out-of-plane field. This behavior implies that the film's preferred orientation aligns with the out-of-plane direction, indicating PMA properties. Figure 5.7a presents the thickness dependency of the film grown at point A. The saturation magnetization (M_s) values for film thicknesses of 18,

24, and 30 nm were found to be 98, 108, and 55 kA/m, respectively. The observed reduction in M_s at t = 30 nm aligned with the prior findings reported by Duong et al. and could be attributed to stress relaxation within the film[36].

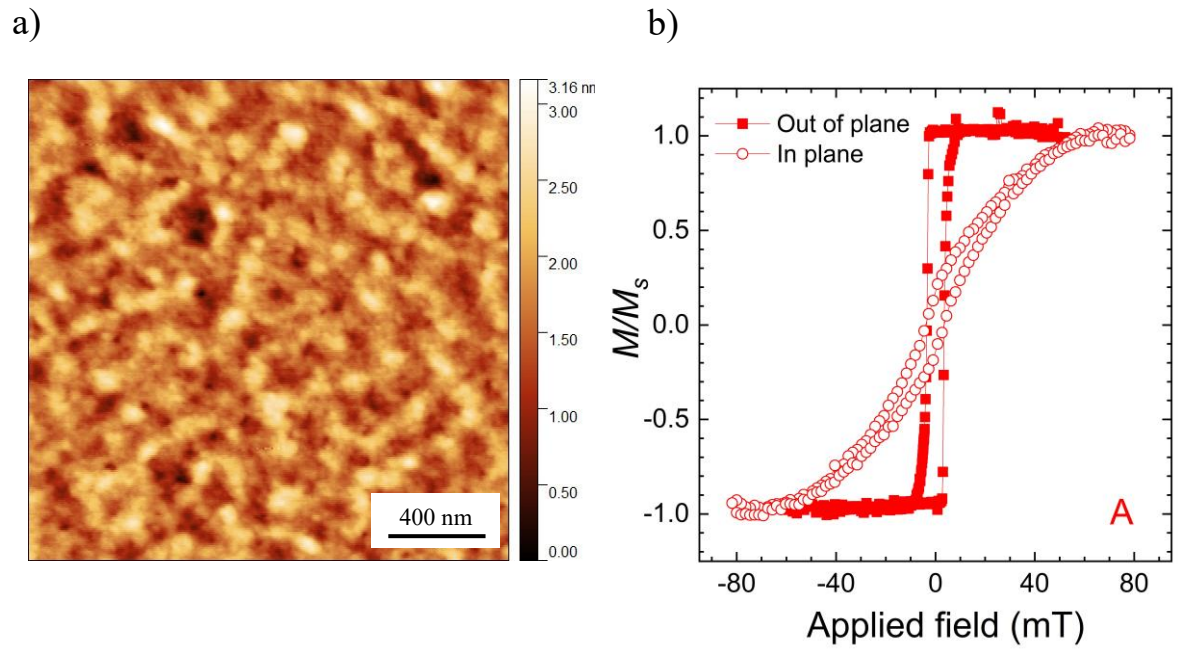

Figure 5.6 a) Surface morphology and b). hysteresis loop of TmIG films measured for out-of-plane and in-plane fields for a thickness of 24 nm.

Figure 5.7b shows the magnetometry results of films with different compositions. All films showed a hysteresis loop in their *M–H* curves under an out-of-plane applied field. The M_s values at growth positions B and C were quantified as 23 and 30 kA/m, respectively, notably lower than that at position A. This reduction in M_s in Tm-enriched films aligned with the findings of Wu et al.[28], who attributed it to the presence of Fe vacancies at tetrahedral sites. Therefore, within slightly off-stoichiometric TmIG films, the existence of Fe vacancies at tetrahedral sites resulted in a reduction of magnetic moment.

FMR measurements were used to determine the effective anisotropy energy (K_{eff}) of the TmIG film (t = 24 nm) at position A. In these measurements, an AC field (h_{rf}) was applied to the film under a static external field (H) at various angles relative to the film plane (θ_H), as shown in Figure 5.8a. Figure 5.8b demonstrates the representative FMR spectra at θ_H = 0, 30, 60, 90, and 120°, highlighting distinct FMR signals. After processing the raw data, the angular dependence of the resonance field (μ_{0HFMR}) was obtained by utilizing the

peak search function available in this instrument.

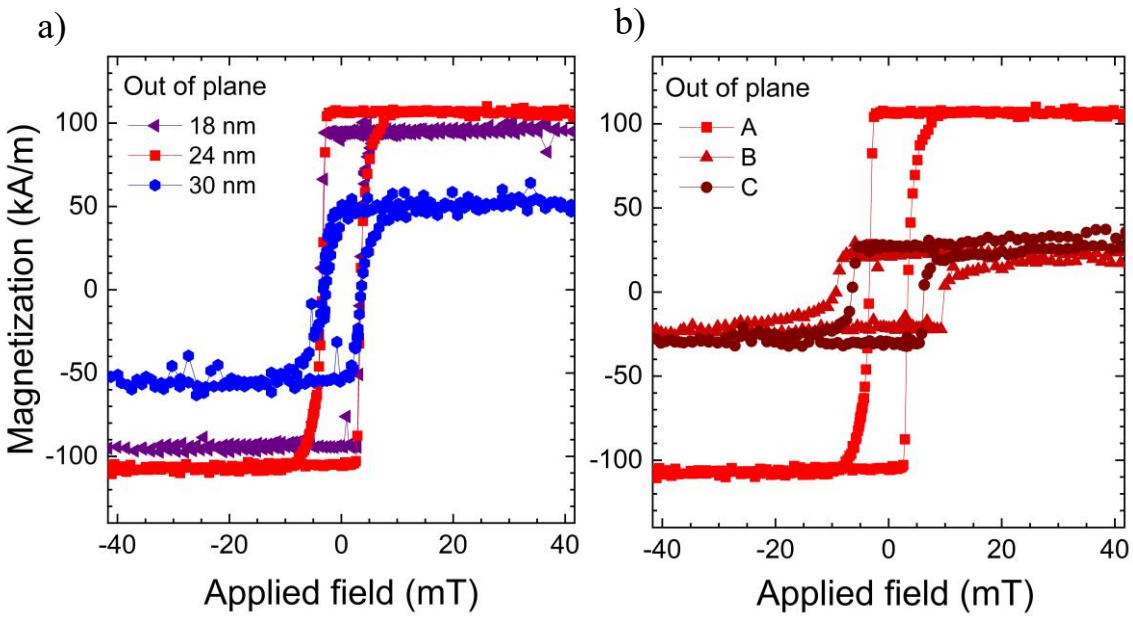

Figure 5.7 The hysteresis loops of TmIG films for out-of-plane field: a). different thicknesses and b). different compositions.

This dependence was plotted in Fig. 5.8c, where black symbols represent μ_{0HFMR}. The uniaxial magnetic anisotropy field (h_u) was quantified by the following equation[37]:

$$\left(\frac{\omega}{\gamma}\right)^2 = [\mu_0 H_{FMR}\cos(\theta_H - \theta) - h_u\cos(2\theta)] \times [\mu_0 H_{FMR}\sin(\theta_H - \theta) + h_u\sin^2 2\theta] = 0 \quad (5.1)$$

$$\mu_0 H_{FMR}\sin(\theta_H - \theta) + \frac{h_u}{2}\sin 2\theta = 0 \quad (5.2)$$

In the equations, $\omega = 2\pi f$ and $\mu_0 H_{FMR}$ symbolize the angular frequency of the applied microwave and resonance field extracted from the FMR spectra, respectively. The angles of θ_H and θ represent the angle of the applied field and M_s relative to the film plane, respectively. The identification of the minimum value at 100° supports the claim of PMA in the film. Equations (5.1) and (5.2) were approached iteratively by substituting the measured resonance field and uniaxial magnetic anisotropy field (h_u) of the TmIG film, which yielded a value of -0.16 T. The K_{eff} calculated as $K_{eff} = h_u M_s/2$ was approximated to be 8.6 kJ/m^3, with M_s = 108 kA/m, obtained via SQUID magnetometry under an out-of-plane applied field. These results were consistent with those reported by other research teams employing pulsed laser deposition (PLD) and off-axis sputtering methods[12,28,36]. The outcomes indicated that oxygen ion bombardment of the substrate did not significantly affect the magnetic anisotropy

or magnetic moment in a magnetic insulator. However, in the realm of semiconductor application, it did attenuate the conductivity of the film[38].

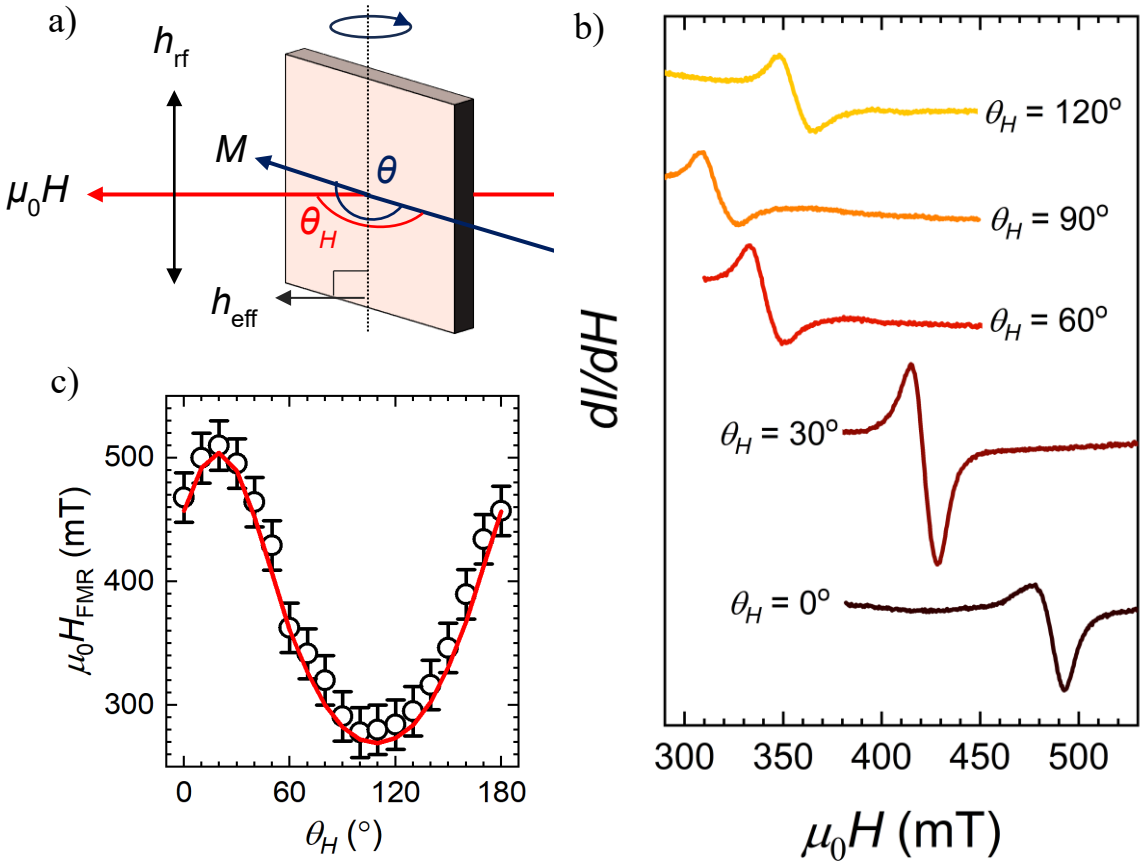

Figure 5.8 Angle dependence of the resonance field of TmIG film for position A and thickness 24 nm. a). Schematic of the measurement set up. b). FMR curves at various angles. c). θ_H-dependence of the resonance field.

To analyze the domain morphology, TmIG films with different thicknesses were examined using a polar magneto-optical Kerr effect microscopy. The experimental procedure began with the application of an out-of-plane magnetic field, succeeded by AC demagnetization, followed by the acquisition of microscopic images, as depicted in Fig. 5.9a–c. These images revealed a maze domain pattern characteristic of PMA, thereby validating our successful implementation of on-axis sputtering fabrication for TmIG with PMA. Similar maze domain patterns were verified for films deposited with varying thicknesses, for position A. Two-dimensional Fast Fourier Transforms (FFT) were used, and

the intensity was radially averaged. Fig. 5.9d illustrates the relationship between the normalized intensity and radius.

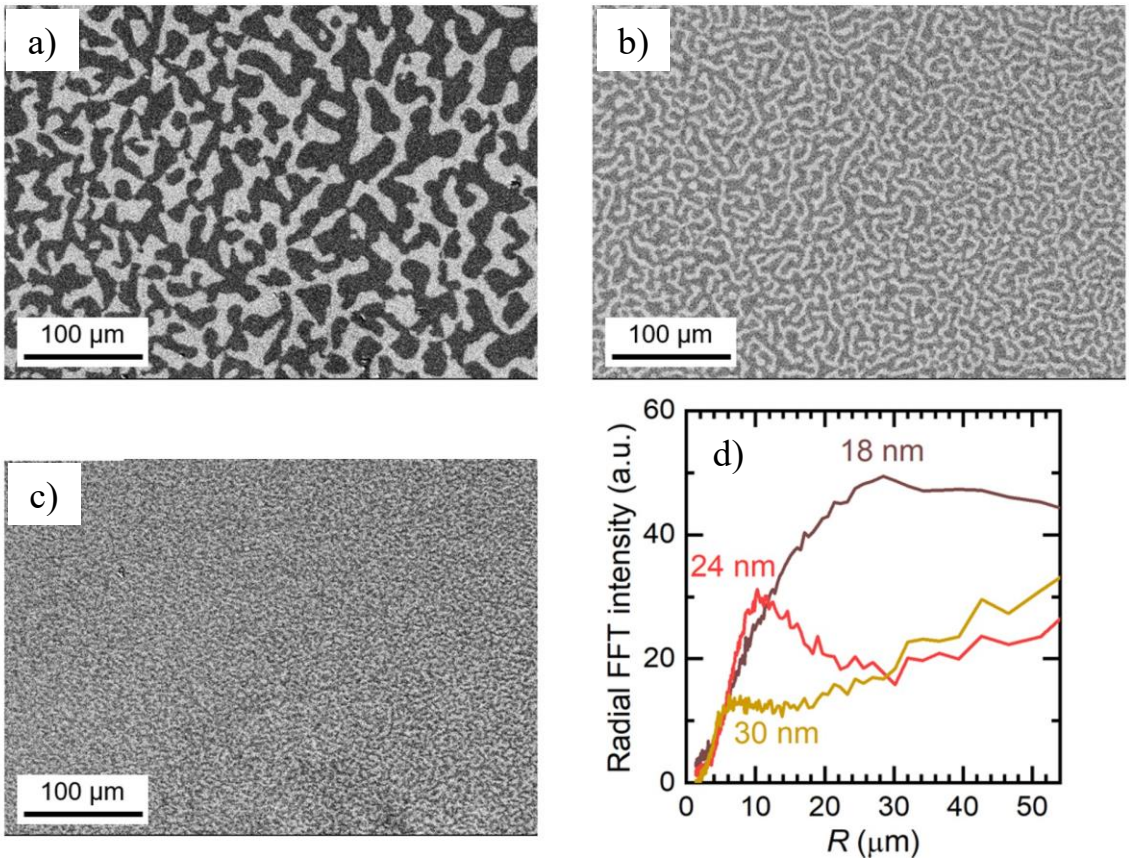

Figure 5.9 Dependence of maze domains of various thicknesses evaluated using Kerr microscope. a). 18 nm, b). 24 nm, and c). 30 nm. d). Two-dimensional FFT of radially averaged microscopic image intensity.

By fitting a Gaussian function, the stripe spacing (D_S) was determined to be 28, 11, and 8 μm for thicknesses of 18, 24, and 30 nm, respectively. Using these results, the Kaplan–Gehring model was used to estimate the domain wall energy density (σ_{DW}), expressed as[27]

$$\sigma_{DW} = \frac{2K_d t}{\pi} \ln\left[\frac{D_S}{t \exp\left(\frac{\pi b}{2} + 1\right)}\right] \tag{5.3}$$

where t is the film thickness, b = -0.666 is a model-dependent constant, and $K_d = \mu_0 \frac{M_S^2}{2}$ is the dipolar energy constant. The domain wall energy density was calculated to be 0.51 mJ/m^2 for 18 nm, 0.69 mJ/m^2 for 24 nm, and 0.2 mJ/m^2 for 30 nm.

The decrease in saturation M_s led to a corresponding reduction in the domain-wall energy density, as illustrated in Fig. 5.8. Consequently, this decrease contributed to a diminution in domain spacing. These values were consistent with those reported for other TmIG films prepared by pulsed laser deposition (PLD) or off-axis sputtering[12,27,28]. The exchange stiffness of the 24 nm thick film was estimated to be A_{ex} = 3.4 pJ/m using the equation $A_{ex} = \frac{\sigma_{DW}^2}{16K_{eff}}$. The variation in A_{ex} could be attributed to the nonuniformity of the film thickness in the film, which had an RMS roughness of 0.4 nm.

5.2. *Large-scale Fabrication of $Tm_3Fe_5O_{12}$ Films with PMA by Sputtering*

Based on the without-rotation method, the difference in sample positioning revealed that the Tm/Fe ratio was not significantly different. Position A had a ratio of 0.6. The ratio of the other position, which had a lower thickness and the same radius from the center of the substrate holder, was not too far from the stoichiometric ratio (Tm/Fe of 0.7). Thus, rotating the substrate during deposition to produce a larger film area holds promise for achieving a Tm/Fe ratio within this range (0.6–0.7). XRR techniques were used to measure the thickness of the TmIG film, which was found to be approximately 20 nm. The composition was analyzed via XRF using the FP method. This analysis revealed distinct peaks corresponding to Tm and Fe, as shown in Fig. 5.10a and 5.10b, resulting in a Tm/Fe ratio of 0.65. These findings closely match the known bulk composition of TmIG and are consistent with the results in prior research[28].

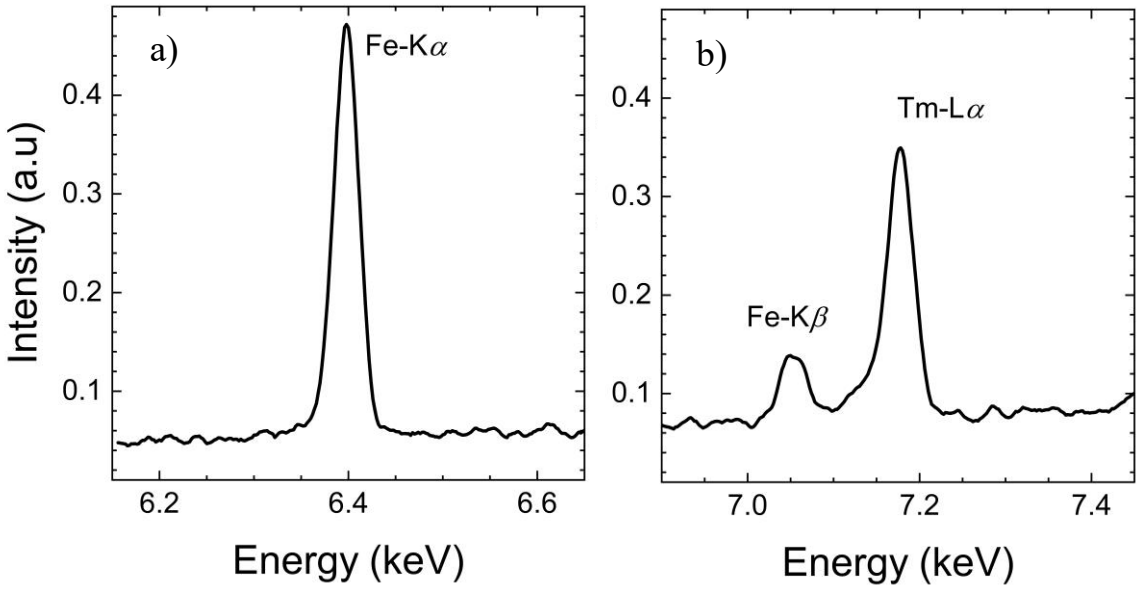

Figure 5.10 XRF spectra of TmIG film. a). Fe and b). Tm

XRD was performed to analyze the crystalline structure of the TmIG film at different postannealing temperatures (T_{an}), as shown in Fig. 5.11. Only substrate peaks were observed in the as-deposited state. However, T_{an} of 650 and 800 °C broadened the curve surrounding the TmIG (444) peak. Notably, a distinct peak characteristic of TmIG emerged for T_{an} at 950 °C. The observed results suggest that T_{an} plays a critical role in shaping the growth of the TmIG crystal structure, a phenomenon consistent with the existing literature[29]. Higher

post-annealing temperatures lead to lattice strains, which promote the formation of the TmIG crystal structure.

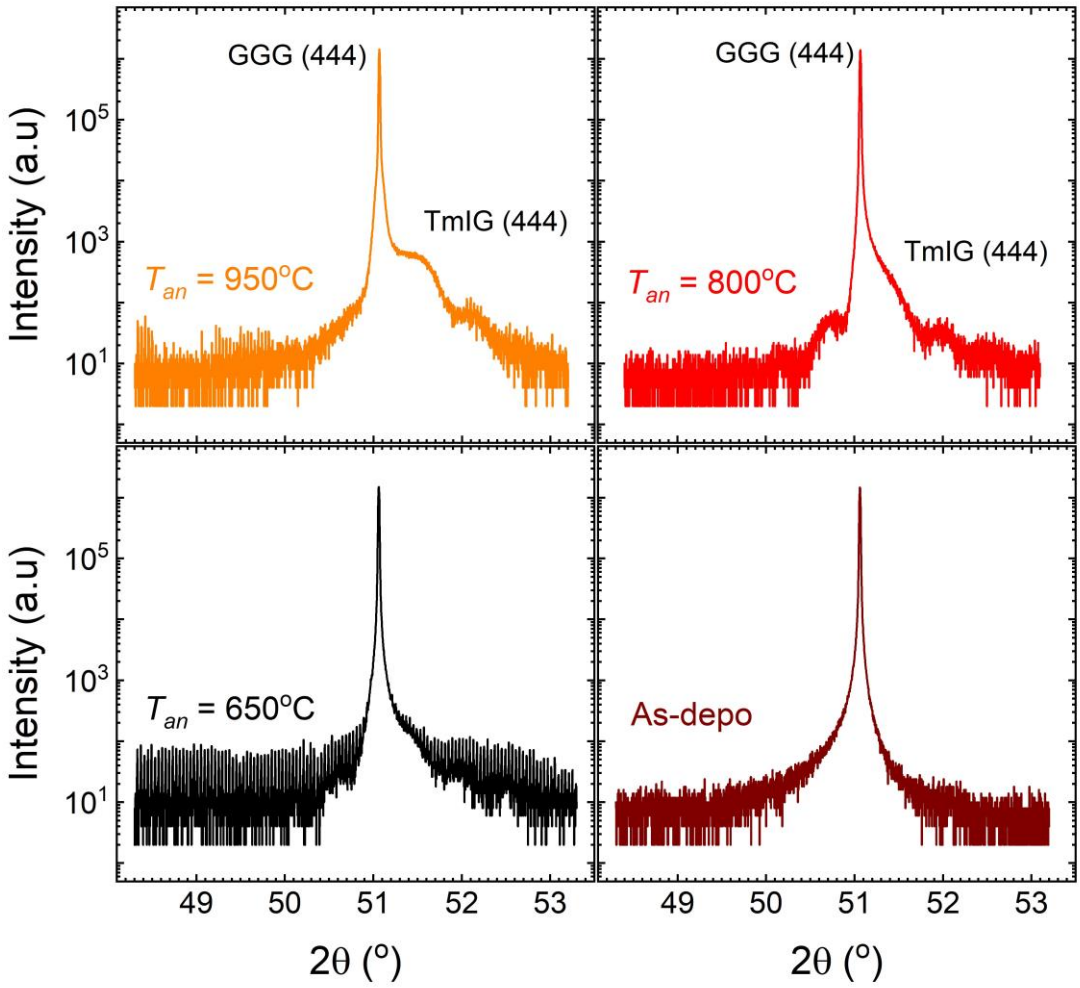

Figure 5.11 XRD pattern of TmIG film with various T_{an}.

To validate the presence of strain in our film, the lattice constants (c and a) and in-plane strain were calculated based on the XRD pattern, as follows[29];

$$c = \frac{\lambda\sqrt{h^2 + k^2 + l^2}}{2sin\theta} \tag{5.4}$$

$$a \approx \sqrt{\frac{1.233^3}{c}} \tag{5.5}$$

$$\varepsilon_{II\%} = \frac{a - a_{TIG}}{a_{TIG}} \times 100\% \tag{5.6}$$

where θ, c, a, and a_{TIG} represent the diffraction angle, out-of-plane, in-plane, and unstrained lattice constants (1.233 nm) of TmIG, respectively. The parameters h, k, and l signify the Miller indices of the crystal planes, while ε_{II} denotes the in-plane strain. The calculation results for the film annealed at 950 °C indicated that c, a, and ε_{II} were 1.229, 1.235, and 0.16%, respectively, suggesting that the lattice constant of the film was strained[29]. This strained lattice constant possessed the potential to induce magneto-crystalline anisotropy, transitioning from an in-plane magnetic anisotropy (IMA) to perpendicular magnetic anisotropy (PMA). However, the lattice constants for the other conditions (as-deposited, annealed at 650 and 800 °C) were not determined due to unclear or absent peak positions for TmIG (444).

The hysteresis loop of the TmIG film, with an out-of-plane field direction, for various post-annealing temperatures evaluated by SQUID MPMS3 at room temperature, is displayed in Fig. 5.12. The paramagnetic background from the GGG substrates has been subtracted. The saturation magnetization (M_s) for T_{an} at 650 and 800 °C was obtained as 10 kA/m, while the M_s for T_{an} of 950 °C was 40 kA/m. Additionally, the coercive field (H_c) of the film was noted as 0.22 mT for T_{an} of 650 and 800 °C, and 1.5 mT for a T_{an} of 950 °C. These results align with the XRD findings, wherein the films annealed at 650 and 800 °C exhibit a broadened pattern and lack a definitive TmIG peak, suggesting minimal or no strain on the lattice constant of the film, thereby resulting in a lower M_s. Conversely, the TmIG film annealed at 950 °C, where lattice constant strain was evident, displays a fourfold increase in M_s. This rise in M_s with increasing T_{an} was also reported by Duong et al[36]. They successfully controlled and attained M_s values close to that of bulk TmIG with a T_{an} of 1000 °C.

Figure 5.13a illustrates a comparison of the magnetization, particularly between the out-of-plane and in-plane magnetic fields, for a TmIG film subjected to T_{an} of 950 °C. The results indicate that the M_s in the in-plane direction surpasses that in the out-of-plane direction, suggesting a predominant out-of-plane magnetization orientation in the TmIG film[4,26,39,40]. This observation is consistent with results in the previous report.

In various applications, especially those involving heterostructures, the surface properties of the films play crucial roles[22]. Figure 5.13b presents the surface morphology of the TmIG film (scanned in 5 μm × 5 μm area) after a T_{an} of 950 °C. Analysis of the surface

morphology revealed an RMS roughness of 0.8 nm, which closely corresponded to findings reported in other studies[22,41].

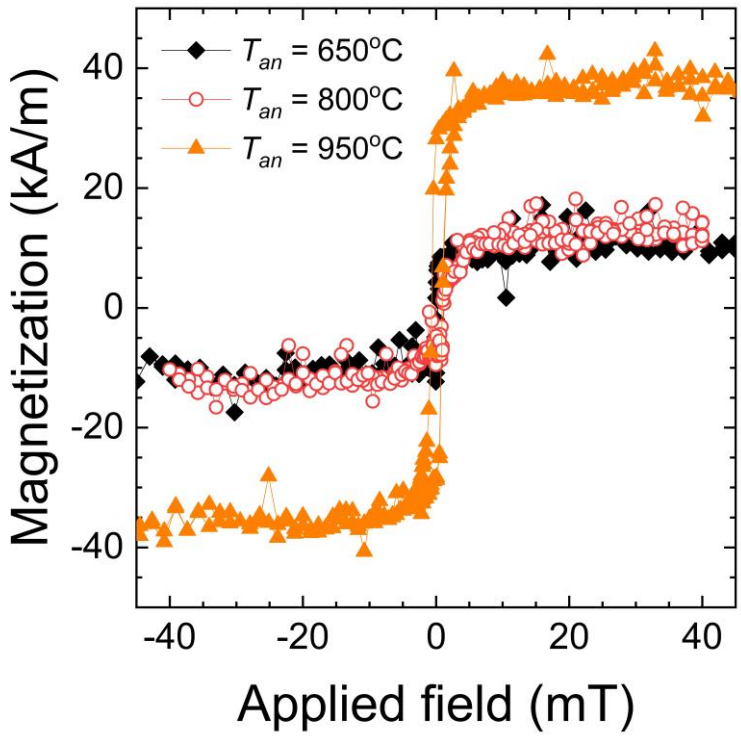

Figure 5.12 Hysteresis loop of TmIG films for out-of-plane field with various T_{an}.

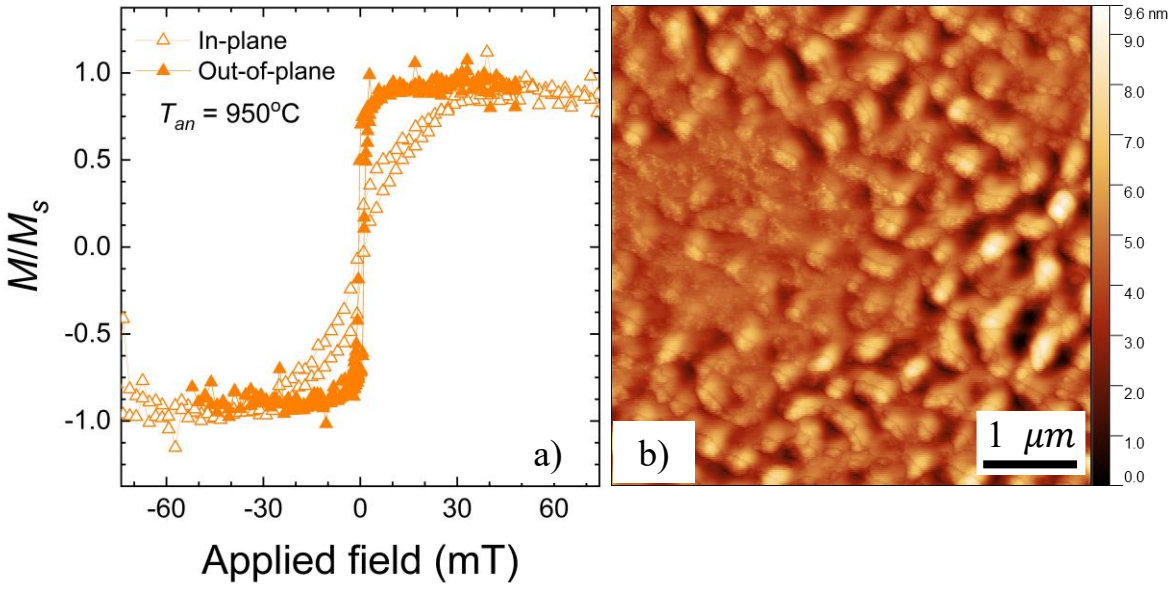

Figure 5.13 a). Hysteresis loop of the out-of-plane and in-plane measurements. b). Surface morphology for a thickness of 20 nm.

The preferred orientation of the magnetic moment was determined by the effective magnetic anisotropy (K_{eff}), which was influenced by three main factors: magneto-crystalline anisotropy (K_{cr}), shape anisotropy (K_{sh}), and magneto-elastic anisotropy (K_{el})[42].

$$K_{eff} = K_{cr} + K_{sh} + K_{el} \tag{5.7}$$

Magneto-crystalline anisotropy refers to the orientation of magnetization along a preferred direction within a crystal structure. The contribution of K_{cr} to the total magnetic anisotropy is small compared to the other types such as K_{sh} and K_{el}. The low bulk K_{cr} has a negligible effect on the total magnetic anisotropy[27]. Shape anisotropy, which is determined by the three-dimensional configuration of a material, significantly influences the direction of the magnetic moment. It can be estimated as follows[22]:

$$K_{sh} = \frac{\mu_0}{2} M_s^2 \tag{5.8}$$

The symbol M_s denotes the saturation magnetization in the easy axis direction. Magneto-elastic anisotropy arises from the strain or stress affecting the lattice constant. In this context, the lattice constant of the GGG substrate is larger than that of the TmIG film, causing strain in the TmIG lattice. This strain can potentially reorient the easy axis direction. The shift of the easy axis from an in-plane to an out-of-plane orientation occurs when the magnitude of K_{el} surpasses that of K_{sh}. The value of K_{el} can be determined using the following equation[24]:

$$K_{el} = -\frac{3}{2} \lambda_{111} \sigma_{II} \tag{5.9}$$

λ_{111} refers to the magnetostriction constant along the (111) direction, while σ_{II} represents the in-plane stress induced in the material by the lattice mismatch between the GGG substrate and TmIG film, which can be determined using the following formula[42] :

$$\sigma_{II} = \frac{Y}{1-\nu} \varepsilon_{II} \tag{5.10}$$

Here, Y and ν represent the Young's modulus (2×10^{11} Pa) and Poisson's ratio (0.29), respectively, for all garnet types[42]. By applying the above formula, the K_{eff} for a TmIG film with T_{an} of 950 °C and thickness of 20 nm was calculated to be -2.5 kJ/m^3. The negative K_{eff} indicated that the magneto-elastic anisotropy exceeded the shape anisotropy to

change the easy direction from in-plane to out-of-plane, as shown in Fig. 5.13a. The reduction in K_{eff} from that in the previous section (-8.6 kJ/m^3) was due to stoichiometric deviations (0.6) induced by averaging the Tm/Fe ratio over the donut area (the shaded area in Fig. 5.1a).

To validate this method with thinner films, a TmIG film of thickness 10 nm was fabricated using the same growth parameters as those for the 20 nm film. XRD and SQUID MPMS3 measurements were conducted to assess the crystal structure and PMA properties, respectively. Fig. 5.14 presents the XRD pattern of the TmIG film subjected to various T_{an} (650, 800, and 950 °C). This pattern exhibits resemblances to the 20 nm thick film; initially, only substrate peaks were observed in the as-deposited state. Subsequent annealing at 650 and 800 °C resulted in broadening around the TmIG (444) peak, while a sharper peak emerged at 950°C.

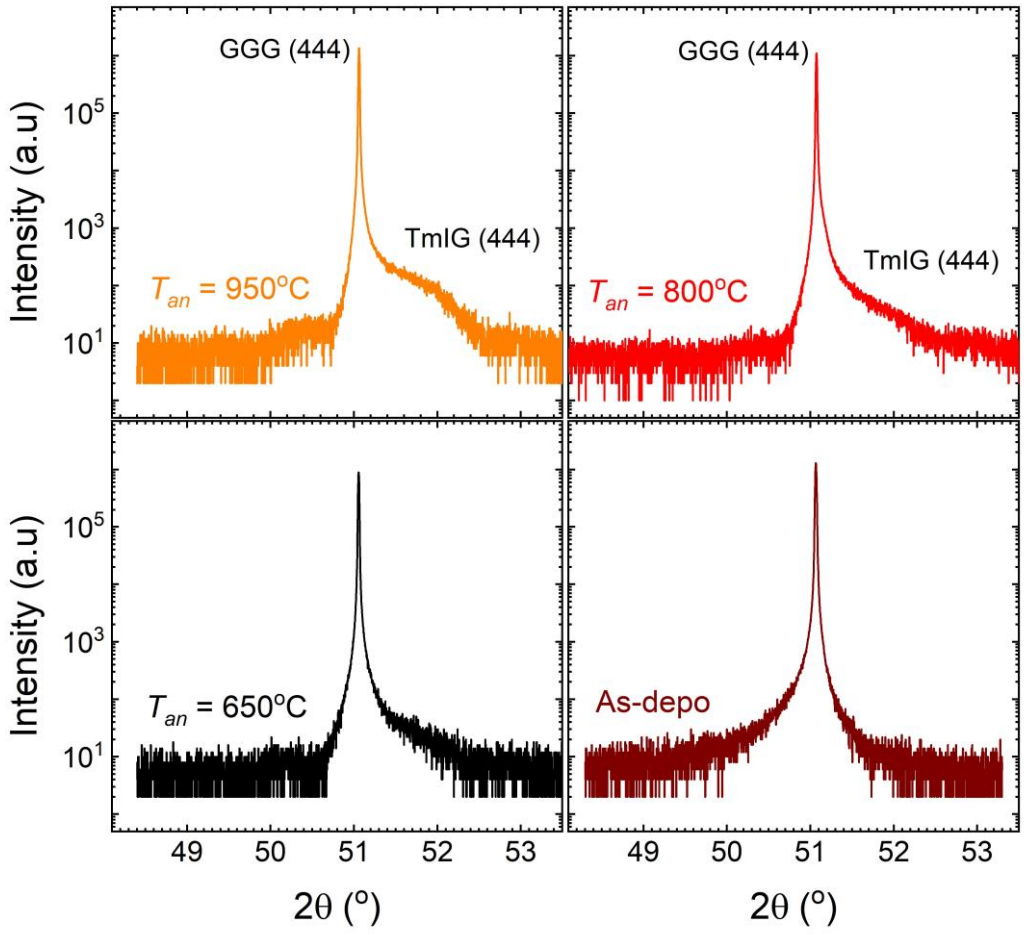

Figure 5.14 XRD patterns of 10 nm thick TmIG film for various T_{an}.

Figure 5.15 depicts a comparison of the hysteresis loop between the out-of-plane and in-plane magnetic fields for a 10 nm thick film annealed at 950 °C. Similar to the behavior observed in the 20 nm film, the easy axis orientation of M_s was perpendicular to the film plane, demonstrating PMA properties. These findings confirm that TmIG films with expanded surface areas and PMA attributes can be grown through on-axis sputtering using rotational techniques.

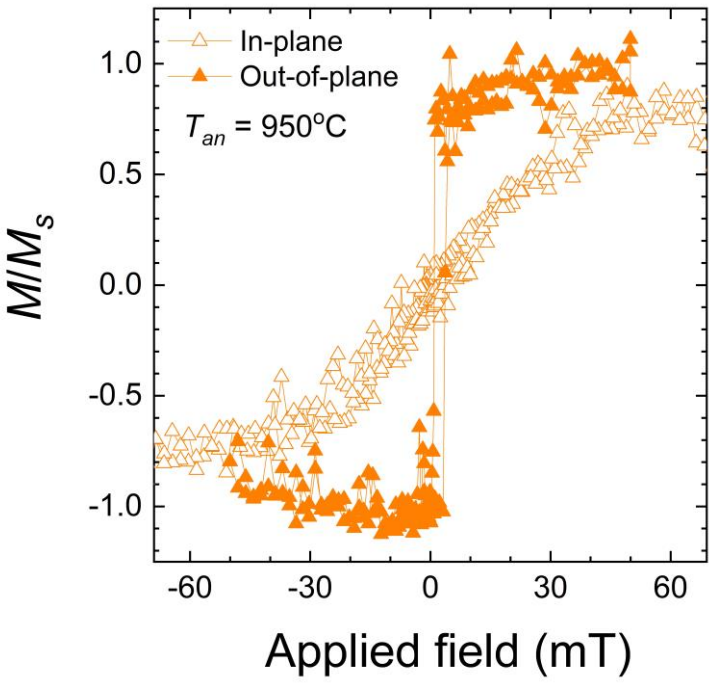

Figure 5.15 Hysteresis loop of the out-of-plane and in-plane measurements for a thickness of 10 nm.

5.4 Conclusions

In summary, the on-axis sputtering deposition of PMA-TmIG was demonstrated, both with and without the rotation technique. The stoichiometric TmIG film was attained successfully by positioning the sample appropriately on the substrate, relative to the target. In the absence of rotation, PMA was achieved through hysteresis loop patterns, angle dependence of FMR, and observations using a polar magneto-optical Kerr effect microscope. The effective anisotropy measured at 8.6 kJ/m^3 aligned with previous findings from studies utilizing PLD and off-axis sputtering. These results demonstrated the stability of magnetic anisotropy and moment in the ferrimagnetic insulator during ion-bombardment deposition. In addition, large-scale TmIG films were successfully fabricated, with thicknesses of 20 nm and 10 nm, on GGG (111) under rotational conditions, producing a total film area of 25 cm^2, six times larger than that achievable with the nonrotational method. By optimizing the growth parameters of TmIG and ensuring the substrate's placement at a consistent radius from the center of the substrate holder, a Tm/Fe ratio close to stoichiometry was achieved. Post-annealing treatment induced lattice strain, leading to the growth of the crystal structure (444) and a distinct peak in the saturation field at a T_{an} of 950 °C. This investigation highlights the potential of our approach for large-scale TmIG fabrication with PMA , offering significant improvements in the production efficiency, for the industry.

References

1. Y. Kajiwara, K. Harii, S. Takahashi, J. Ohe, K. Uchida, M. Mizuguchi, H. Umezawa, H. Kawai, K. Ando, K. Takanashi, S. Maekawa, E. Saitoh, *Nature*. **464**, 262–266 (2010).

2. H. Nakayama, M. Althammer, Y. T. Chen, K. Uchida, Y. Kajiwara, D. Kikuchi, T. Ohtani, S. Geprägs, M. Opel, S. Takahashi, R. Gross, G. E. W. Bauer, S. T. B. Goennenwein, E. Saitoh, *Phys. Rev. Lett.* **110**, 1–5 (2013).

3. C. O. Avci, A. Quindeau, C. F. Pai, M. Mann, L. Caretta, A. S. Tang, M. C. Onbasli, C. A. Ross, G. S. D. Beach, *Nat. Mater.* **16**, 309–314 (2017).

4. H. Bai, Z. Z. Zhu, J. T. Ke, G. Li, J. Su, Y. Zhang, T. Zhu, J. W. Cai, *Phys. Rev. Appl.* **17**, 1–9 (2022).

5. J. Zou, S. Bosco, B. Pal, S. S. P. Parkin, J. Klinovaja, D. Loss, *Phys. Rev. Res.* **5**, 1–13 (2023).

6. C. Hauser, T. Richter, N. Homonnay, C. Eisenschmidt, M. Qaid, H. Deniz, D. Hesse, M. Sawicki, S. G. Ebbinghaus, G. Schmidt, *Sci. Rep.* **6** (2016), doi:10.1038/srep20827.

7. M. Kubota, A. Tsukazaki, F. Kagawa, K. Shibuya, Y. Tokunaga, M. Kawasaki, Y. Tokura, *Appl. Phys. Express*. **5** (2012), doi:10.1143/APEX.5.103002.

8. C. O. Avci, E. Rosenberg, M. Baumgartner, L. Beran, A. Quindeau, P. Gambardella, C. A. Ross, G. S. D. Beach, *Appl. Phys. Lett.* **111** (2017), doi:10.1063/1.4994050.

9. J. J. Bauer, E. R. Rosenberg, S. Kundu, K. A. Mkhoyan, P. Quarterman, A. J. Grutter, B. J. Kirby, J. A. Borchers, C. A. Ross, *Adv. Electron. Mater.* **6** (2020), doi:10.1002/aelm.201900820.

10. Q. Shao, Y. Liu, G. Yu, S. K. Kim, X. Che, C. Tang, Q. L. He, Y. Tserkovnyak, J. Shi, K. L. Wang, *arXiv*, 1–17 (2019).

11. S. Vélez, S. Ruiz-Gómez, J. Schaab, E. Gradauskaite, M. S. Wörnle, P. Welter, B. J. Jacot, C. L. Degen, M. Trassin, M. Fiebig, P. Gambardella, *Nat. Nanotechnol.* **17**, 834–841 (2022).

12. C. N. Wu, C. C. Tseng, K. Y. Lin, C. K. Cheng, S. L. Yeh, Y. T. Fanchiang, M. Hong,

J. Kwo, *AIP Adv.* **8**, 6–12 (2018).

13. S. Ding, A. Ross, R. Lebrun, S. Becker, K. Lee, I. Boventer, S. Das, Y. Kurokawa, S. Gupta, J. Yang, G. Jakob, M. Kläui, *Phys. Rev. B.* **100**, 100406 (2019).

14. Y. Yang, T. Liu, L. Bi, L. Deng, *J. Alloys Compd.* **860**, 158235 (2021).

15. H. Zhang, Y. Zhang, Z. Hou, M. Qin, X. Gao, J. Liu, *Mater. Futur.* **2** (2023), doi:10.1088/2752-5724/ace1df.

16. S. Vélez, J. Schaab, M. S. Wörnle, M. Müller, E. Gradauskaite, P. Welter, C. Gutgsell, C. Nistor, C. L. Degen, M. Trassin, M. Fiebig, P. Gambardella, *Nat. Commun.* **10**, 1–8 (2019).

17. S. Xia, S. Zhang, Z. Luan, L. Zhou, J. Liang, G. Liu, B. Yang, H. Yang, R. Liu, D. Wu, *Appl. Phys. Lett.* **116** (2020), doi:10.1063/1.5134762.

18. A. J. Lee, A. S. Ahmed, J. Flores, S. Guo, B. Wang, N. Bagués, D. W. Mccomb, F. Yang, *Phys. Rev. Lett.* **124** (2020), doi:10.1103/PhysRevLett.124.107201.

19. L. Caretta, E. Rosenberg, F. Büttner, T. Fakhrul, P. Gargiani, M. Valvidares, Z. Chen, P. Reddy, D. A. Muller, C. A. Ross, G. S. D. Beach, *Nat. Commun.* **11**, 1–9 (2020).

20. T. Fakhrul, S. Huang, Y. Song, B. Khurana, G. S. D. Beach, C. A. Ross, *Phys. Rev. B.* **107**, 54421 (2023).

21. R. Timalsina, H. Wang, B. Giri, A. Erickson, X. Xu, A. Laraoui, *Adv. Electron. Mater.* **2300648**, 1–10 (2023).

22. A. Quindeau, C. O. Avci, W. Liu, C. Sun, M. Mann, A. S. Tang, M. C. Onbasli, D. Bono, P. M. Voyles, Y. Xu, J. Robinson, G. S. D. Beach, C. A. Ross, *Adv. Electron. Mater.* **3** (2017), doi:10.1002/aelm.201600376.

23. G. L. S. Vilela, E. Santos, J. E. Abrao, A. R. Rodrigues, S. M. Rezende, A. Azevedo, J. S. Moodera, *Appl. Phys. Lett.* **120** (2022), doi:10.1063/5.0082849.

24. S. Mokarian Zanjani, M. C. Onbaşlı, *J. Magn. Magn. Mater.* **499**, 166108 (2020).

25. O. Ciubotariu, A. Semisalova, K. Lenz, M. Albrecht, *Sci. Rep.* **9**, 1–8 (2019).

26. C. Tang, P. Sellappan, Y. Liu, Y. Xu, J. E. Garay, J. Shi, *Phys. Rev. B.* **94**, 1–5 (2016).

27. E. R. Rosenberg, K. Litzius, J. M. Shaw, G. A. Riley, G. S. D. Beach, H. T. Nembach, C. A. Ross, *Adv. Electron. Mater.* **7**, 1–11 (2021).

28. C. N. Wu, C. C. Tseng, Y. T. Fanchiang, C. K. Cheng, K. Y. Lin, S. L. Yeh, S. R. Yang, C. T. Wu, T. Liu, M. Wu, M. Hong, J. Kwo, *Sci. Rep.* **8** (2018), doi:10.1038/s41598-018-29493-5.

29. G. Vilela, H. Chi, G. Stephen, C. Settens, P. Zhou, Y. Ou, D. Suri, D. Heiman, J. S. Moodera, *J. Appl. Phys.* **127** (2020), doi:10.1063/1.5135012.

30. D. H. A. Blank, M. Dekkers, G. Rijnders, *J. Phys. D. Appl. Phys.* **47** (2014), doi:10.1088/0022-3727/47/3/034006.

31. D. Fischer, G. F. De La Fuente, M. Jansen, *Rev. Sci. Instrum.* **83** (2012), doi:10.1063/1.3697861.

32. P. Kuppusami, V. S. Raghunathan, *Surf. Eng.* **22**, 81–83 (2006).

33. U. Betz, M. Kharrazi Olsson, J. Marthy, M. F. Escolá, F. Atamny, *Surf. Coatings Technol.* **200**, 5751–5759 (2006).

34. K. Alshammari, E. Haltz, M. Alyami, M. Ali, P. S. Keatley, C. H. Marrows, J. Barker, T. A. Moore, *Phys. Rev. B.* **104**, 1–6 (2021).

35. H. Takahara, *Rigaku J.* **33**, 17–21 (2017).

36. V. D. Duong, P. Cao Van, T. Nguyen Thi, H. Y. Ahn, V. A. Cao, J. Nah, G. Kim, K. S. Lee, J. W. Kim, J. R. Jeong, *J. Alloys Compd.* **927**, 166800 (2022).

37. S. Yoshii, K. Kato, E. Shigematsu, R. Ohshima, Y. Ando, K. Usami, M. Shiraishi, *Phys. Rev. B.* **106**, 1–9 (2022).

38. A. Bikowski, T. Welzel, K. Ellmer, *Appl. Phys. Lett.* **102** (2013), doi:10.1063/1.4811647.

39. F. Büttner, M. A. Mawass, J. Bauer, E. Rosenberg, L. Caretta, C. O. Avci, J. Gräfe, S. Finizio, C. A. F. Vaz, N. Novakovic, M. Weigand, K. Litzius, J. Förster, N. Träger, F. Groß, D. Suzuki, M. Huang, J. Bartell, F. Kronast, J. Raabe, G. Schütz, C. A. Ross, G. S. D. Beach, *Phys. Rev. Mater.* **4**, 17–19 (2020).

40. Y. Meng, P. Chen, W. He, H. Zhuang, J. Li, J. Dong, X. Li, L. Wang, Q. Guo, J. Yang,

Y. Ji, X. Shen, X. Yu, G. Yu, J. Li, X. Han, R. Yu, *Small*. **2308724**, 1–8 (2024).

41. Y. Zhang, Q. Yang, X. Liu, D. Zhang, Y. Rao, H. Zhang, *AIP Adv.* **11** (2021), doi:10.1063/5.0050340.

42. J. Fu, M. Hua, X. Wen, M. Xue, S. Ding, M. Wang, P. Yu, S. Liu, J. Han, C. Wang, H. Du, Y. Yang, J. Yang, *Appl. Phys. Lett.* **110**, 3–8 (2017).

Chapter 6

Summary and Recommendations

6.1 Summary

The nanostructural effects of the nanoscale inhomogeneity in ZnO:Co films, serving as DMS, and nanoscale lattice strain in TmIG films, functioning as ferrimagnetic insulators, on their physical and chemical properties were studied in this dissertation. Through detailed analyses and advanced characterization techniques, the study explored how these nanostructure features influence the magnetic and structural behaviors of these materials, providing insights into their potential applications in spintronic devices.

The creation and control of inhomogeneities in the ZnO:Co film were successfully achieved via NMC. The inhomogeneities structure represented by the lattice parameter, grain size, and stoichiometry of ZnO were attributed to the transformation of magnetic properties. The superparamagnetic–ferromagnetic properties of ZnO:CoN films with the highest inhomogeneous structure were obtained at a T_{an} of 400 °C, under which condition the T_{an} was the optimum before N desorption. The analysis of the superparamagnetic–ferromagnetic properties revealed that the incorporation of Co and N atoms into the ZnO significantly deteriorated the grain size, in addition to producing disparities in both stoichiometry and lattice in the ZnO:CoN film at 400 °C. In addition, increasing the T_{an} above 400 °C resulted in a decrease in the N and increase in the O concentration, leading to an increase in the grain size and lattice parameters closer to that of bulk ZnO. The loss of superparamagnetic–ferromagnetic properties at high T_{an} indicated that the homogeneous structure reduced the magnetization of the film. For ZnO:Co films without nitrogen, the ferromagnetic properties were also observed at a T_{an} of 400 °C with higher M_s and H_c. In contrast to ZnO:CoN, the origin of ferromagnetism in the ZnO:Co film was dominated by the Co cluster and O_v. In addition, the growth of ZnO:Co using oxygen corroborated the hypothesis positing that a homogeneous structure and low Co content led to reduced M_{s} and H_{c}.

To focus on the impacts of nanoscale inhomogeneity on the magnetic properties, other structural and compositional differences among the samples were eliminated by preparing a set of samples by varying only the postannealing time. An enhancement of the coercivity and blocking temperature was observed with increasing postannealing duration without altering the wurtzite structure and chemical composition, suggesting that the postannealing changed the distribution of Co atoms in the film. The hypothesis that NMC induced the nanoscale inhomogeneity that largely enhanced H_{c} and T_{b} was corroborated

based on two different quantitative analyses: the ZFC–FC difference approach and EDX approach. A new method to analyze the nanoscale inhomogeneity from EDX was demonstrated and provided a direct measure of the inhomogeneity based on statistics. Gaussian distribution function reproduced the distribution of the $\rho_{Co}/[\rho_{Co}+\rho_{Zn}]$ well and enabled detailed discussion of the origin of the magnetic moment. Based on these studies, NMC proved to be an effective technique to control the inhomogeneous structure and phase of magnetic properties of the ZnO:Co film. This method has the potential to be applied to the development of DMS materials. In addition, the quantification of nanoscale inhomogeneities presented in this study offers a valuable approach to characterizing nanoscale inhomogeneities in solids and paves the way for further insights into DMS.

Nanoscale lattice strain-induced PMA properties in TmIG films grown on GGG (111) substrates using on-axis sputtering, both with and without substrate rotation during deposition, have been demonstrated. A stoichiometric TmIG film was successfully achieved from the sample deposited at an appropriate position on the substrate relative to the target. In the absence of rotation, PMA was confirmed through hysteresis loop patterns, angle dependence of FMR, and observations using a polar magneto-optical Kerr effect microscope. The effective anisotropy and saturation magnetization measured at 8.6 kJ/m^3 and 108 kA/m were consistent with the previous results from studies utilizing PLD and off-axis sputtering. Additionally, large-scale TmIG films were successfully fabricated, with thicknesses of 20 and 10 nm, on GGG (111) under rotational conditions, producing a total film area of 25 cm^2, six times larger than that achieved by the nonrotational method. Through the optimization of growth parameters for TmIG and ensuring consistent placement of the substrate at a uniform radius from the center of the substrate holder, a Tm/Fe ratio close to stoichiometry was achieved. The rise in post-annealing temperature induced lattice strain, promoting the growth of the crystal structure (444) and the emergence of a distinct peak in the saturation field. This investigation highlights the potential of our approach for large-scale TmIG fabrication with PMA properties, offering significant improvements in production efficiency for the industry.

6.2 Future recommendation

In this Ph.D. dissertation, extensive investigations have focused on two key issues: First, the exploration of nanoscale inhomogeneity within ZnO:Co films, revealing potential improvements in critical temperature; and second, the investigation of nanoscale lattice strain in TmIG films deposited on GGG substrate, poised to overcome the challenge of shape anisotropy and thereby achieve PMA properties. The nitrogen-mediated crystallization method was successfully used to induce and control inhomogeneities in the ZnO:Co film. The superparamagnetic-ferromagnetic properties of ZnO:CoN films are achieved at the most inhomogeneous structure, precisely at the optimal T_{an} just before N desorption begins. This study achieved notable enhancements in coercivity, blocking temperature, and the quantification of nanoscale inhomogeneity. However, the observation of coercive field at room temperature remains elusive. Recommendations for achieving this goal could include maintaining oxygen vacancies and further exploration of the Co-to-N ratio dependency.

The fabrication of TmIG films with PMA properties and larger areas was successfully achieved by on-axis sputtering, in contrast to previous reports that used unusual off-axis geometries. The PMA properties, which are critical for efficient manipulation of magnetization by spin-orbit torque injection from an adjacent conductive layer, were achieved by thermal annealing, with the thickness and Tm/Fe ratio controlled by the position of the substrate relative to the target. This investigation demonstrates the feasibility of the proposed approach for the large-scale fabrication of TmIG with PMA properties, thus offering significant improvements in fabrication efficiency for industrial applications. Therefore, it is advisable to extend the exploration of this method to encompass other rare-earth iron garnet materials and growth metal films deposited on rare-earth iron garnet. This pursuit aims to realize high-efficiency magnetization switching and ultrafast chiral domain motion. Such advances have the potential to catalyze the development of memory and logic devices with unprecedented capabilities.

List of Journal Publications

1. **Agusutrisno, M. N.,** Kamataki, K., Okumura, T., Itagaki, N., Koga, K., Shiratani, M., & Yamashita, N. **(2024)**. Effect of nanoscale inhomogeneity on blocking temperature of ZnO:Co films fabricated by nitrogen-mediated crystallization. *MRS Advances* (Accepted)
   https://doi.org/10.1557/s43580-024-00907-z

2. **Agusutrisno, M. N.,** Obinata, S., Kamataki, K., Okumura, T., Itagaki, N., Koga, K., Shiratani, M., & Yamashita, N. **(2024)**. Large-scale fabrication of thulium iron garnet film with perpendicular magnetic anisotropy using RF magnetron sputtering. *Japanese Journal of Applied Physics*. (Accepted)
   https://doi.org/10.35848/1347-4065/ad5aff

3. **Agusutrisno, M. N.,** Marrows, C. H., Kamataki, K., Okumura, T., Itagaki, N., Koga, K., Shiratani, M., & Yamashita, N. **(2024)**. On-axis sputtering fabrication of $Tm_3Fe_5O_{12}$ film with perpendicular magnetic anisotropy. *Thin Solid Films*, *788*, 140176.
   https://doi.org/10.1016/j.tsf.2023.140176.

4. **Agusutrisno, M. N.,** Narishige, R., Kamataki, K., Okumura, T., Itagaki, N., Koga, K., Shiratani, M., & Yamashita, N. **(2023)**. Control of inhomogeneity and magnetic properties of ZnO:Co films grown by magnetron sputtering using nitrogen. *Materials Science in Semiconductor Processing*, *162*, 107503.
   https://doi.org/10.1016/j.mssp.2023.107503.

5. **Agusutrisno, M. N.,** Yamashita, N., Kamataki, K., Koga, K., Itagaki, N., & Shiratani, M. **(2022)**. Control of magnetic transition of ZnO:Co grown by RF-sputter using post-annealing. In *2022 International Conference on Informatics Electrical and Electronics (ICIEE)* (pp. 1-4). IEEE.
   10.1109/ICIEE55596.2022.10010108

List of International Conferences

1. The 5th International Union of Materials Research Society (IUMRS), International Conference of Young Researcher on Advanced Materials (ICYRAM) 2022.
2. 9th International Symposium on control of Semiconductor Interfaces (ISCSI-IX) 2022.
3. 3rd International Conference on Informatics Electrical and Electronics (ICIEE) 2022.
4. The 31st International Toki Conference on Plasma and Fusion Research 2022
5. International Conference MRM2023/IUMRS-2023
6. 17th International Conference on Plasma-Nano Technology & Science 2024 (ISPlasma2024/IC-PLANTS2024/APSPT-13)

Acknowledgements

I am deeply grateful to the many people who have provided invaluable support throughout my studies. Their advice, motivation, insights, and encouragement have been indispensable. Here I endeavor to express my heartfelt thanks to them all.

First, I would like to express my deepest gratitude to my thesis advisor, Prof. Masaharu Shiratani, for granting me the opportunity to pursue this study and for his invaluable guidance and unwavering support throughout my Ph.D. research. His insights and mentorship have been essential to the completion of this work.

Second, I would like to express my sincere gratitude to Dr. Naoto Yamashita for his supervision, encouragement, and guidance throughout my research. His support was crucial at every stage, from conducting experiments and preparing papers to completing this thesis.

I am grateful to Prof. Naho Itagaki for providing access to the laboratory facilities and for the insightful discussions that greatly contributed to my research.

I am grateful to Prof. Hiromi Yuasa and Prof. Hisato Yabuta for their critical readings, useful comments, and suggestions in developing the manuscript.

I also appreciate the support and stimulating discussions with members of Shiratani-Lab, Itagaki-Lab, and Koga-Lab. Their valuable suggestions and collaborative spirit greatly enriched my research experience.

I would like to thank Plasma Lab administrative and technical staffs: Ms. Obata, Ms. Yanagawa, Ms. Kubo, and Ms. Fujimoto. Their support has been invaluable in ensuring the smooth progress of my studies.

Finally, I would like to show my gratitude to Japan International Cooperation Agency (JICA) for the financial support which enabling me to pursue my doctoral degree in Japan.

Thank you all.

Agusutrisno Marlis Nurut.